Origami and kirigami design principles for optical tracking, energy harvesting, and other applications

by

Aaron Louis Lamoureux

A dissertation submitted in partial fulfillment
of the requirements for the degree of
Doctor of Philosophy
(Materials Science and Engineering)
in the University of Michigan
2017

Doctoral Committee:

Professor Max Shtein, Chair
Professor Stephen R. Forrest
Professor Nicholas A. Kotov
Professor Pei-Cheng Ku

ACKNOWLEDGEMENTS

The work presented in this dissertation would not have been possible without the help and unwavering support from family, friends, and colleagues over the past five years.

First, I would like to thank both past and present members of the Shtein Group for helping me to become a better scientist. Kanika Agrawal, Adam Barito, Steve Morris, Olga Shalev, and Matt Sykes – thank you for helping me when I first started, and for continuing to push me on a daily basis to better understand my research. It was clear that you were a close-knit group before I joined, and I really appreciate that you let me be a part of it as well. To the more recent additions – Erin Evke and Lydia Mensah – thank you for putting up with me during my final year, and for all your help in finishing up my research. To the undergrads with whom I have worked – James Berry, Kevin Greenman, Carlos Serrators, and Anthony Wang – thank you for all your help, and for making this work possible. I would also like to thank my collaborators – Chih-Wei Chen, Nicholas Chiotellis, Pablo Damasceno, Paul Dodd, Lawren Gamble, Gogol Guha, Tom Shcrhoeder, Terry Shyu, and especially Byungjun Lee and Kyusang Lee – for your constructive criticisms, passions, and dedication to our projects. This work is equally yours as it is mine.

Second, I would like to thank my friends and family, without whom this dissertation would not be possible. To everyone on the Red Zeppelin intramural team – thank you for letting me be a part of such an amazing group of people, and for single-handedly helping me fill an entire drawer with t-shirts. Despite my several trips to the emergency room (thank you Diana), my time with the team was a needed respite from lab work and something I could not have imagined

doing without. To my close friends in Michigan – Kevin and Ellen – thank you for the time we shared together, and I hope that we will stay in touch going forward. To my cousin Nate – I think we've grown closer over the past five years, and for that I am extremely grateful. I hope we continue to stay close, despite the three-hour time difference. I also want to thank my family - Jaclyn, Mom, and Dad – for your continued unconditional support and love over the past five years. It has been hard being so far from home, but your phone calls, packages, and visits have made everything much easier. To my girlfriend Jess – you are everything to me, and you more than anyone know how hard I have worked for this. You make me a better person, and I am looking forward to the next chapter of our lives together.

Finally, I would like to thank my committee members for pushing me to become a better scientist. To Professor Kotov and Professor Ku – it was great working with your students, and I really appreciate your insight and critiques over the past few years. To Professor Forrest – thank you for allowing me to use your equipment, and for allowing Kyusang and Byungjun to work with me on such interesting projects. My research would not have been possible without all of you, and for that I am extremely grateful. Finally, I would like to thank my advisor, Max Shtein, for allowing me to be part of such an amazing research group. I have learned so much from you about designing experiments, thinking critically, understanding the bigger picture, as well as the best ways to communicate my work to others. I am also thankful for the patience you showed during our disagreements early on, and for the many lessons you have taught me since. You have helped me not only become a better scientist, but a better coworker and person as well.

TABLE OF CONTENTS

LIST OF TABLES

LIST OF FIGURES

ABSTRACT

Origami and kirigami (the folding and cutting of paper, respectively, to achieve a desired shape) have been used in engineering to develop airbags, optical components, deployable spaceborne solar arrays, reprogrammable metamaterials, and load-bearing metal structures. Despite these efforts however, little has been shown beyond the packaging and load-bearing advantages of these three-dimensional approaches to structural design. This dissertation describes the use of dynamic, three-dimensional design principles to develop multifunctional mechanical and optoelectronic devices with improved performance, decreased fabrication costs, and greater economic value. First, we introduce a novel method of integrated, low-profile solar tracking whereby a simple kirigami pattern in thin-film gallium-arsenide solar cells enables tracking at the substrate level simply by stretching the sheet. The new tracker is inherently lightweight and very low profile; it is less susceptible to wind loading, which greatly reduces tracking system complexity, size, and cost, while also enabling new applications. System performance is considered as a function of cut geometry, materials selection, and geographic location, and optimized trackers are shown to generate up to 40% more energy per solar cell area over the course of a day relative to a stationary, flat panel module. Electrical and mechanical robustness are also considered with implications towards long-term solar tracking applications (i.e. >10,000 actuation cycles). Subsequently, we discuss a multifunctional system that combines kirigami solar tracking and integrated concentration optics to further reduce the overall cost of solar

electricity. Optical design, mechanical response, and materials selection are considered to maximize optical and power concentration factor while also maintaining a simple design philosophy. The final system is shown to provide ~60x solar concentration, and further modifications will enable power concentration factors greater than 100x. Finally, similar design principles are extended to develop new applications including textured surfaces for flow manipulation and drag steering, kirigami patterns for tunable antennas, and origami tessellations for novel forms of electrochemical energy storage.

Chapter 1 Introduction

1.1 History of origami and use in engineering

Although the term *origami* (derived from the words *ori – to fold* and *kami – paper*) was only coined in 1880, the idea of folding a two-dimensional sheet into a three-dimensional structure most likely dates back to the invention of paper by Ts'ai Lun of China in 105 A.D. Subsequently, paper folding was practiced in various cultures around the world. For example, in Japan, folded structures were often incorporated into wealthy homes and religious ceremonies. Simultaneously, paper folding was studied in Spain, with an emphasis on mathematics and understanding different geometric shapes. The majority of this work was undocumented, unfortunately, and often only spread by word of mouth. The first written history of simple origami designs can be traced to the *Sebenzuru Orikata*, written in 1797 A.D. A more comprehensive list was published in the *Kayaragusa* in 1845, and extensions to modern designs were subsequently produced by Japanese Master Yoshizawa Akira in the early 1950s[1]. Kirigami, which allows cutting as well as folding of the two-dimensional sheet, has since become popular as well.

Origami was not used as a tool in engineering until the 1970s, when the *Yoshimura* pattern was studied with applicability to large span shell structures, reservoirs, and expansion joints. In particular, *Miura* looked at pseudo-cylindrical concave polyhedral shells, and studied the bending of rigid structures under loading conditions (**Figure 1.1**)[2]. The famous *Miura-ori* pattern resulted from this work, which has been used extensively to develop deployable structures with

rigid facets and to engineer in-plane stiffness[3]. Origami has also been used in the design of shopping bags, deployable spaceborne solar arrays, airbags, optical components, and medical devices[4-8].

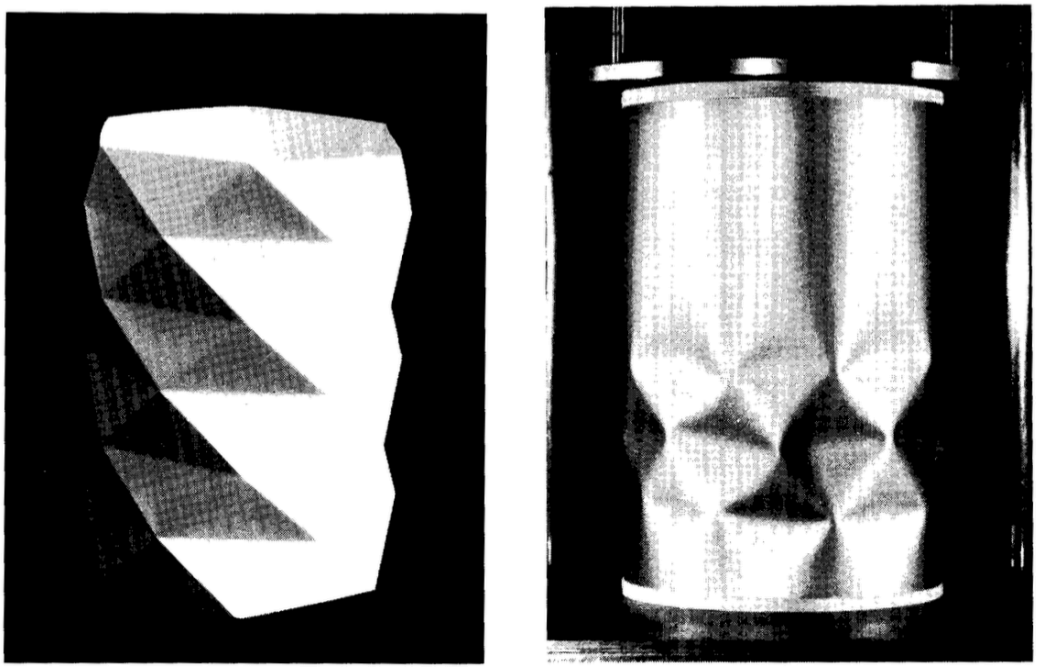

Figure 1.1 The Yoshimura pattern (left) is shown to approximate the bending geometry of cylindrical shells (right).

1.2 Kirigami as an additional design tool

In its purest form, origami allows only for folding of the two-dimensional sheet. From an engineering applications standpoint, this means that new advancements are often incremental, and typically follow the framework of existing origami design principles. *Kirigami*, on the other hand, allows for folding as well as cutting of the two-dimensional sheet. The addition of cutting provides an additional degree of control over geometric design and system behavior. An example of this extra degree of freedom is shown in **Figure 1.2**.

a b

Figure 1.2 (a) An example of a simple origami fold and (b) an equivalent kirigami structure that provides added complexity through the use of strategically placed cuts.

1.3 Origami and kirigami design for highly functionalized and dynamic systems

The majority of origami engineering since the 1970s has focused on deployable and packable structures, where the performance of the unfolded system is identical to that of a system that was simply designed and fabricated to mimic the unfolded state. For example, consider the origami-enabled solar cells developed by Tang *et al*, for which the deformed solar cell performance is equivalent to a planar cell of equivalent area[9], with the added benefit being smaller storage volume. Other similar examples include foldable batteries, foldable kayaks, and load-bearing metal structures[10-12].

More recent research focused on achieving functionality and performance beyond that of the base system. For example, Xu *et al*. have recently proposed kirigami nanocomposities as wide-angle diffraction gratings[13]. In their study, kirigami design is used to enable reconfigurable optical gratings with over a 100% range of period tunability – in other words, kirigami design helps enable a new application. Another example includes work by Shyu *et al*., which leverages

kirigami design to develop dynamic electrodes allowing the density of a plasma discharge inside of an argon-filled glass tube to be tuned by amount of stretch in the kirigami electrode[14].

1.4 Overview of thesis organization

The goal of my research is to use origami and kirigami design principles to develop structures and systems with increased functionality and highly dynamic geometric response. Specifically, I focus on optoelectronic applications related to solar tracking, optical concentration, and combined solar tracking and optical concentration using arrays of miniaturized concentrators moved in unison. The aim is to enable rooftop solar concentration and tracking, and thereby decrease the cost of solar photovoltaic electricity to levels competitive with conventional sources of electricity. The rest of this dissertation is organized as follows. Additional theory and introductions will be given at the beginning of each chapter, with the goal being to provide the reader with sufficient information to completely understand the problems, research goals, and outcomes. Additional applications derived from the main advances described are presented in later chapters, setting a foundation for further research and improvement in the field of highly functionalized kirigami design and engineering.

Chapter 2 Dynamic Kirigami Structures for Integrated Solar Tracking

2.1 Introduction

2.1.1 The current energy landscape

As of 2013, the world total primary energy supply (TPES) was approximately 14,000 million tonnes of oil equivalent (Mtoe), or roughly 150,000 terawatt hours (tWh)[15]. In the United States (U.S.) alone, the TPES was ~2,216 Mtoe in 2014, of which nearly 80% was supplied by unsustainable fossil fuel sources. In fact, less than 2% of the entire TPES in the U.S. is supplied by renewable sources such as wind, geothermal, and solar power[16].

Due to yearly increases in carbon dioxide (CO_2) emissions and concerns over global warming, humankind is currently on a search to increase the use of renewable energy sources and decrease our dependence on fossil fuels. Solar power appears to be an excellent candidate to replace fossil fuels, namely due to the fact that the sun provides ~1.2×10^5 TW per year to the surface of the Earth. At this rate, only 10,000 km^2 of 20%-efficient modules would be required to offset the entire U.S. annual energy consumption per year (~4000 TWh). Perhaps even more astonishing, up to 40% of total, current energy needs could be met in the U.S. using existing rooftop space alone[17]. Unfortunately, as of 2016, total solar installations in the U.S. accounted for only 24.9 TWh (~0.6%) of total energy generation[18].

To understand why the use of solar is limited, it is helpful to consider the cost of solar versus other energy sources. To this point, consider the levelized cost of energy (LCOE), an economic assessment of the average total cost to build and operate a given power-generating asset of its lifetime, divided by the total energy output of that asset over its lifetime. Typically, LCOE is reported as an amortized quantity, over a predetermined lifetime of new and existing systems. Accordingly, consider **Figure 2.1**, which depicts the anticipated LCEO by 2020 for various energy sources. As shown, solar electricity is not only more costly than other forms of renewable energies (e.g. biomass, wind, geothermal), it is >30% more costly than coal and >50% more costly than natural gas[19]. The takeaway: the cost per energy for solar needs to decrease significantly to enable widespread adoption.

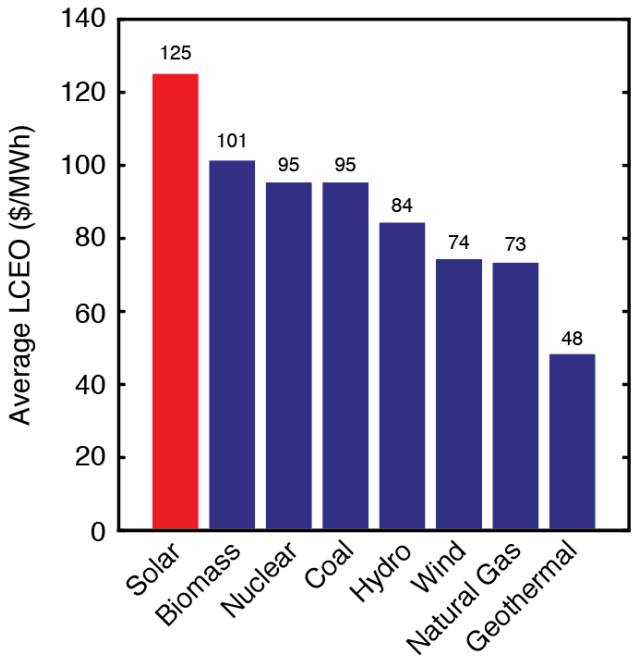

Figure 2.1 Anticipated LCOE for the U.S. by 2020, whereby solar PV source is still considered to be the most expensive, compared to conventional and even other renewable sources of energy.

2.1.2 Photovoltaic cell research and cost structures

The total cost of solar electricity is comprised of *hard costs* – associated with physical photovoltaic (PV) module components, and *soft costs* – associated with tariffs, permitting, customer acquisition, financing, installation, and other *soft* economic considerations (**Figure 2.2a**)[20]. The power conversion efficiency (*PCE*) and the amount of semiconductor material used in a solar cell have the most direct impact on the *hard* costs of every watt-hour of electricity generated by the photovoltaic module. The main research and development objectives have, therefore, focused on both increasing the power conversion efficiency and reducing the cost of photovoltaic modules.

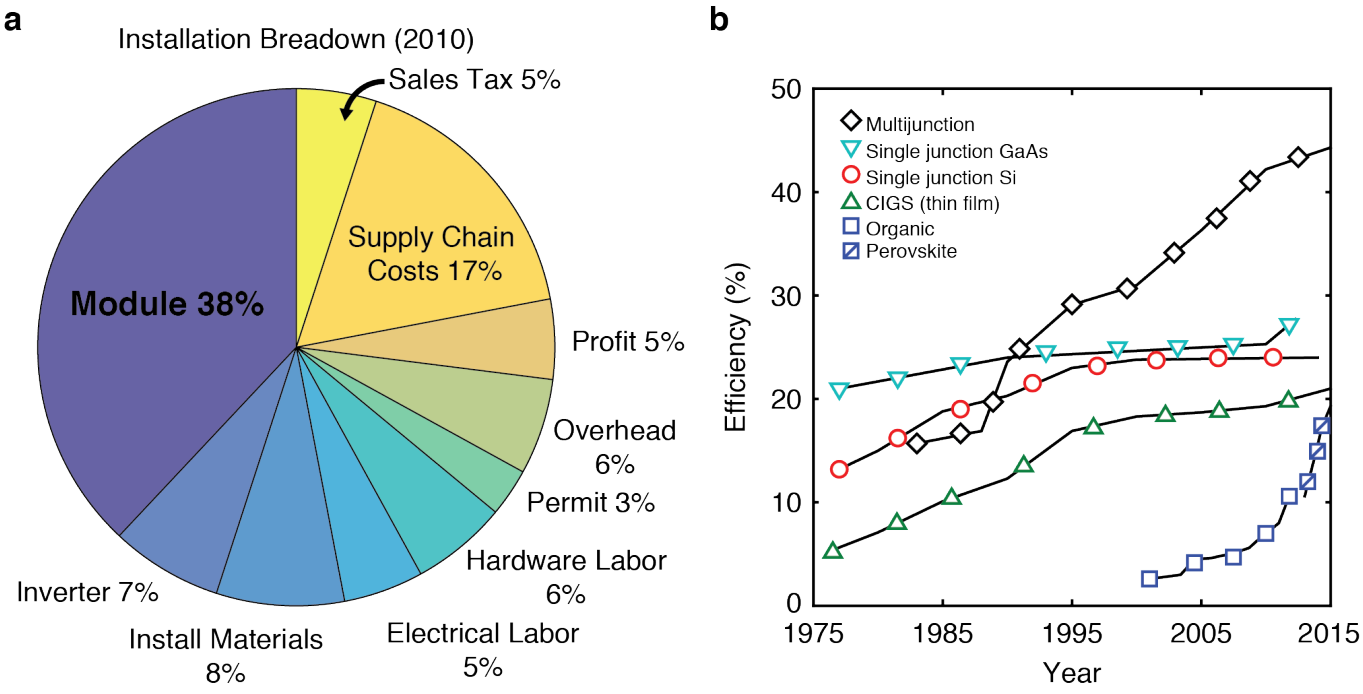

Figure 2.2 (a) Breakdown of installation costs for conventional residential system in 2010. (b) Research over the past 50+ years has led to drastic improvements in efficiency and conformability, although current single-junction systems are limited by thermodynamic limits. Multijunction systems, which break this tradeoff, are expensive, and not currently appropriate for widespread application.

At the heart of the PV module is a PV cell, comprising a semiconductor *p-n* junction. Considerable research has focused on improving the power conversion efficiency of the p-n junction, for both crystalline and thin-film semiconductors, including single junction direct (e.g. GaAs) and indirect bangap (e.g. Si) configurations, multijunction designs, thin-film (inorganic and organic) systems, and more recently perovskite-based PV cells (see **Figure 2.2b**)[21].

While conventional PV material systems have improved steadily, these gains have been incremental over the past 10-15 years (particularly for single junction systems, which are thermodynamically limited to ~33%)[22]. Meanwhile, the improvements in efficiency often also entail increased cost, such that the combined effects partially cancel each other. This tendency of high efficiency PV cells to cost more is depicted in **Figure 2.3a**[23], plotting "iso-energy" lines for different generations of technology.

Consider now the total balance of system (BOS) costs associated with conventional PV modules, and in particular, the cost of the semiconductor with respect to total module costs (**Figure 2.3b**). As shown, for Si PV modules which (as of 2015) account for ~93% of installed systems, the cost due to semiconductor (although decreasing) is still relatively high (~60%). For high-efficiency systems, such as conventional thin-film GaAs (PCE is ~29%), the cost due to semiconductor is extremely high (>80%)[20,24-25]. Work is currently underway to decrease fabrication costs for high-efficiency systems (e.g. GaAs) using low-cost, reusable wafer technologies, while fabrication costs for medium-efficiency Si systems have been largely minimized already thanks to decades of research in the computer chip industry[26-28].

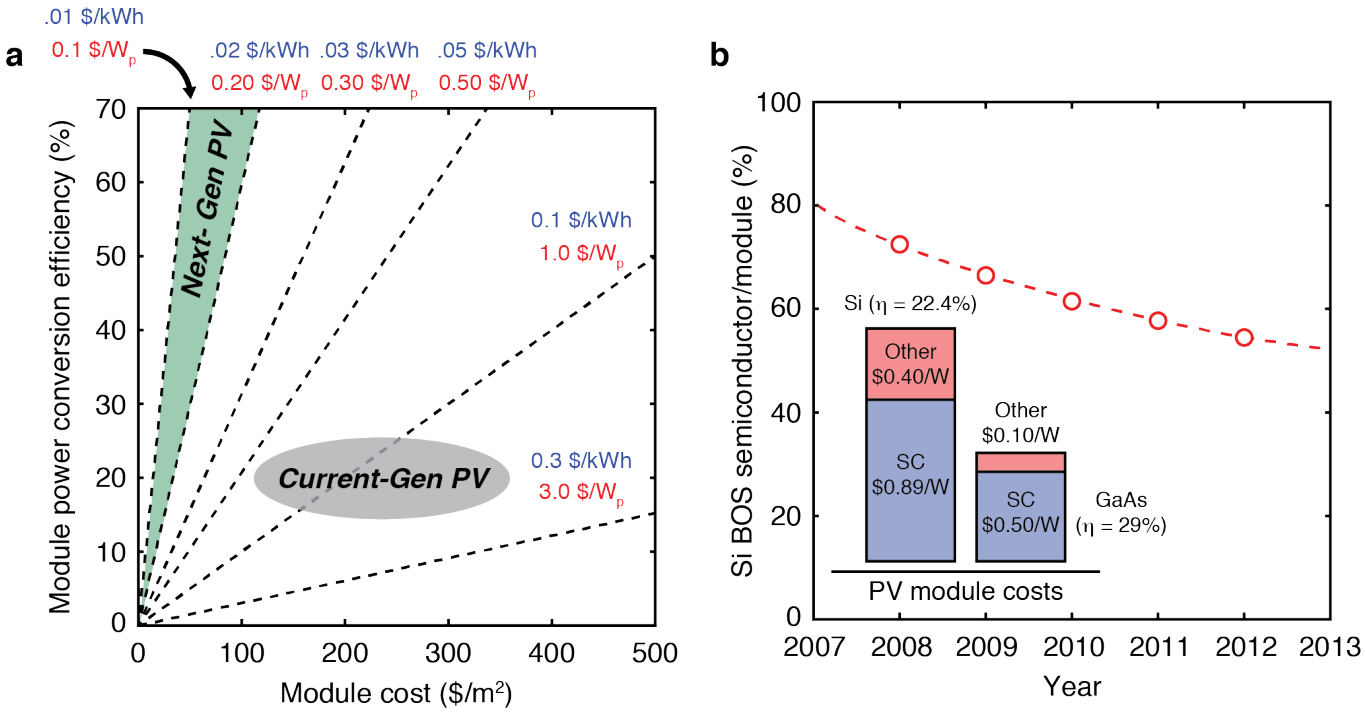

Figure 2.3 (a) To decrease the cost of electricity, next-gen PV must either drastically increase *PCE* or decrease module costs. (b) Cost per energy can be decreased by either increasing PCE or decrease module costs. *Inset*: Semiconductor costs account for ~60% of total BOS costs in Si PV, and >80% in high-efficiency GaAs PV modules.

Diurnal solar tracking increases energy production over the course of a day by as much as 40% relative to stationary panels. However, typical solar tracking mechanisms are bulky and expensive, and have been limited in their market penetration. The fundamentals and trade-offs of conventional solar tracking are discussed in the following section, setting the stage for a discussion of our kirigami-based solar tracking design.

2.1.3 Solar intensity, air mass, and standardized measurement

Although solar radiation incident on the Earth's atmosphere is relatively constant (~1353 W/m^2), radiation incident on the surface of the Earth varies as a function of 1) atmospheric effects such as absorption and scattering, 2) local variations in the atmosphere due to water vapor, cloud coverage, and pollution, 3) geographic location, and 4) time of year and time of day. To this point, it is often helpful to consider the air mass (*AM*), which is a measure of the path length which light takes through the atmosphere normalized to the shortest possible path length (inset of **Figure 2.4a**). Per the spherical model:

$$AM = \frac{s}{y_{atm}} = \sqrt{(r\cos\theta)^2 + 2r + 1} - r\cos\theta \tag{1}$$

and:

$$r = \frac{R_E}{y_{atm}} \tag{2}$$

where R_E is the effective radius of the Earth (~6371 km), y_{atm} is the thickness of the atmosphere (~9 km), and θ is the incident angle of the sun.

Using *AM*, direct intensity (I_D) can then be calculated as follows:

$$I_D = 1.353 \cdot 0.7^{\left(AM^{0.678}\right)} \tag{3}$$

where 1.353 kW/m^2 is the solar constant, 0.7 represents the amount of transmitted radiation to the surface of the Earth, and 0.678 is an empirical constant. Accounting for diffuse (i.e. scattered, indirect) radiation, which amounts to 10% of the direct component, the total global irradiance, I_G, is:

$$I_G = 1.1 \cdot I_D \tag{4}$$

Figure 2.4a shows air mass as a function of incident angle and **Figure 2.4b** depicts direct and global irradiance as a function of incident angle.

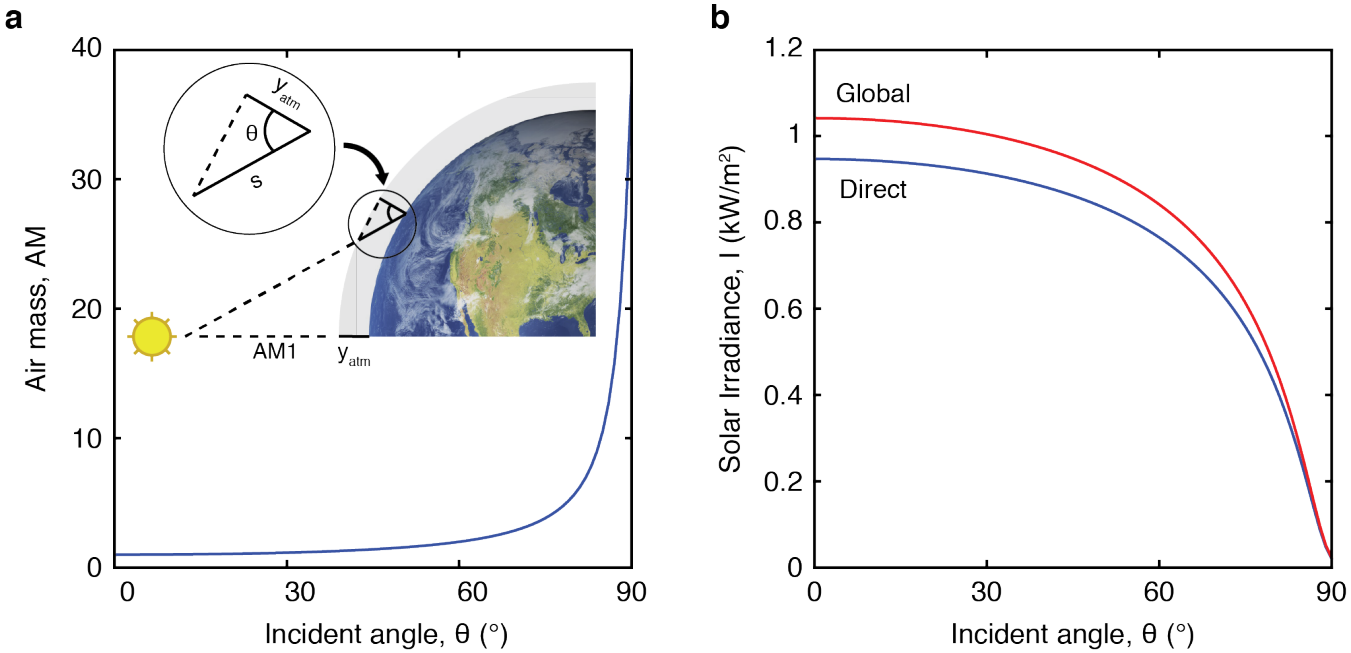

Figure 2.4 (a) Air mass (AM) as a function of incident angle. (b) Direct solar intensity (I_D) as a function of incident angle. *Inset*: Air mass (AM) is a measure of the path length that light from the sun must take through the atmosphere as a function of incident angle, normalized to the shortest path length (equal to the thickness of the atmosphere).

To facilitate an accurate comparison between solar cells that would otherwise be tested under different incident conditions, a standardized spectrum and air mass are often used. At the surface of the Earth, the standard spectrum is AM1.5G (where the *G* stands for *global*, and includes direct and diffuse radiation). For AM1.5G, θ is taken as ~48°, and global irradiance is 970 W/m^2 but often rounded to 1000 W/m^2 for convenience. **Figure 2.5** shows the difference between AM0 (outside of the Earth's atmosphere) and AM1.5G, whereby the change in spectrum and decrease in intensity are due to air mass and the other atmospheric effects explained above.

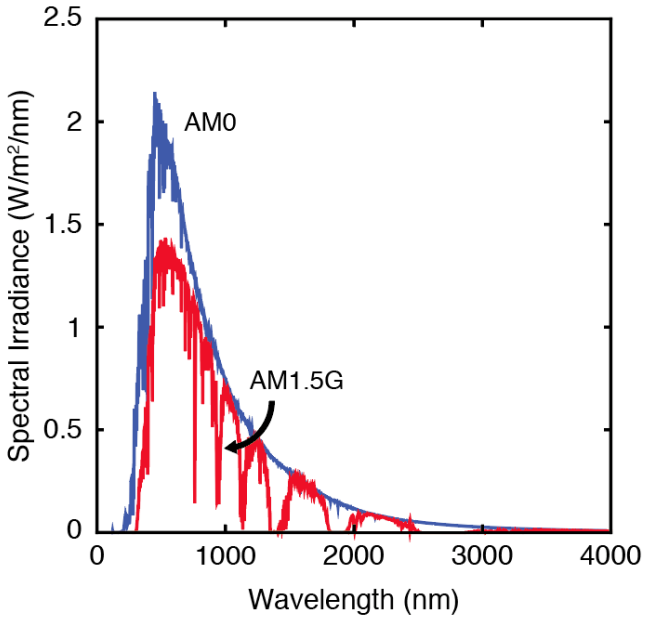

Figure 2.5 Spectral irradiance for AM0 and AM1.5G standards. Noticed the change in spectrum and decrease in intensity, resulting from atmospheric absorption and an increased path length.

2.1.4 Coupling efficiency and solar tracking

An addition to atmospheric losses associated with air mass as discussed in **Section 2.1.3**, conventional PV modules also suffer optical coupling losses due to a decrease in the projected area that scales with the cosine of the misalignment angle between the cell and the sun (**Figure 2.6a**). Since power output is directly related to effective area and coupling efficiency (η_C), power output can be expressed as:

$$P_{gen} = P_{inc}\eta_C = P_{inc}\cos\theta \tag{5}$$

where P_{inc} and P_{gen} are the incident and generated power, respectively, and θ is the misalignment angle between the cell and the sun.

To reduce cosine losses and increase power (and thus energy) density, flat PV modules are often titled to track the sun over the course of the day and/or year. Depending on the geographic location of the system, and whether there are one or two tracking axes, conventional trackers can

provide an increase in yearly energy generation between 20 and 40% compared with non-tracking solar arrays[29,30]. **Figure 2.6b** shows the effect of solar tracking on effective area and coupling efficiency, and **Figure 2.7** shows the effect of solar tracking on power and energy density (for Phoenix, AZ during the summer solstice). See **Section 2.3** and **2.4** for more information on coupling efficiency and energy calculations.

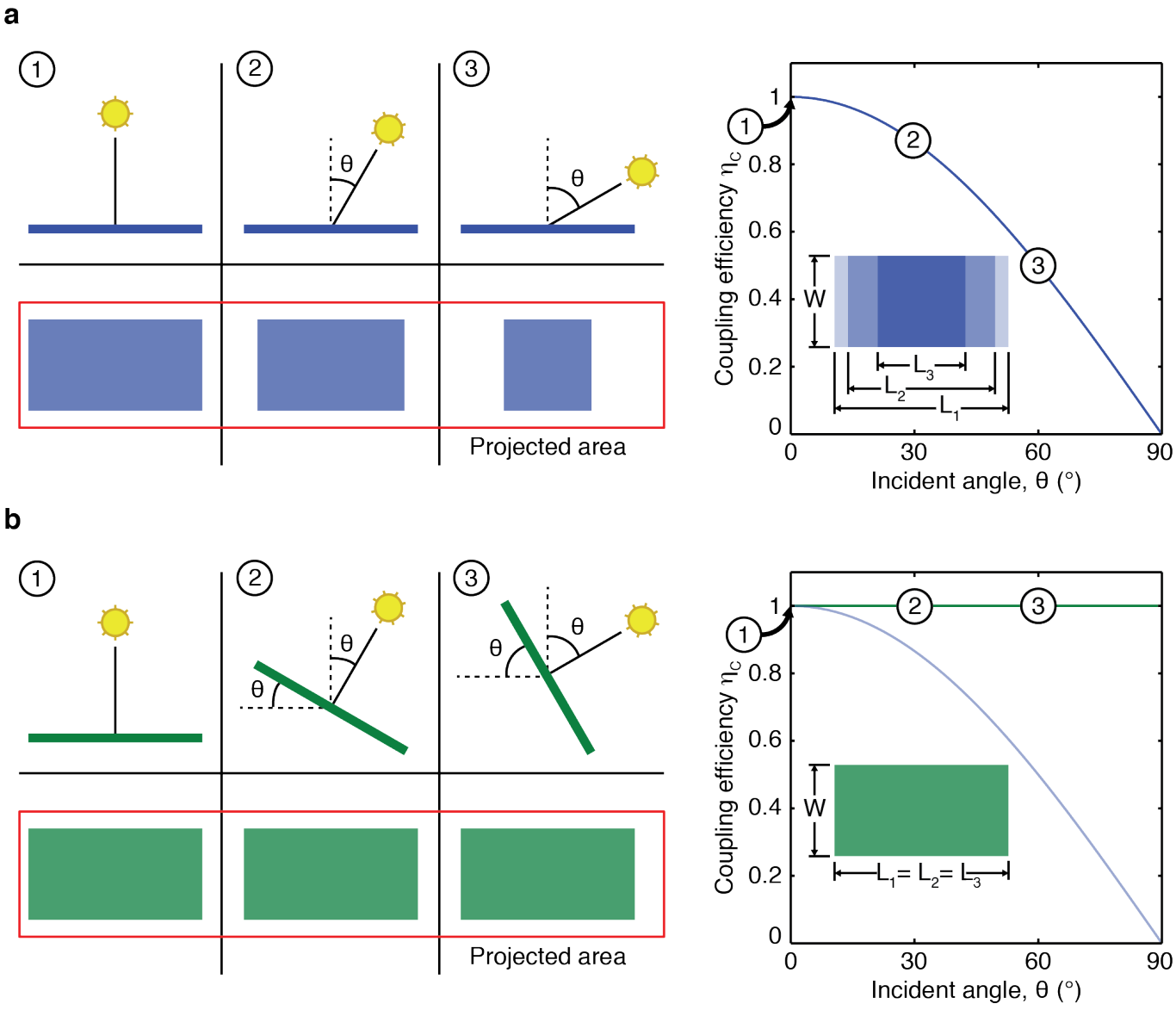

Figure 2.6 (a) For a conventional flat panel, projected area and coupling efficiency decrease as a function of incident angle. (b) By titling the PV module to track the sun, the goal is to maximize effective area and increase coupling efficiency.

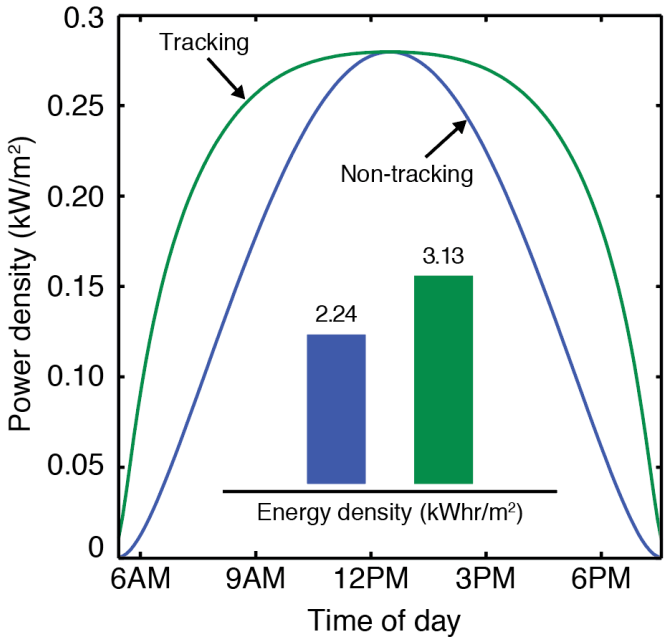

Figure 2.7 (a) Power and energy density comparison for 30% efficiency non-tracking and tracking PV modules in Phoenix, AZ during the summer solstice. In the scenario shown, solar tracking provides a 40% increase in energy density over the course of the day.

2.1.5 Conventional PV, market size, and installation economics

While the previous section makes it obvious that solar tracking is advantageous with respect to maximizing energy collected for a given area of semiconductor used, the practical realization of solar tracking using conventional means introduces complications and costs that limit its market penetration. To understand the current market for conventional PV systems, it is useful to split the contributions from residential/commercial systems (with installed capacities < 1 MW) and utility-scale systems (with installed capacities > 1 MW). As shown in **Figure 2.8**, residential/commercial and utility-scale systems are being installed at a relatively equal rate (as of 2012), however residential/commercial systems account for nearly 2/3 of the total installed capacity[24]. If we consider the number of installations, rather than capacity, however, the difference is much greater. For example, as of 2012, nearly 99.9% of installed systems were considered residential/commercial (with capacities < 1 MW) (**Figure 2.9a**), and of that 99.9%,

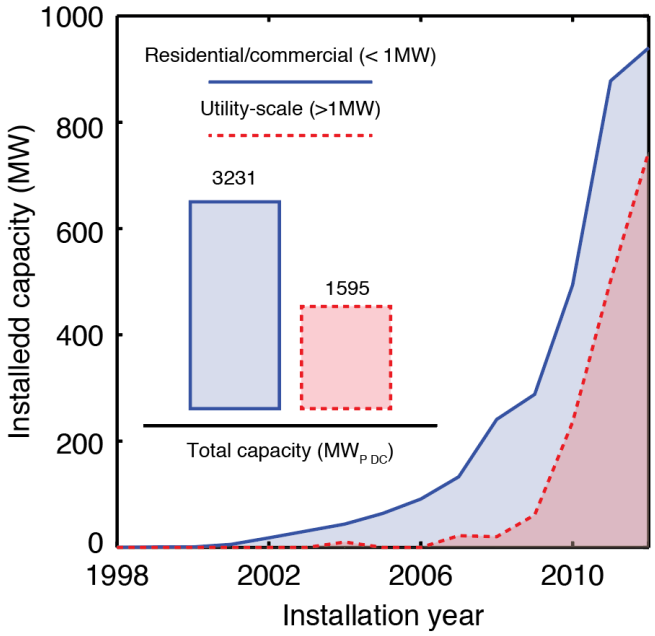

Figure 2.8 As of 2012, residential/commercial (capacities <1 MW) and utility-scale (capacities >1 MW) systems are being added at a similar rate. However, residential/commercial systems account for nearly 2/3 of total installed capacity.

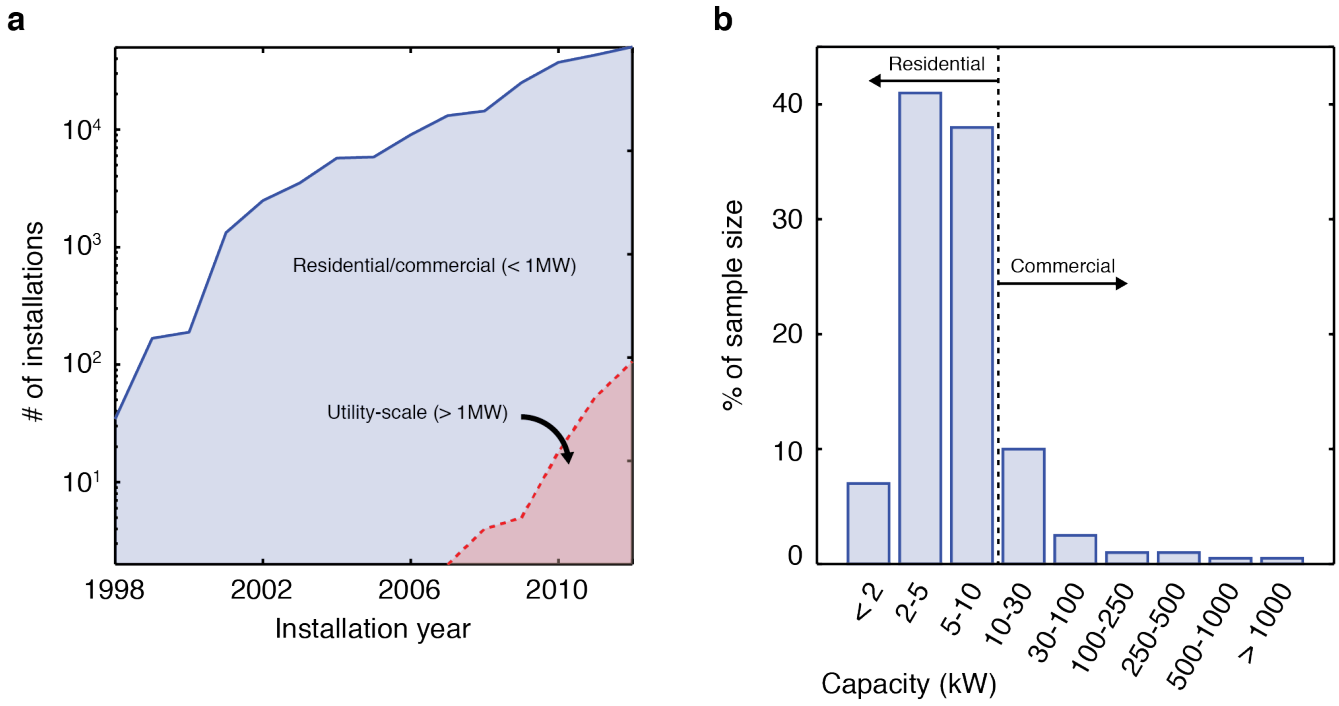

Figure 2.9 (a) Nearly 99.9% of installed systems are residential/commercial, and of those 99.9%, (b) nearly 85% (by capacity) are residential.

nearly 85% were residential systems (with capacities <10 kW) (**Figure 2.9b**). Of these residential systems, less than 0.1% utilize solar tracking[24]. Solar trackers are not commonplace, mainly due to the added costs of tracking and structural components required to track the sun, support system weight, resist wind loading, and enable installations on the ground (**Figure 2.10a**). The fraction of total module cost is also increasing year over year, namely due to the increase in prices of commodity goods (e.g. steel, concrete, etc.) with respect to decreasing semiconductor prices. In fact, ground-based solar trackers cost ~40% more than rooftop, fixed-axis systems that do not require tracking or additional structural components. The increase in cost due to tracking and structural components is often offset by an increase in energy generation due to tracking, however even at a 30% increase in energy generation, a ground-based, single-axis tracker is still >7% more costly than a rooftop-based, fixed-axis PV module (**Figure 2.10b**).

Rooftop, fixed-axis systems cost ~13% less than their ground-based equivalents, because they eliminate the need for foundation and land preparation by utilize existing rooftop infrastructure[24]. If this cost-saving approach is applied to solar trackers (i.e. to reduce structural costs), these hypothetical rooftop trackers would help offset the cost of tracking components and reduce the overall cost of the system. For example, a rooftop tracker with a 30% increase in energy generation would cost ~10% less per watt-hour than conventional ground-mounted solar trackers and ~4% less per watt-hour than equivalent, rooftop flat panel modules. To this point, **Figure 2.10b** provides more detail on costs savings as a function of solar tracking performance.

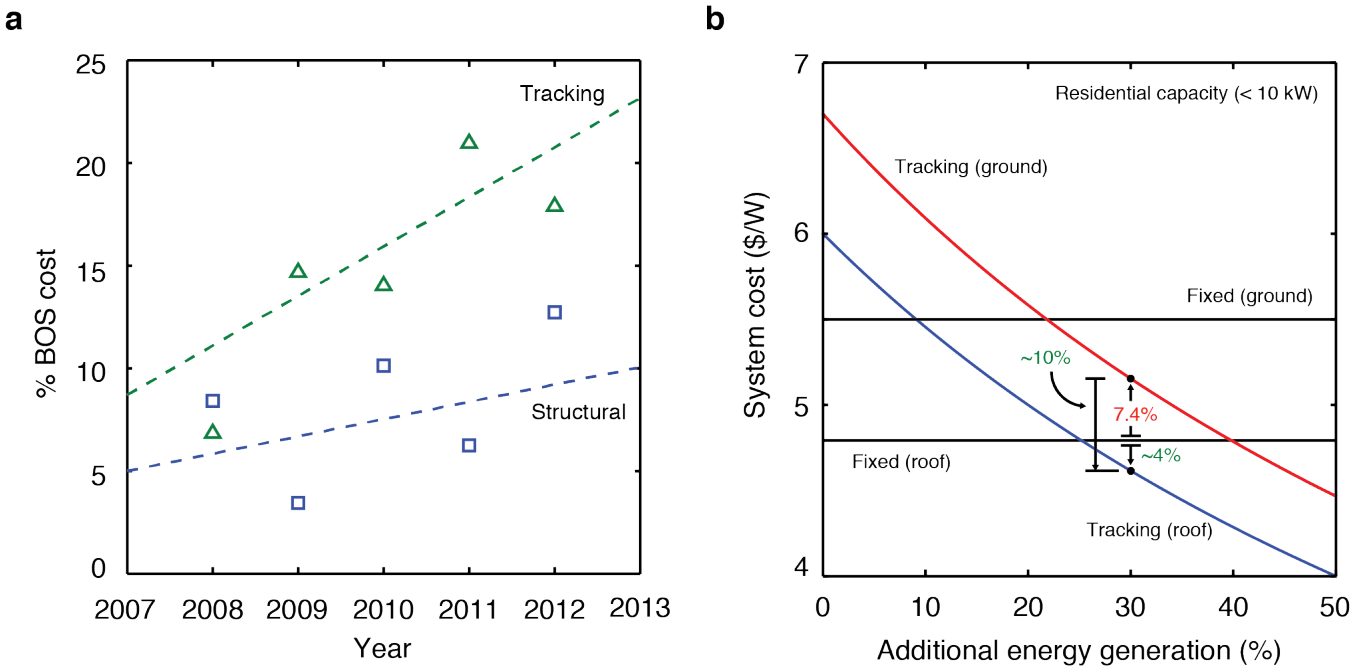

Figure 2.10 (a) Tracking and structural components required to track the sun, support system weight, resist wind loading, and facilitate installations on the ground account for a large portion of total BOS costs. (b) A hypothetical rooftop tracker (with a 30% increase in energy generation) would cost ~10% less per watt than conventional solar trackers and ~4% less per watt than equivalent, rooftop flat panel modules.

2.1.6 The issue of wind loading and conventional trackers

As shown in the previous section, rooftop-mounted solar trackers have the potential to drastically reduce installed costs. Unfortunately, due to the weight and bulk of conventional systems, rooftop mounting is extremely rare and impractical. Consider for example wind loading as a function of geographic location, altitude, and panel area in the direction parallel to flow, where:

$$F = \int P \, dA \tag{6}$$

where F is the force due to wind loading, P is the pressure, and dA is equivalent to the panel cross-sectional area in the direction parallel to flow. Pressure is a function of density (ρ) and velocity (v) according to:

$$P = \rho v^2 \tag{7}$$

where

$$\rho = \frac{M}{RT}\left(1 - \frac{La}{T}\right)^{\frac{gM}{RL}} \tag{8}$$

and

$$v = \left(\frac{u*}{0.4}\right)\log\left(\frac{a}{z_0}\right) \tag{9}$$

In equations (8,9), P_0 is the standard pressure at sea level (~101 kPa), L is the temperature lapse rate (0.065 K/m), a is the altitude of the PV installation, g is acceleration due to gravity (9.8 m/s^2), M is the molar mass of dry air (~0.029 kg/mol), R is the ideal gas constant (8.314 J/mol/K), and $u*$ and z_0 are experimental constants used to account for varying terrain. Temperature is also a function of altitude, such that:

$$T = T_0 - La \tag{10}$$

where T_0 is the temperature at sea level (288 K).

Figure 2.11a shows wind loading as a function of altitude and module footprint in the direction of flow. Category 3 terrain was chosen (numerous closely spaced obstructions 3 to 5 meters apart, replicating a suburban housing development), such that $u*$ and z_0 are 1.626 and 0.2, respectively. Also shown are the relative number of non-tracking and tracking installations – due to the large form factor of conventional trackers and the resulting high wind loads, conventional solar trackers are not suited for rooftop installations. This is an extremely important issue, and something that the majority of this chapter will look to address. The ultimate goal is to use origami and kirigami design principles to develop a low-profile solar tracker that is lightweight and not subject to wind loading (**Figure 11b**). Such a system would decrease costs due to system weight, and also enable new applications previously reserved for non-tracking systems.

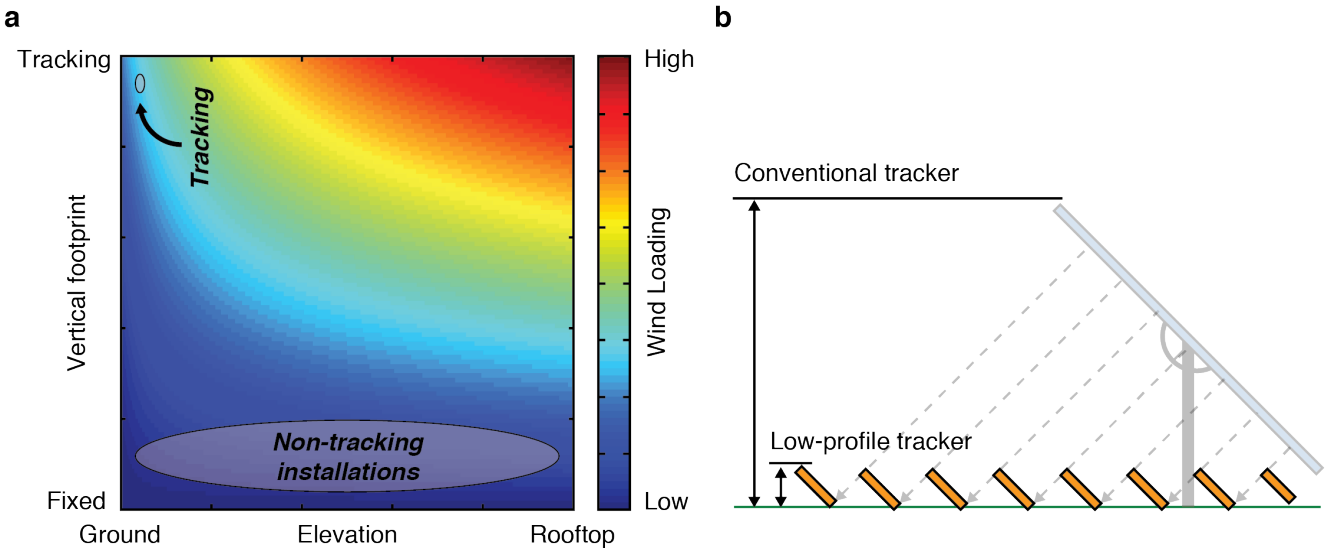

Figure 2.11 (a) Due to the large vertical footprint and high wind loading on conventional trackers, existing systems are currently limited to ground-based installation. (b) By decreasing vertical footprint, the goal is to decrease system costs and enable new applications for solar tracking.

2.2 Kirigami design principles

2.2.1 Design parameters and geometric response

Consider the simple kirigami structure shown in the inset of **Figure 2.12a**. The structure consists of a repeating linear cut pattern in an otherwise thin, continuous sheet of flexible material. Pulling on this structure in a direction perpendicular to the cuts (here designated as the *axial direction*) results in instabilities that produce controlled buckling in the transverse direction (i.e. parallel to the cuts) and a change in feature angle of the material between the cuts. This transformation is shown pictorially in **Figure 2.12a,** and schematically in **Figure 2.12b**. Also shown in **Fig. 2.12b** is how semiconductor could be mounted onto the surface of a mechanical carrier substrate, and the subsequent geometric response of the structure used to track the movement of the sun. Importantly, it is possible to control the direction of feature tilt (i.e.

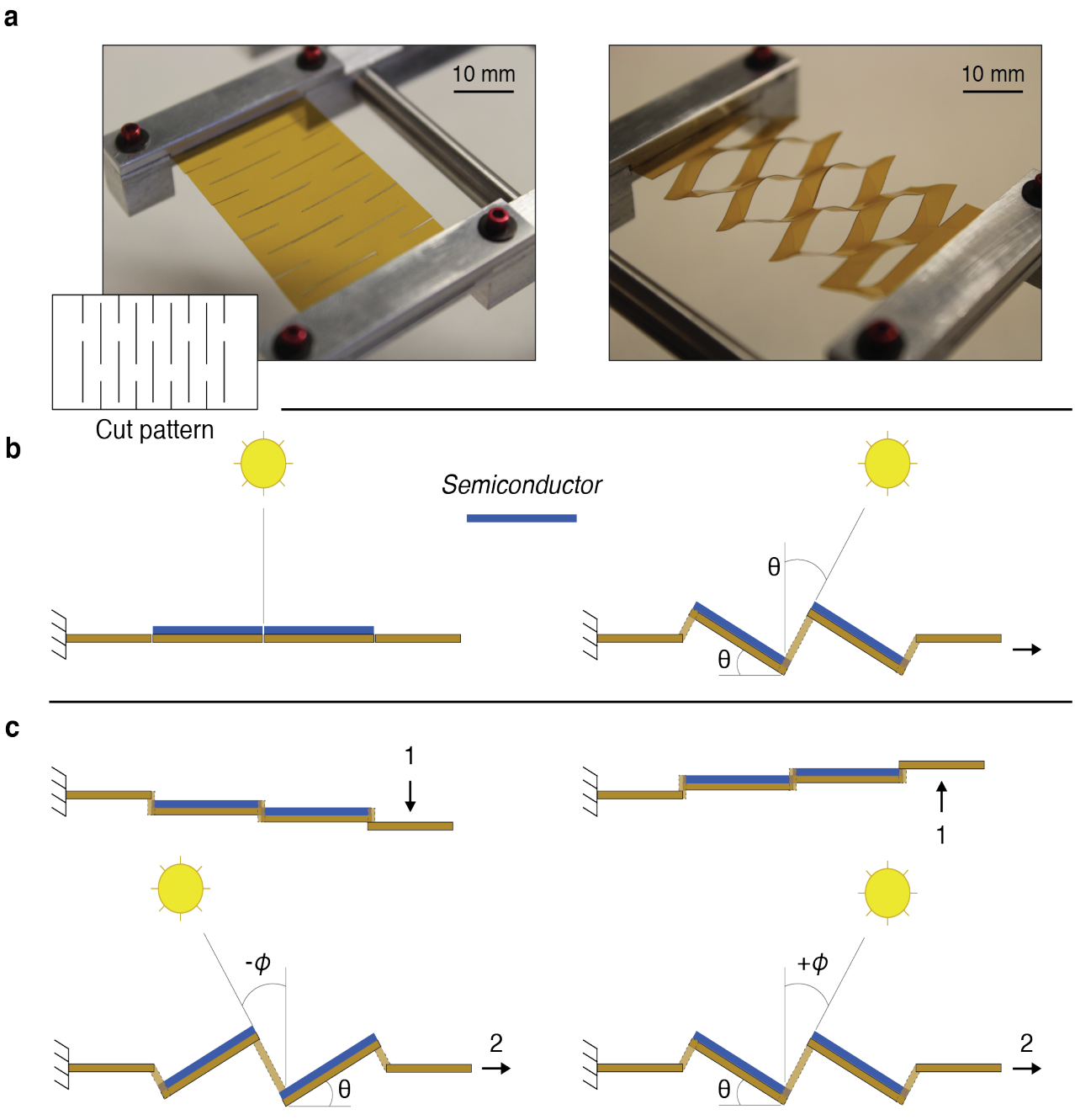

Figure 2.12 (a) Pulling on the linear cut pattern (shown in *inset*) in the axial direction results in instabilities and a change in feature angle of the material between the cuts. (b) Schematic of geometric response. By mounting flexible semiconductor to the surface of a carrier substrate, the linear cut pattern may be used as a macroscopically low-profile way to track the sun. (c) The direction of feature tilt (i.e. clockwise or counter-clockwise with respect to the original place) is controlled by lifting or lowering one end of the sheet (step 1) before pulling (step 2).

positive or negative θ) by lifting or lowering one end of the sheet before the straining process (**Figure 2.12c**). This structure is macroscopically flat when compared to conventional trackers, and could potentially eliminate a lot of the wind loading and system weight that typically lead to high tracking costs.

The geometric response of the linear kirigami structure is clarified in **Figure 2.13a**, where the kirigami geometry is defined by the cut length (L_C), as well as the spacing between cuts in the transverse (x) and axial (y) directions. Using simple geometry, it is possible to relate the change in feature angle (θ) and decrease in sample width (i.e. transverse strain, ε_T) due to buckling along the length as a function of cut parameters and axial strain (ε_A).

$$\theta = \cos^{-1}\left(\frac{1}{\varepsilon_A + 1}\right) \tag{11}$$

$$\varepsilon_T = \frac{R_1 - 1}{R_1 + 1}\left[\cos\left(\sin^{-1}\left(\frac{2R_1 \tan\theta}{R_1 R_2 - R_2}\right)\right) - 1\right] \tag{12}$$

where $R_1 = \frac{L_C}{x}$ and $R_2 = \frac{L_C}{y}$ are dimensionless parameters, and $\varepsilon_A = \frac{L - L_0}{L_0}$ and $\varepsilon_T = \frac{W - W_0}{W_0}$ define the axial and transverse strains, respectively. Please see **Section 2.2.1.1** for derivations for equations (11,12).

To examine the effect of cut parameters on geometric response, R_1 and R_2 were systematically varied such that $R_1 = R_2 = 3$, 5, 10, and 20, as shown in schematic form in **Figure 2.13b**. Specific cut parameters are as follows: $R_1 = R_2 = 3$ ($L_C = 6$ mm, $x = 2$ mm, and $y = 2$ mm), $R_1 = R_2 = 5$ ($L_C = 10$ mm, $x = 2$ mm, and $y = 2$ mm), $R_1 = R_2 = 10$ ($L_C = 20$ mm, $x = 2$ mm, and $y = 2$ mm), $R_1 = R_2 = 20$ ($L_C = 20$ mm, $x = 1$ mm, and $y = 1$ mm). The response characterized by equations (11,12) (solid lines) is experimentally verified (closed symbols) for all geometries in **Figure 2.13c**. We find that larger R_1 and R_2 enable increased axial strains and correspondingly larger tracking

angles, where the maximum pseudo-plastic limit for each superstructure is proportional to the maximum tracking angle (θ_{MAX}):

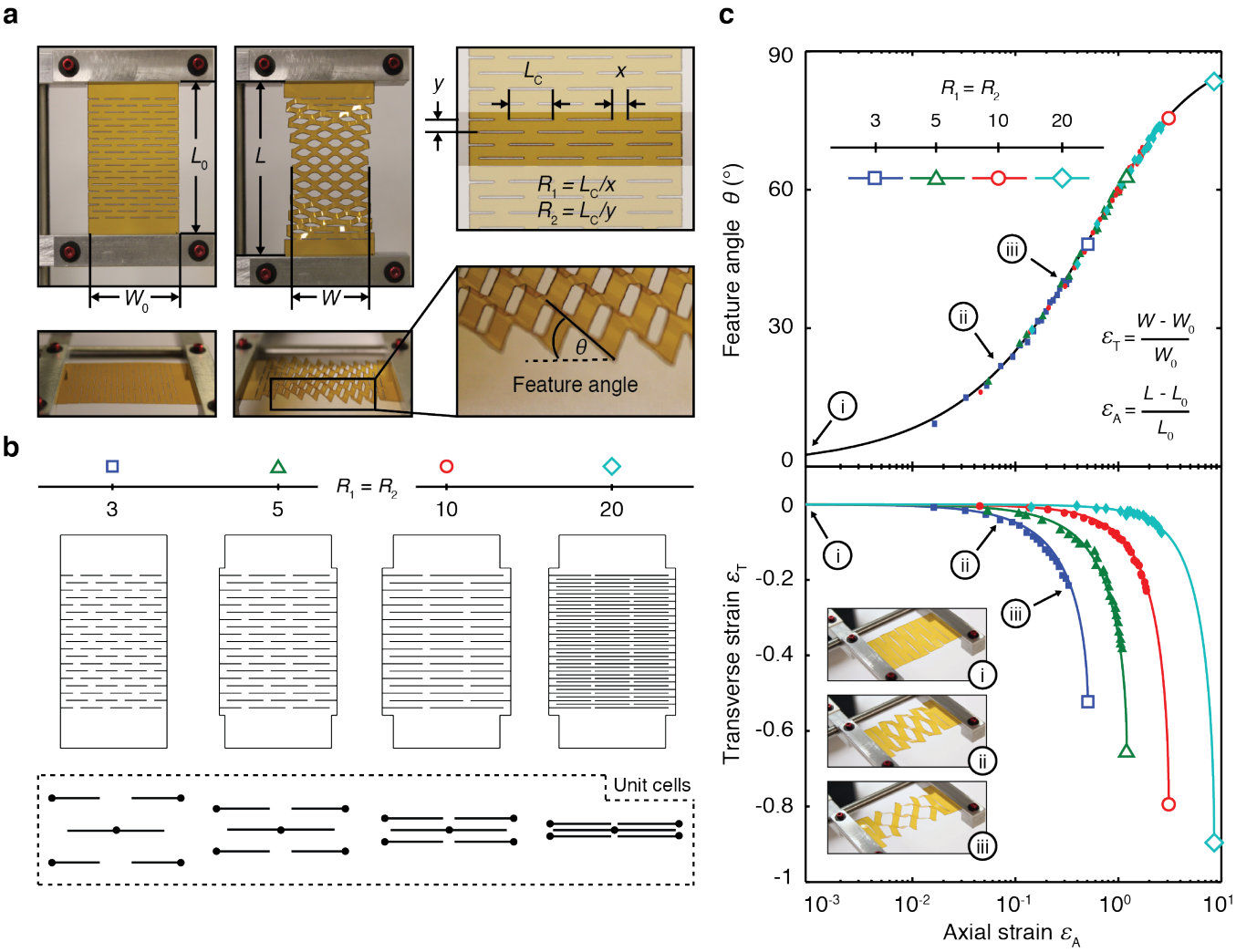

Figure 2.13 (a) Response of a Kapton® kirigami structure to stretching in the axial direction (ε_A) is accompanied by a decrease in sample width (ε_T) and a change in feature angle (θ). Also shown are the geometric parameters that define the kirigami structure, namely the cut length (L_C) and spacing between cuts in the transverse (x) and axial (y) directions, which can be expressed in terms of the dimensionless parameters, R_1 and R_2. (b) Schematics of four kirigami structures, where $R_1 = R_2 = 3$, 5, 10, and 20, along with their corresponding units cells. (c) Transverse strain (ε_T), and feature angle (θ), *vs.* axial strain (ε_A), for several kirigami structures where $R_1 = R_2 = 3$, 5, 10, and 20. Theoretical predictions per equations (11,12) are shown by solid lines, while the closed symbols represent experimental data from a 50 μm-thick Kapton® sample of the appropriate geometry. While larger R_1 and R_2 enable increased axial strains and correspondingly larger transverse strains, the change in feature angle is independent of cut geometry.

$$\theta_{MAX} = \tan^{-1}\left(\frac{R_1 R_2 - R_2}{2R_1}\right) \tag{13}$$

A plot of θ *vs.* ε_A confirms that the change in feature angle in response to axial strain is independent of cut geometry. For the samples tested, θ was controlled to within ±1.0° of its value in equation (11). Another (perhaps more intuitive) way to view the effect of cut geometry on ε_T is shown in **Figure 2.14**. As you can see, geometric necking is reduced as R_1 and R_2 are increased. This effect is extremely important, as it will directly affect coupling efficiency and solar tracking performance (see **Section 2.3** and **Section 2.4**).

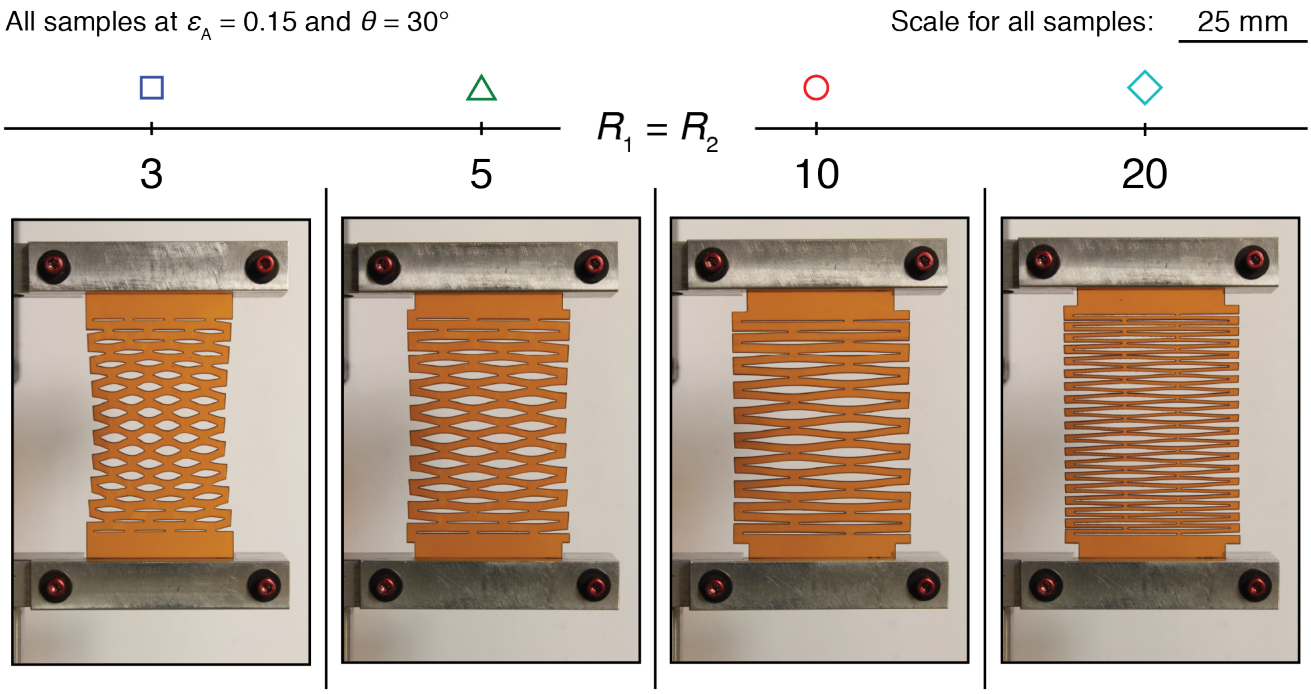

Figure 2.14 Four kirigami samples with different R_1 and R_2 values at the sample axial strain (0.15) and angle (30°). As shown, the magnitude of geometric necking ($|\varepsilon_T|$) is reduced as R_1 and R_2 are increased.

Based on equations (11,12), it is also possible to calculate the "geometric" Poisson ratio (v) of the linear kirigami structures:

$$\nu = -\frac{\varepsilon_T}{\varepsilon_A} \tag{14}$$

where ε_T is the transverse strain predicted by equation (12) and ε_A is the axial strain. ν is plotted versus ε_A in **Figure 2.15a** for kirigami structures were $R_1 = R_2 = 3$, 5, 10, and 20. Notice that, although ν for each structure is constant over most of the operation range, it increases significantly at strains near the geometric maximums of the structure. In addition, we see that ν is smaller for higher R_1 and R_2. This is expected, considering the geometric response previously shown in **Figure 2.12c**. Furthermore, **Figure 2.15b** plots ν at low ε_A (i.e. in the region where ν is constant) versus R_1 and R_2. Again, as expected, ν is smaller for larger values of R_1 and R_2.

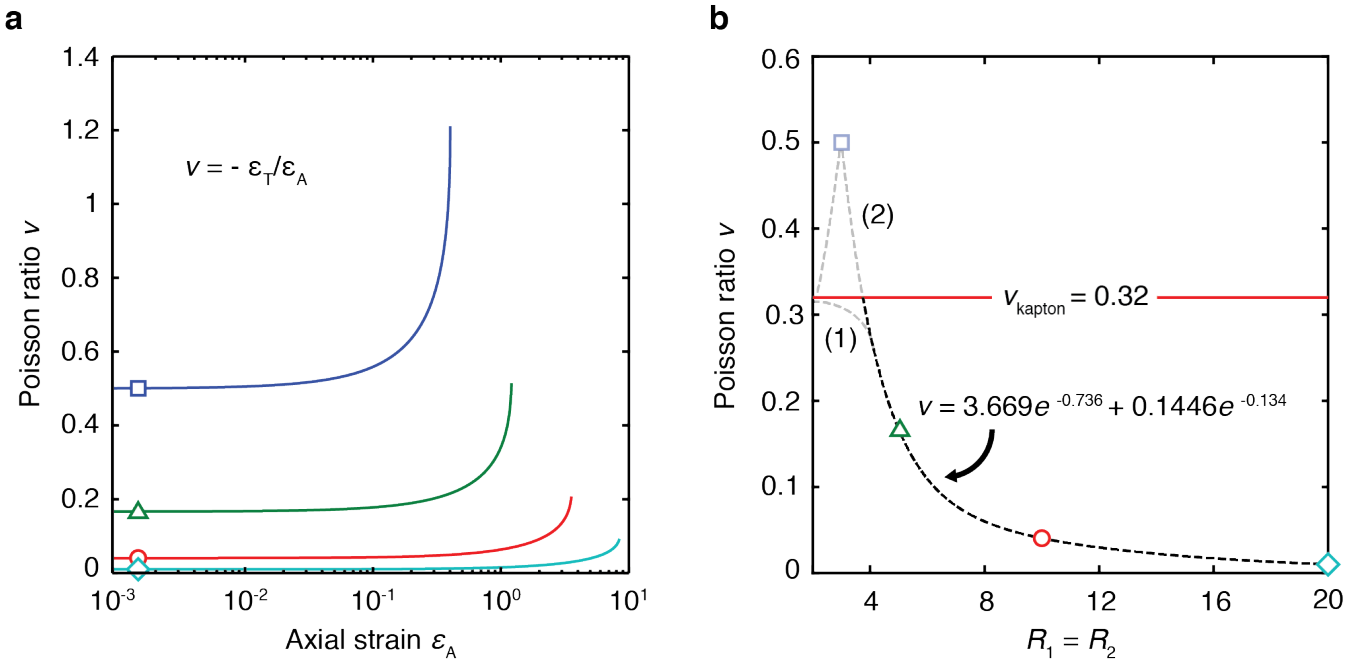

Figure 2.15 (a) Geometric Poisson ratio (ν) versus axial strain (ε_A) for several kirigami structures, where $R_1 = R_2 = 3$, 5, 10, and 20. (b) Poisson ratio (ν) at low strains versus R_1 and R_2. Also shown are two hypothetical curves to explain the increase in ν at low R_1 and R_2.

Although the trend in **Figure 2.15b** is expected, an anomaly occurs at low values of R_1 and R_2. The Poisson ratio of the kirigami pattern becomes larger than the Poisson ratio of a pristine, uncut sheet of the same material (in this case, Kapton® is used). This is unexpected, as one

would assume that as the cuts become smaller and smaller, the Poisson ratio should approach that of the base material. To explain this response, we consider two mechanisms:

Mechanism 1: Defect engineering has been used in the past to modify Poisson ratio. Moreover, small voids have been shown to increase the Poisson ratio of the material[31]. One hypothesis is that the kirigami cuts are behaving like small voids at small values of R_1 and R_2, resulting in an increase in Poisson ratio. Once the cuts are long enough, the kirigami response predicted by equation (11,12) takes over and the Poisson ratio decreases accordingly. A hypothetical response curve is marked as (1) in **Figure 2.15b**.

Mechanism 2: For small values of R_1 and R_2, the bending elements are relatively short (L_C) in comparison to their width (y). Instead of these elements deforming normal to the plane of the solar cells, it may be that there are some additional deformation parameters (e.g. rotation and/or torsional effects) that need to be considered. These effects would result in the Poisson ratio deviating from purely geometric origins and approaching the Poisson ratio of the base material at low values of R_1 and R_2. A hypothetical response curve is marked as (2) in **Figure 2.15b**.

2.2.1.1 Derivation of geometric response

To fully understand the origins of equations (11-13) it is helpful to provide a detailed look at geometric response and go systematically through their derivations. **Figure 2.16a** shows geometric response as viewed from the side, whereby stretching the geometry results in a change in θ as a function of ε_A.

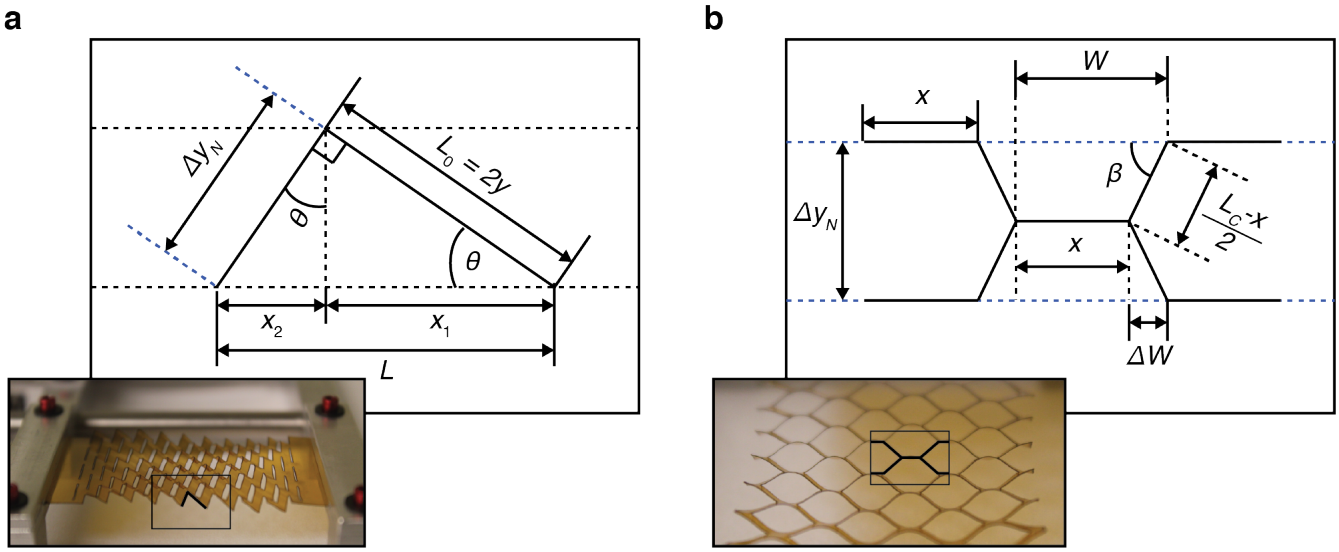

Figure 2.16 (a) Detailed geometric response and calculation parameters used to calculate ε_A as a function of θ, per equation (11). (b) Detailed geometric response and calculation parameters used to calculate ε_T as a function of ε_A and cut parameters, per equation (12).

If we consider a single unit cell, the initial length (L_0) when $\theta = 0°$ is equal to $2y$. Subsequently, the instantaneous length of the structure (L_0) is:

$$L = x_1 + x_2 \tag{15}$$

where

$$x_1 = 2y\cos\theta \tag{16}$$

and

$$x_2 = 2y\sin\theta\tan\theta \tag{17}$$

ε_A is defined as $\frac{L-L_0}{L_0}$, which means that we can calculate ε_A in terms of equations (14-16):

$$\varepsilon_A = \frac{L-L_0}{L_0} = \frac{2y\cos\theta + 2y\sin\theta\tan\theta - 2y}{2y} = \cos\theta + \sin\theta\tan\theta - 1 = \sec\theta - 1 \tag{18}$$

where secθ is equal to $\frac{1}{\cos\theta}$. Using this relationship, we can rearrange equation (17) to:

$$\varepsilon_A = \frac{1}{\cos\theta} - 1 \tag{11}$$

Figure 2.16b depicts the geometric origins of ε_T, and also includes the relevant calculation parameters needed to derive equation (12). Specifically, we can calculate ε_T by considering that:

$$\varepsilon_T = \frac{W - W_0}{W_0} \tag{19}$$

where

$$W_0 = x + \frac{L_C - x}{2} \tag{20}$$

and the instantaneous width (W) is a function of x and the change width (ΔW):

$$W = x + \Delta W \tag{21}$$

where

$$\Delta W = \left(\frac{L_C - x}{2}\right)\cos\beta \tag{22}$$

and

$$\beta = \cos^{-1}\left[\frac{\Delta y_N}{2\left(\frac{L_C - x}{2}\right)}\right] = \cos^{-1}\left(\frac{\Delta y_N}{L_C - x}\right) \tag{23}$$

From **Figure 2.16a** we know that:

$$\Delta y_N = 2y\tan\theta \tag{24}$$

such that

$$\beta = \cos^{-1}\left[\frac{2y\tan\theta}{(L_C - x)}\right] = \sin^{-1}\left(\frac{2y\tan\theta}{L_C - x}\right) \tag{25}$$

Putting everything together and solving for ε_T:

$$\begin{aligned}\varepsilon_T &= \frac{x + \left(\frac{L_C - x}{2}\right)\cos\left[\sin^{-1}\left(\frac{2y\tan\theta}{L_C - x}\right)\right] - \left(x + \frac{L_C - x}{2}\right)}{x + \frac{L_C - x}{2}} \\ &= \frac{\left(\frac{L_C - x}{2}\right)\cos\left[\sin^{-1}\left(\frac{2y\tan\theta}{L_C - x}\right)\right] - \left(\frac{L_C - x}{2}\right)}{x + \frac{L_C - x}{2}}\end{aligned} \tag{26}$$

To further simplify equation (23), it is helpful to convert all geometric parameters to R_1 and R_2.

$$\frac{L_C - x}{2} = \frac{x(R_1 - 1)}{2} \tag{27}$$

and

$$\frac{2y\tan\theta}{L_C - x} = \frac{2R_1\tan\theta}{R_1R_2 - R_2} \tag{28}$$

Combining equation (26) with equation equations (27-28), we are able to arrive at equation (12).

$$\begin{aligned}\varepsilon_T &= \frac{\frac{x(R_1 - 1)}{2}\cos\left[\sin^{-1}\left(\frac{2y\tan\theta}{L_C - x}\right)\right] - \frac{x(R_1 - 1)}{2}}{x + \frac{x(R_1 - 1)}{2}} \\ &= \frac{(R_1 - 1)\cos\left[\sin^{-1}\left(\frac{2y\tan\theta}{L_C - x}\right)\right] - (R_1 - 1)}{2 + (R_1 - 1)} \\ &= \frac{R_1 - 1}{R_1 + 1}\left[\cos\left(\sin^{-1}\left(\frac{2R_1\tan\theta}{R_1R_2 - R_2}\right)\right) - 1\right]\end{aligned} \tag{12}$$

2.3 Optical coupling efficiency

2.3.1 Optical coupling efficiency for kirigami trackers

To determine the total coupling efficiency (η_C) for the kirigami tracker, we must consider the coupling efficiency due to the motion of the sun and tracking angle of the kirigami tracker (η_1) as well as the coupling efficiency due cosine and geometric effects due to the dynamic response of the kirigami structure (η_2). Each case is shown in **Figure 2.17a** and **Figure 2.17b**, respectively.

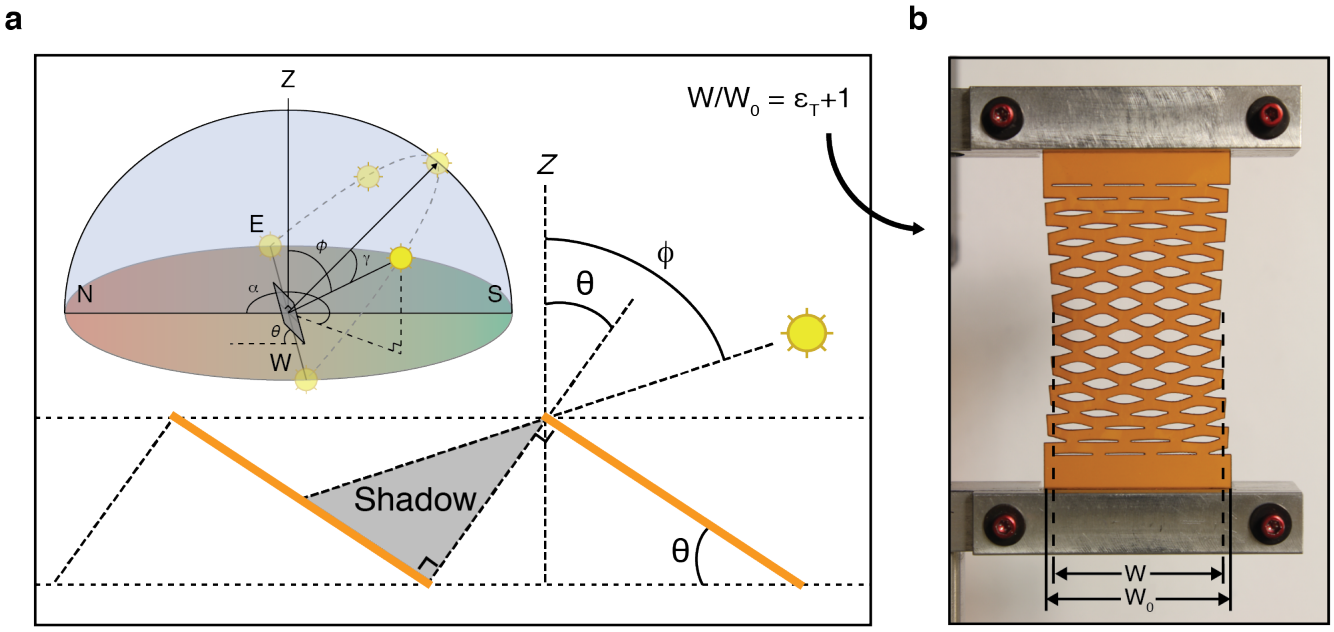

Figure 2.17 Optical coupling efficiency can be broken down into (a) axial losses due to the motion of the sun and tracking angle (i.e. η_1) and (b) reflection and geometric losses due to the dynamic response of the kirigami tracker (i.e. η_2).

Total coupling efficiency (η_C) can be calculated as the product of η_1 and η_2 such that:

$$\eta_C = \eta_1 \cdot \eta_2 \tag{29}$$

where

$$\eta_1 = \left[1 - \tan\theta \tan(\phi - \theta)\right] \cos\gamma \tag{30}$$

and

$$\eta_2 = (\varepsilon_T + 1)(1 - R) \tag{31}$$

such that

$$\eta_C = (\varepsilon_T + 1)(1 - R)\left[1 - \tan\theta \tan(\phi - \theta)\right]\cos\gamma \tag{32}$$

where θ is the kirigami tracking angle, ϕ is the angle of the sun from zenith, γ is the misalignment angle between the normal to the solar cell and the sun, and ε_T and R are the transverse strain and reflection losses for the kirigami tracker, respectively. Here, γ can be calculated as a function of zenith angle (ϕ) and azimuthal angle (α):

$$\gamma = \cos^{-1}\left(\frac{a \cdot b}{|a||b|}\right) \tag{33}$$

where, for a panel with an E-W axis of rotation as was used in this study:

$$a = \begin{bmatrix} -\sin\phi\cos\alpha & \sin\phi\sin\alpha & \cos\phi \end{bmatrix} \tag{34}$$

$$b = \begin{bmatrix} 0 & -\tan\theta & -1 \end{bmatrix} \tag{35}$$

2.3.1.1 Derivation of coupling efficiency

To fully understand the origins of coupling efficiency and how they relate to the kirigami tracker, it is helpful to go through the derivation. Accordingly, **Figure 2.18** provides a schematic view of geometric response as used to derive coupling efficiency:

$$x_1 = 2y\sin\theta \tag{36}$$

$$x_2 = \frac{x_1}{\cos\theta} = 2y\tan\theta \tag{37}$$

$$x_3 = x_2\tan(\phi - \theta) = 2y\tan\theta\tan(\phi - \theta) \tag{38}$$

$$x_4 = 2y(1 - x_3) = 2y\left[1 - \tan\theta\tan(\phi - \theta)\right] \tag{39}$$

$$\eta_1 = \frac{x_4}{2y}\cos\gamma = \left[1 - \tan\theta\tan\left(\phi - \theta\right)\right]\cos\gamma \tag{30}$$

$$\eta_2 = \frac{W}{W_0}\left(1 - R\right) = \left(\varepsilon_T + 1\right)\left(1 - R\right) \tag{31}$$

$$\eta_C = \eta_1 \cdot \eta_2 = \left(\varepsilon_T + 1\right)\left(1 - R\right)\left[1 - \tan\theta\tan\left(\phi - \theta\right)\right]\cos\gamma \tag{32}$$

Note that γ is not shown in **Figure 2.18**. Instead, please see the inset of **Figure 2.17a** for reference.

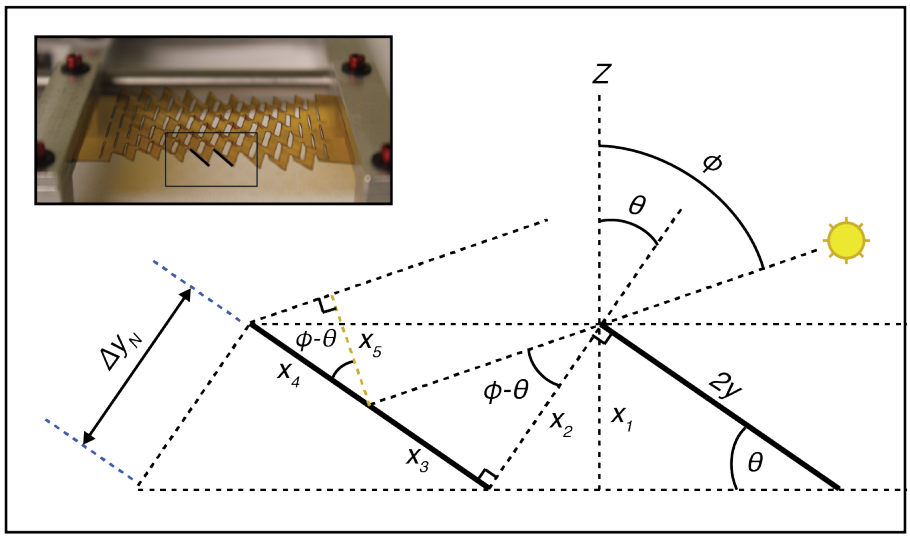

Figure 2.18 Detailed geometric response and calculation parameters used to calculate total coupling efficiency (η_T).

2.3.2 Optimization

To maximize solar tracking performance, we must maximize η_C. Accordingly, shadowing in the axial direction, as well as cosine losses, must be balanced against the decrease in width resulting from the geometric response of the structure. Indeed, tracking to θ_{MAX} may not be optimal due to the sharp decrease in projected area beyond some critical strain (see **Figure 2.13c**). This geometric subtly is shown in **Figure 2.19a**, where we analyze the differences in coupling

efficiency for optimized tracking (open symbols), and one variation of non-optimized tracking to θ_{MAX} (closed symbols) for $R_1 = R_2 = 5$.

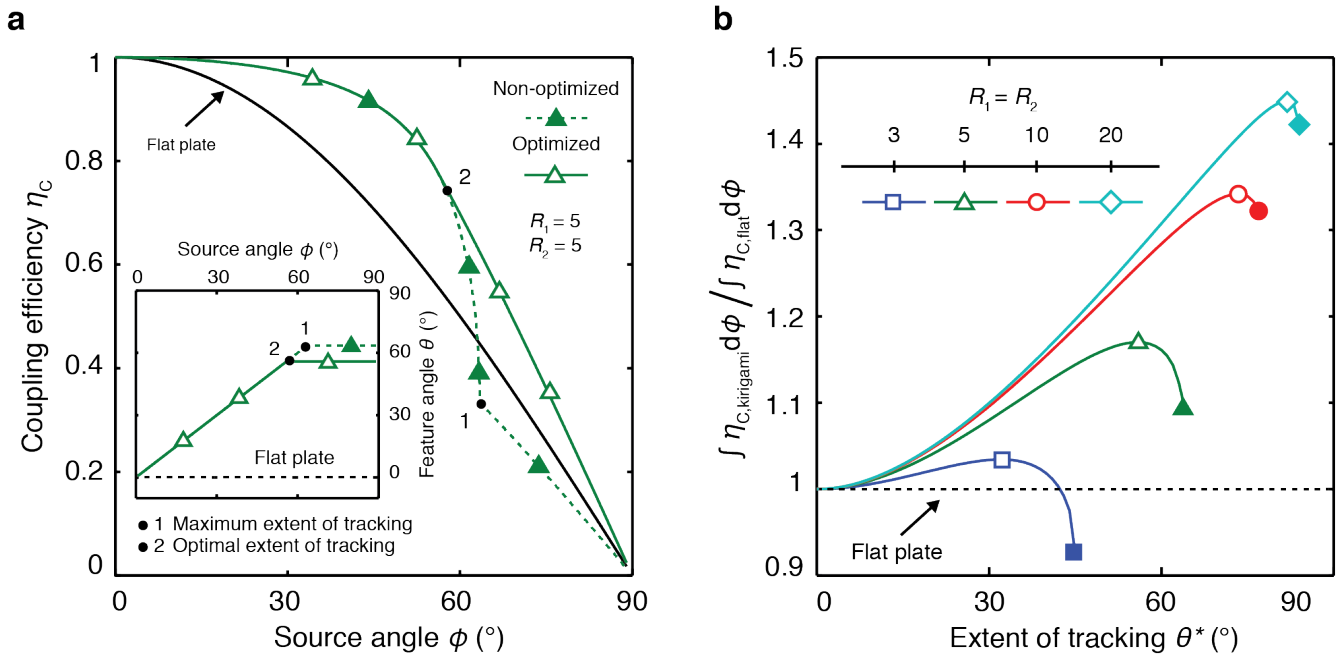

Figure 2.19 (a) Coupling efficiency (η_C) versus source angle (ϕ) for optimized (solid lines) and non-optimized (dashed lines) tracking. *Inset*: Feature angle (θ) versus ϕ. (b) η_C integrated over a range of tracking angles (from ϕ = 0 to ϕ = θ^*) and normalized to conventional planar cell performance. Open and closed symbols represent optimized and non-optimized tracking, respectively.

As shown in the inset of **Figure 2.19a** (θ *vs.* ϕ), each kirigami tracker trackers the source as characterized by a unity slope until a predetermined (and arbitrary) value of θ^* is reached (i.e. extent of tracking), after which the tracking angle (θ) is held constant. Here, θ^* is denoted as *point 1* and *point 2* for non-optimized and optimized tracking, respectively. The effects of these tracking modes are shown in the plot of η_C *vs.* ϕ – note the difference in η_C at large values of ϕ. Whereas tracking to θ_{MAX} (closed symbols) causes a large decrease in sample width and η_C near the geometric limits of the structure, optimized tracking (open symbols) minimizes the tradeoff between geometric losses, self-shadowing, and cosine losses to maximize η_C. **Figure 2.19b**

shows the extension of this analysis to other cut geometries, where η_C is integrated over a range of tracking angles (from $\phi = 0$ to $\phi = \theta^*$) and normalized to conventional planar cell performance. This provides the optimal tracking process for a given kirigami structure, where maximum performance is obtained by tracking the source at normal incidence until reaching the θ^* corresponding to the maximum of each curve (for $R_1 = R_2 = 3$, $\theta^* \approx 37°$, for $R_1 = R_2 = 5$, $\theta^* \approx 54°$, for $R_1 = R_2 = 10$, $\theta^* \approx 73°$, and for $R_1 = R_2 = 20$, $\theta^* \approx 82°$). For comparison, tracking to θ_{MAX} *vs.* the optimized tracking limit are shown as solid and open symbols, respectively.

2.3.3 Experimental validation

To verify η_C per equation (32), kirigami solar trackers were fabricated from gallium arsenide (GaAs) semiconductor *p-n* junctions transferred onto a polyimide film using an epitaxial lift-off process (ELO)[26-28,32]. An example of a kirigami tracker with $R_1 = R_2 = 3$ ($L_C = 15$ mm, $x = 5$ mm, $y = 5$ mm) is shown in **Figure 2.20a**, and more detailed information on fabrication can be found in **Section 2.7**. A kirigami tracker with $R_1 = R_2 = 5$ ($L_C = 15$ mm, $x = 3$ mm, $y = 3$ mm) was also tested. Larger values were not tested due to limitations in the GaAs fabrication process and experimental considerations. Each tracker was systematically strained to follow a moving AM1.5G collimated light source, and the solar cell current density vs. voltage (*J-V*) characteristics were obtained as a function of illumination angle (ϕ). A schematic of this experiment is shown in the inset of **Figure 2.20b**, where the kirigami tracker was strained to track the light source to the optimal θ^* per the process shown in **Figure 2.19**.

Figure 2.20b plots the ratio of the normalized angle-dependent short circuit current density ($J_{SC}(\phi)/J_{SC}(\phi=0)$) for two samples, where $R_1 = R_2 = 3$ and $R_1 = R_2 = 5$ (closed symbols). Also shown is η_C defined by equation (32) for several cut geometries (open symbols, solid lines). As

expected, larger R_1 and R_2 lead to an increase in η_C due to the suppression of ε_T at equivalent ε_A. Furthermore, $J_{SC}(\phi)/J_{SC}(\phi=0)$ matches η_C predicted by equation (32), suggesting that η_C is a

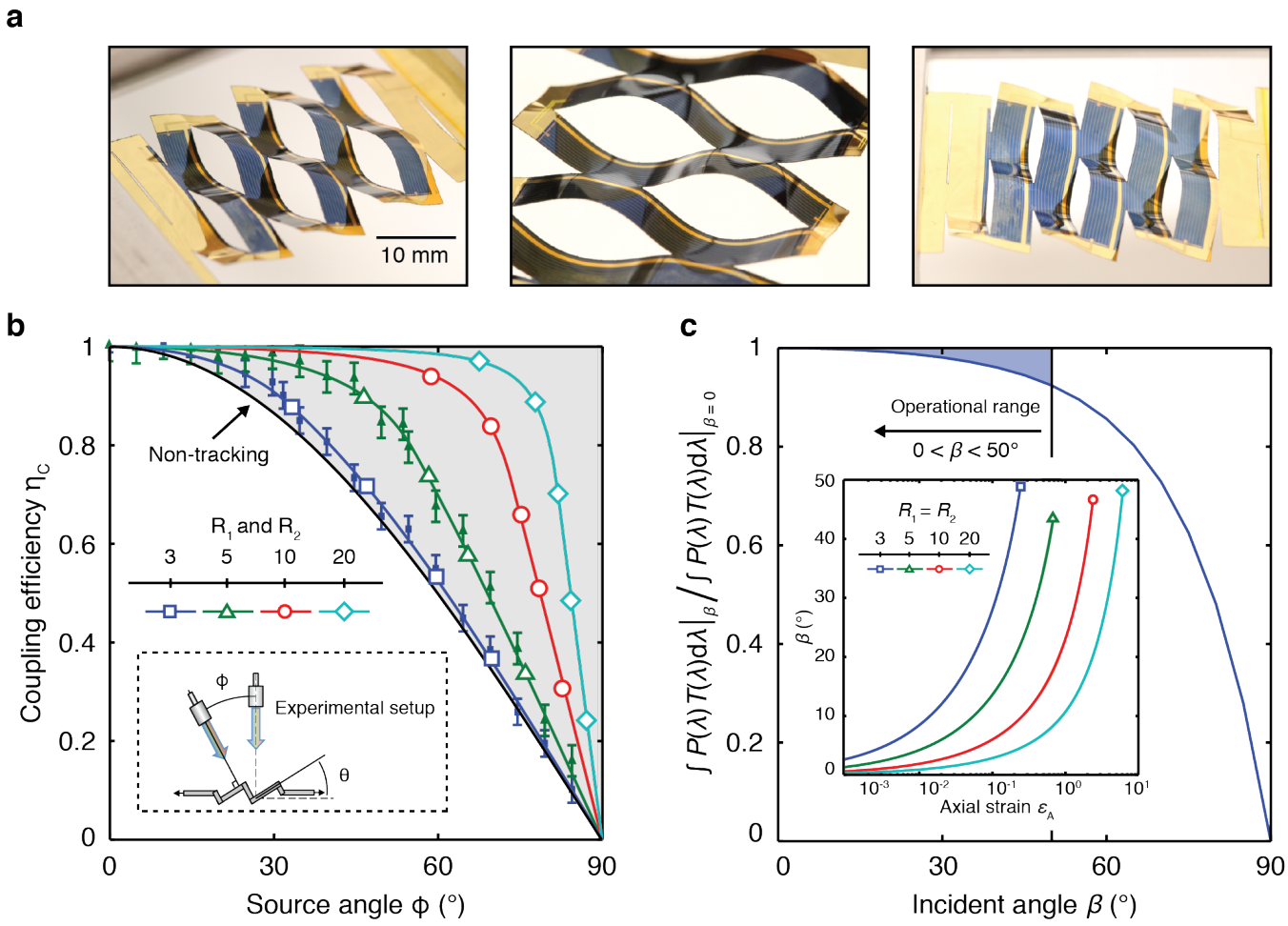

Figure 2.20 (a) Integrated thin-film, GaAs solar cells mounted by cold weld bonding on a Kapton® carrier substrate, as used for testing. Here, L_C = 15 mm, x = 3 mm, and y = 3 mm (R_1 = R_2 = 3). (b) Normalized solar cell short circuit current density $J_{SC}(\phi)/J_{SC}(\phi=0)$ versus source angle (ϕ) for two samples, where R_1 and R_2 = 3 and 5 (closed symbols). Also shown is simulated total coupling efficiency (η_C) from equation (31). (c) Normalized transmitted power for a typical bilayer ARC. *Inset*: β versus axial strain (ε_A).

direct measure of optical coupling in the presence of a suitable anti-reflective coating (ARC).

Performance for a typical bilayer ARC is shown in **Figure 2.20c**, where we plot normalized transmitted power integrated from 350 to 900 nm versus β (see **Figure 2.16b**). Of course, we must also consider β as a function of ε_A (inset) to fully understand the impact of reflection losses.

Interestingly enough, while each sample tracks to a different maximum ε_A (according to **Figure 2.20c**), β at ε_A (max) remains consistent, and below 50°. Over this operational range ($0 < \beta < 50°$), transmitted power is shown to remain relatively constant, highlighting the importance of a good ARC. An understanding of this response allows us to more accurately predict η_C.

2.4 Tracking performance

2.4.1 Geographic location, time of year, and time of day

As explained earlier, the location of the sun in the sky is defined by the zenith (ϕ) and azimuthal (α) angles (**Figure 2.17a**). Of course, the values of these angles changes as a function of geographic location, time of year, and of course, time of day. Therefore, to truly understand tracking performance as a function of real-world conditions, it was important to fully understand the motion of the sun.

The zenith angle (ϕ) is equal to 90° minus the altitude angle (a), the angle between the sun and the horizon:

$$\phi = 90° - a \tag{40}$$

where

$$a = \sin^{-1}\left[\sin\delta\sin\varphi + \cos\delta\cos\varphi\cos\left(HRA\right)\right] \tag{41}$$

In equation (41), δ is the declination angle, φ is the latitude of the location of interest, and HRA is the hour angle:

$$\delta = \sin^{-1}\left[\sin\left(23.45°\right)\right]\sin\left[\frac{360°}{365}\left(d - 81\right)\right] \tag{42}$$

$$HRA = 15°\left(LST - 12\right) \tag{43}$$

where d is the number of days since the start of the year and LST is the local solar time:

$$LST = LT + \frac{TC}{60} \tag{44}$$

where LT is the local time and TC is the Time Correction Factor (in minutes), which accounts for the variation of LST due to longitude variations within the time zone:

$$TC = 4\left(longitude - LSTM\right) + EoT \tag{45}$$

In Equation (45), $LSTM$ is the local standard time meridian and EoT is the equation of time, an empirical formula that corrects for the eccentricity of the Earth's orbit and the axial tilt of the Earth:

$$LSTM = \frac{360°}{24\ hr}\Delta T_{GMT} \tag{46}$$

$$EoT = 9.87\sin\left(2B\right) - 7.53\cos B - 1.5\sin B \tag{47}$$

where Δ_{GMT} is the difference of the local time (LT) from Greenwich Mean Time (GMT) in hours and

$$B = \frac{360°}{365}\left(d - 81\right) \tag{48}$$

The azimuthal angle (α) can be calculated as a function of declination angle (δ), latitude (in degrees), altitude angle (a), and the hour angle (HRA). In the solar morning (i.e. $LST < 12$)

$$\alpha = \cos^{-1}\left[\frac{\sin\delta\cos\left(latitude\right) - \cos\delta\sin\left(latitude\right)\cos\left(HRA\right)}{\cos a}\right] \tag{49}$$

and in the solar evening (i.e. $LST > 12$):

$$\alpha = 360° - \cos^{-1}\left[\frac{\sin\delta\cos\left(latitude\right) - \cos\delta\sin\left(latitude\right)\cos\left(HRA\right)}{\cos a}\right] \tag{50}$$

Sunrise and also be calculated for a given geographic location and time of year using the variables above:

$$Sunrise = 12 - \frac{1}{15^\circ}\cos^{-1}\left[-\tan(latitude)\tan\delta\right] - \frac{TC}{60} \tag{51}$$

$$Sunset = 12 + \frac{1}{15^\circ}\cos^{-1}\left[-\tan(latitude)\tan\delta\right] - \frac{TC}{60} \tag{52}$$

The effects of geographic location and time of year on the position of the sun are shown in **Figure 2.21a** and **2.21b**, respectively. Specifically, zenith (ϕ) and azimuthal (α) angles are shown for Phoenix, AZ (blue, dashed line) and Ann Arbor, MI (red, solid line) on the summer solstice (June 22) in **Figure 2.21a** and for Phoenix, AZ on June 22 (blue, dashed line) and November 11 (red, solid lines) in **Figure 2.21b**. The sunrise (open circles) and sunset (closed circles) times are also denoted on the x-axis for each scenario. Parameters used to generate **Figure 2.21,** along with sunrise and sunset times calculated using equations (51,52) are provided in **Table 1**.

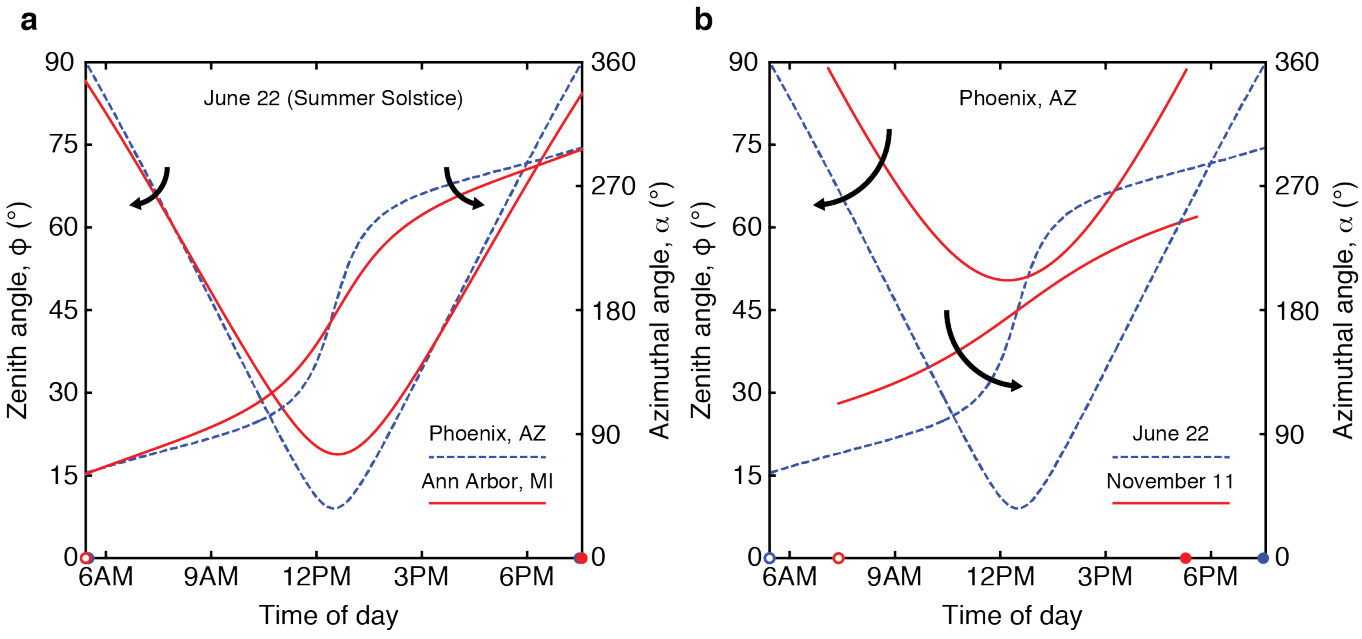

Figure 2.21 (a) Zenith angle (ϕ) versus time of day on June 22 (the Summer Solstice) in Phoenix, AZ (blue, dashed line) and Ann Arbor, MI (red, solid line). (b) ϕ versus time of day in Phoenix, AZ on June 22 (blue, dashed line) and November 11 (red, solid line).

Table 2.1 Geographic and time of year parameters used to generate results in Figure 2.21

		Phoenix, AZ		**Ann Arbor, MI**	
		July 20	November 11	July 20	November 11
Latitude (°)		32.45		42.2814	
Longitude (°)		-112.0667		-83.7483	
Δ_{GMT} (hr)		-7		-5	
Day of year, *d*		172	315	172	315
Sunrise		5:26am MST		7:28am EST	
Sunset	7:34pm MST	5:11pm EST			

2.4.2 Simulated solar tracking performance

The effect of kirigami geometry on power generation is compared to fixed planar cells and conventional single-axis systems in **Figure 2.22a** for Phoenix, AZ (33.45° N, 112.07° W) during the summer solstice (July 20). The power conversion efficiency (PCE) for each system was assumed to be 30%. As R_1 and R_2 increase, the system is shown to be more efficient in the morning and evening at angles far from the zenith, and the output power density increases accordingly. As shown in the inset, the output energy density for an optimized kirigami system approaches that of conventional single-axis tracking in the limit of large values of R_1 and R_2. This is indeed remarkable for a solar cell that remains essentially flat and without a change in macroscopic orientation.

Figure 2.22b shows power density and tracking angle (θ) as a function of time of day for $R_1 = R_2 = 5$, in Phoenix, AZ (33.45° N, 112.07° W) on July 20. Notice the stepwise change in θ near noon, which occurs in this particular geographic location and time of year to maximize coupling efficiency. Note that this would *not* occur in a geographic location and time of year for which the sun travels directly overhead (for example at the Equator, during the Summer Solstice). A

breakdown of coupling efficiencies (η_1, η_1, and η_C, per equations (30-32)) as a function of time of day is also shown for a tracker with $R_1 = R_2 = 5$ in **Figure 2.22c**.

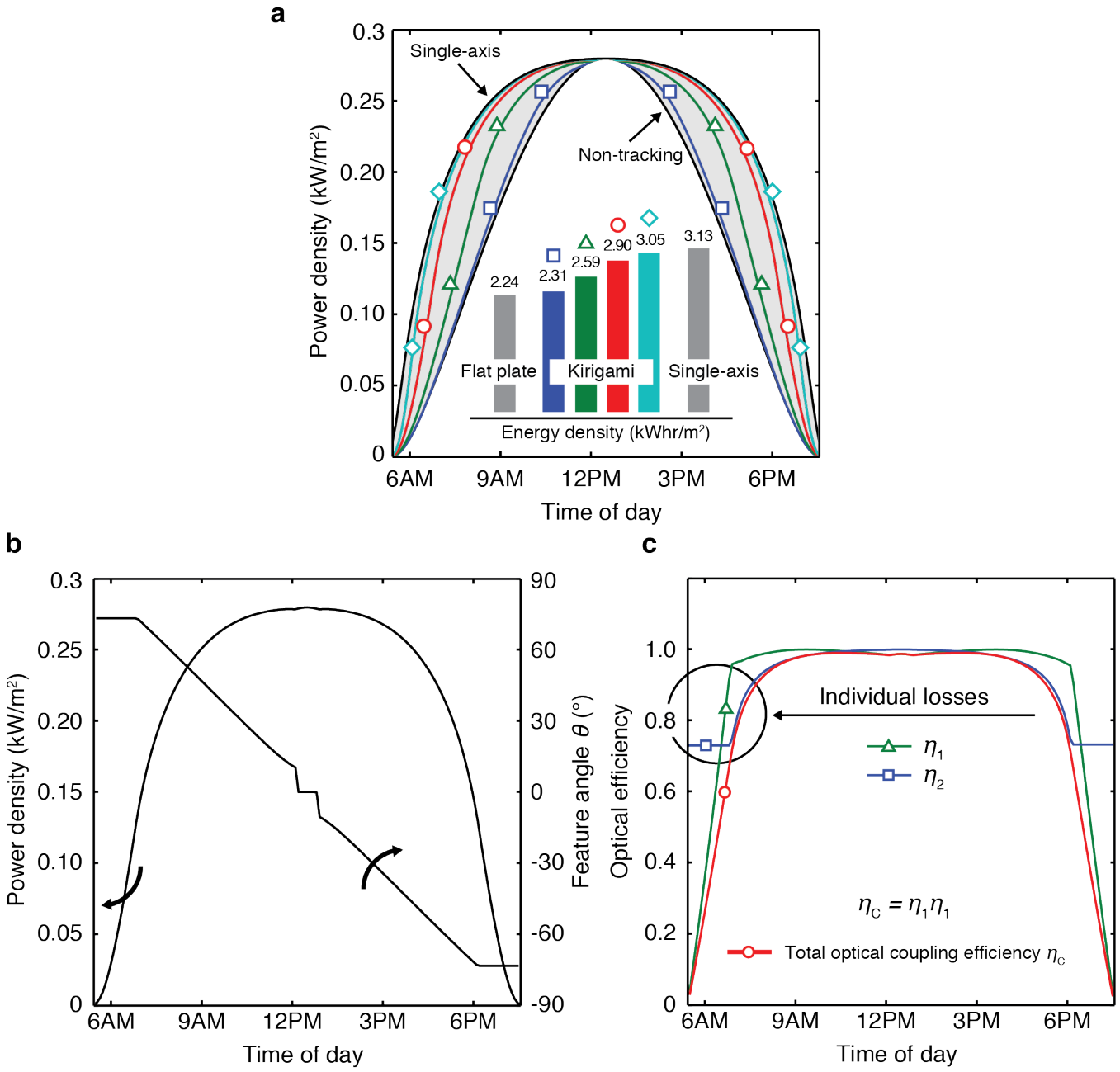

Figure 2.22 (a) Output electrical power density versus time of day for several kirigami cut structures, a stationary panel, and a conventional single-axis tracking panel in Phoenix, AZ (33.45° N, 112.07° W) on the Summer Solstice. *Inset*: Integrated power density (sunrise to sunset), where kirigami-enabled trackers are shown to approach near single-axis performance. (b) Detailed power density and feature angle (θ) versus time of day for kirigami tracker with $R_1 = R_2 = 5$. (c) Breakdown of coupling efficiencies (η_1, η_1, and η_C, per equations (30-32)) versus time of day for a kirigami tracker with $R_1 = R_2 = 5$.

2.5 Mechanical analysis

2.5.1 Beam deflection analysis

A typical linear kirigami pattern is shown in **Figure 2.23a**, for which the characteristic cut parameters are cut length (L_C) and the spacing between cuts in the transverse (ε_T) and axial (ε_A) directions. Upon stretching the sample, instabilities defined by the cut geometry cause shearing along the length of cut, and a subsequent elongation of the sample and decrease in width. The resulting shape of each substructure may be considered purely geometric, and is shown in **Figure 2.23b**. Each kirigami structure may be represented as a number of bending beams, where each beam has a length (L_B) of ($L_C - x$)/4 (**Figure 2.23c**). These beams are connected in series in the axial direction and in parallel in the transverse direction. The following is a derivation of total force acting on the structure as a function of displacement (ΔL).

Beam theory provides that the displacement (d) of a cantilever beam of length (L) as a function of material properties, area moment on inertia (I), and force (F) is:

$$d = \frac{FL^3}{3EI} \tag{53}$$

where E is the Young's modulus of the material, and:

$$I = \frac{ab^3}{12} \tag{54}$$

where a is the dimension of the beam normal to the direction of bending and b is the dimension of the beam in the direction of bending.

Each complete cut consists of four total beams – two beams connected in series (**Figure 2.23c**), both of which are then connected in parallel to another pair (**Figure 2.23b**). Each cut is then connected in parallel with other cuts within the same row, and each row is connected in series with each row along the axial length of the sample. Accordingly, we can approximate the

total force required to deflect the structure out of the plane of the sheet (d) as a function of material properties and system geometry:

$$F = \frac{16 N_C E y^2 t^3}{L_0 \left(L_C - x\right)^3} d \tag{55}$$

where N_C is the number of cuts per row (cuts which intersect the boundary of the sample are taken as one half of a cut), E is the Young's Modulus of the material, x and y are the spacing between cuts in the transverse and axial direction, respectively, L_0 is the initial sample length as measured from the first cut to the last, and L_C is the cut length.

To calculate deflection of the structure in the plane and direction of axial strain, we consider the relationship between d and the total instantaneous length of the sample (L) as shown in **Figure 2.23d**. Using the law of cosines:

$$d = \sqrt{L^2 - y^2} \tag{56}$$

Next, we relate displacement in the plane and direction of axial strain (ΔL) by considering the relationship between L and the initial length (L_0):

$$L = L_0 + \Delta L \tag{57}$$

Substituting equations (56,57) into equation (55) yields the total force (F) as a function of material, cut geometry, and true displacement (ΔL):

$$F = \frac{16 N_C E y^2 t^3}{L_0 \left(L_C - x\right)^3} \sqrt{\left(L_0 + \Delta L\right)^2 - y^2} \tag{58}$$

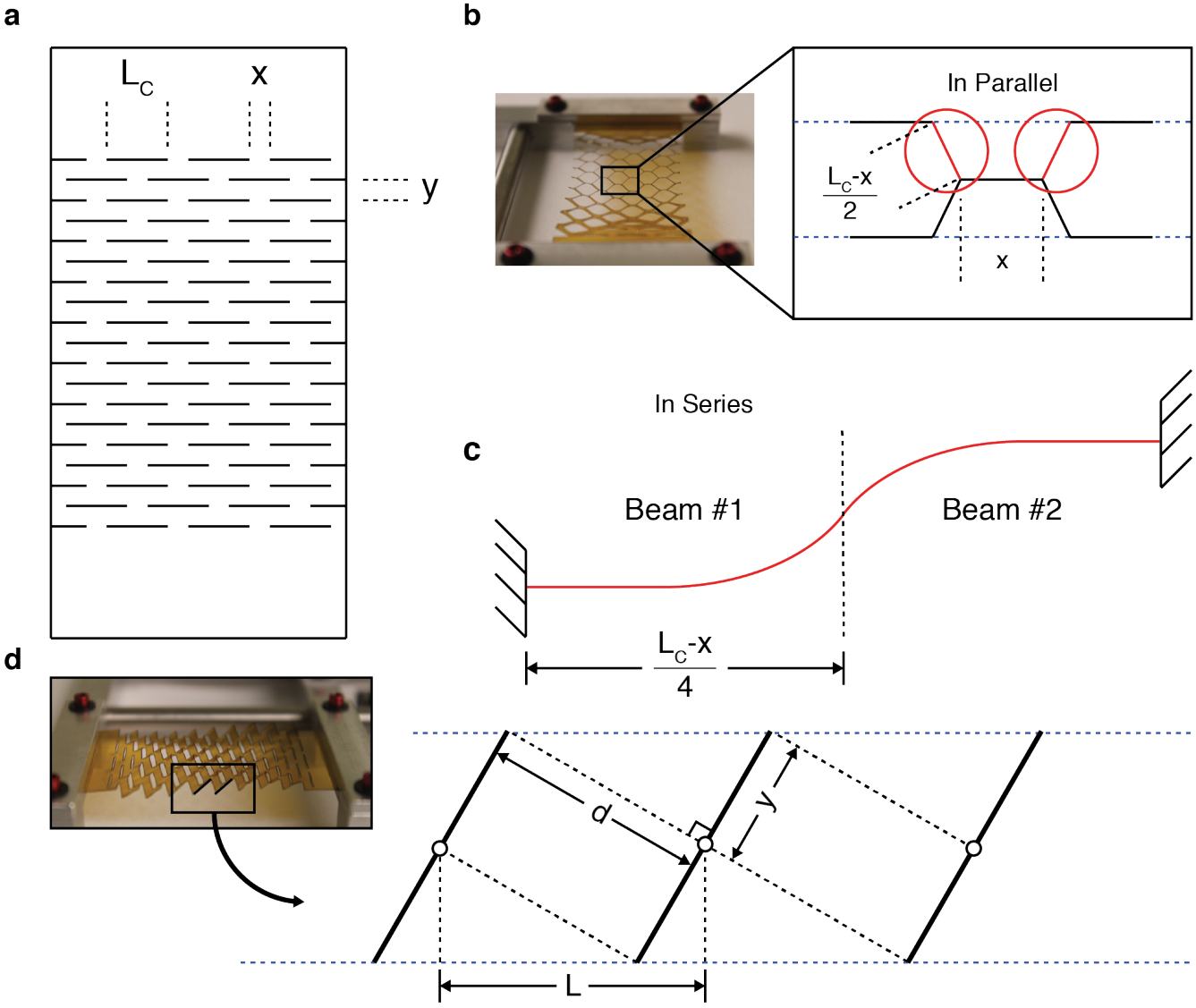

Figure 2.23 (a) Schematic of linear kirigami pattern, showing cut length (L_C) and the spacing between cuts in the transverse (ε_T) and axial (ε_A) directions. (b) The bending portion of the kirigami structure is shown in red. (c) Each bending portion can be expressed as two fixed-end cantilever beams joined in the middle, where the length of each beam is ($L_C - x$)/4. (d) Side view schematic showing displacement per row (d_R) and axial spacing between cuts (y).

2.5.2 Experimental mechanical response

Equation (58) allows us to qualitatively predict the effects of cut parameters and materials selection on mechanical response. Specifically, as the cuts become longer and the spacing between cuts becomes smaller (i.e. as R_1 and R_2 increase), we would expect displacement for a

given force to increase. This is potentially important when considering a solar tracking application, where the force required to strain the tracker is directly proportional to the power requirements of the linear actuator required for motion. As the force required to strain the tracker decreases, so do the power requirements and costs associated with the actuation method.

Figure 2.24a plots experimental stress (σ) versus axial strain (ε_A) for linear kirigami samples with $R_1 = R_2 = 3$, 5, 10, and 20 (geometries shown in **Figure 2.15b**). As expected, the stress required to strain a given sample decreases as R_1 and R_2 increase. We can also consider the strain energy (E_ε), which is the force (F) integrated over axial displacement (dx), and represents the total energy required to actuate the structure over one cycle:

$$E_\varepsilon = \int F\,dx \tag{59}$$

E_ε is plotted against R_1 and R_2 in the inset of **Figure 2.24a** and decrease as R_1 and R_2 increase.

Recall that geometric response as derived in **Section 2.2** could be simplified in terms of R_1 and R_2. In other words, regardless of the values of L_C, x, and y, the relationships between tracking angle (θ), transverse strain (ε_T), and axial strain (ε_T) would be the same for equivalent values of R_1 and R_2. Here, however, the mechanical properties are very much a function of the specific values of L_C, x, and y, as calculated qualitatively in equation (58). **Figure 24b** plots stress (σ) versus axial strain (ε_A) for two linear kirigami structures. $R_1 = R_2 = 5$ for each structure, however the specific values of L_C, x, and y are different. Specifically, $L_C = 10$ mm, $x = 2$ mm, and $y = 2$ mm for the first structure (red), and $L_C = 15$ mm, $x = 3$ mm, and $y = 3$ mm for the second structure (blue).

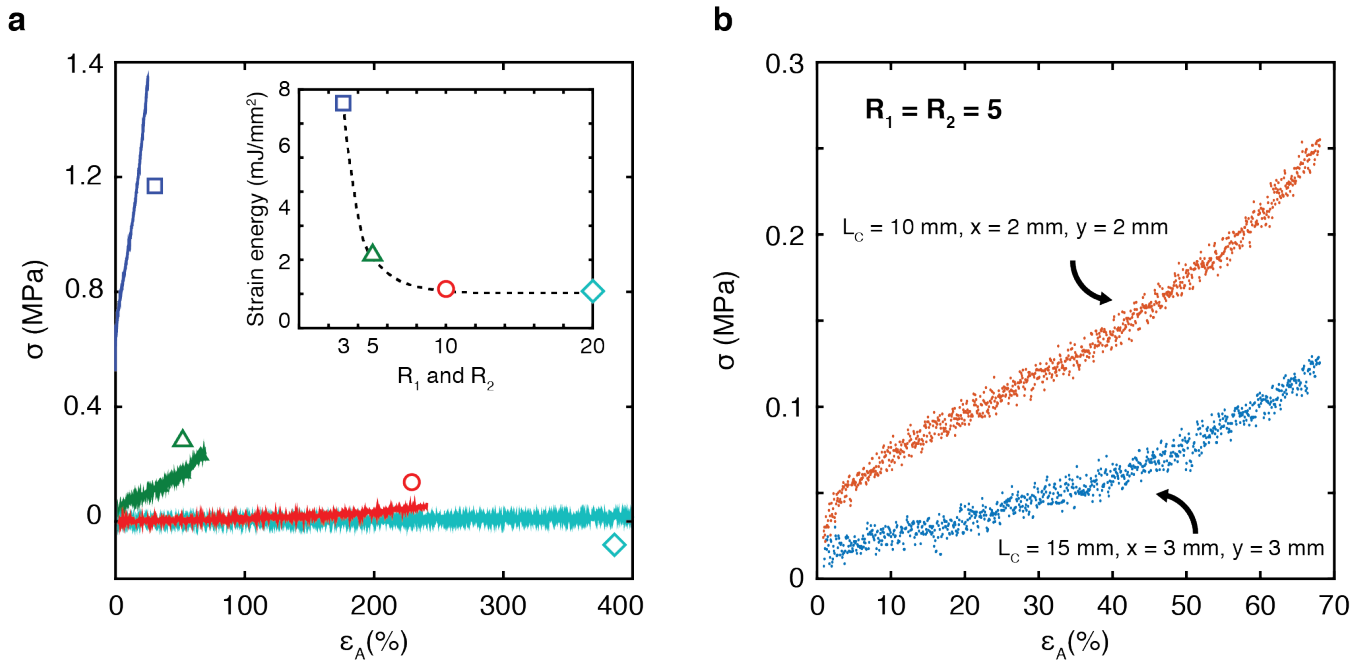

Figure 2.24 (a) Measured stress (σ) versus axial strain (ε_A) for linear kirigami structures where R_1 = R_2 = 3, 5, 10, and 20. *Inset*: Strain energy (E_ε) versus R_1 and R_2, where strain energy represents the amount of energy required to strain the structure over one cycle. (b) Measured σ versus ε_A for two linear kirigami structures with R_1 = R_2 = 5. Notice the change in mechanical response due to specific cut parameters (L_C, x, and y), something that was not considered in the geometric response models from Section 2.2.

2.6 Effect of cyclic strain on performance

2.6.1 Origins of plastic deformation

As a force is applied to the end of the kirigami structures, regions of localized stress at the edges of each cut cause (1) plastic deformation proportional to the geometry of the kirigami structure and, for large enough stress concentrations, (2) propagation of a crack along the direction of the cut. To help quantify the amount of plastic deformation, it is helpful to look at the change in strain energy (E_ε) versus cycle number. To this point, **Figure 2.25a** plots E_ε versus cycle number for a Kapton® kirigami structure where R_1 = R_2 = 5 (L_C = 10 mm, x = 2 mm, and y = 2 mm). The inset shows the change in the stress (σ) versus axial strain (ε_A) curve as measured experimentally.

We will quantify the relative decrease in E_ε from the first to last cycle, and call it strain energy fade (E_F):

$$E_F = \frac{E_\varepsilon\big|_1 - E_\varepsilon\big|_n}{E_\varepsilon\big|_1} \tag{60}$$

where $E_\varepsilon|_1$ and $E_\varepsilon|_n$ are the strain energies from the first and last cycles, respectively. As shown in **Figure 2.25a**, the strain fade for a Kapton® sample with $R_1 = R_2 = 5$ ($L_C = 10$ mm, $x = 2$ mm, and $y = 2$ mm) is relatively high, at ~17%. Most of this plastic deformation occurs at the edges of the cuts, and in particular at high strains when the structure is near its geometric limits. Thankfully, by considering geometric (**Section 2.2**) and mechanical (**Section 2.5**) response, it is possible to optimize the structure to minimize strain fade and plastic deformation. To this point, **Figure 2.25b** plots strain energy versus cycle number for three kirigami structure, where $R_1 = R_2 = 3$, 5, and 10. Also shown in the inset are the strain fades associated with each structure over 500 cycles. As you can see, increasing the length of each bending element with respect to it's with (mechanical analysis) and increasing R_1 and R_2 (geometric analysis) help to decrease strain fade (and plastic deformation), as expected. Specifically, for a kirigami structure with $R_1 = R_2 = 10$ ($L_C = 20$ mm, $x = 2$ mm, and $y = 2$ mm), strain fade was measured to be only ~3%.

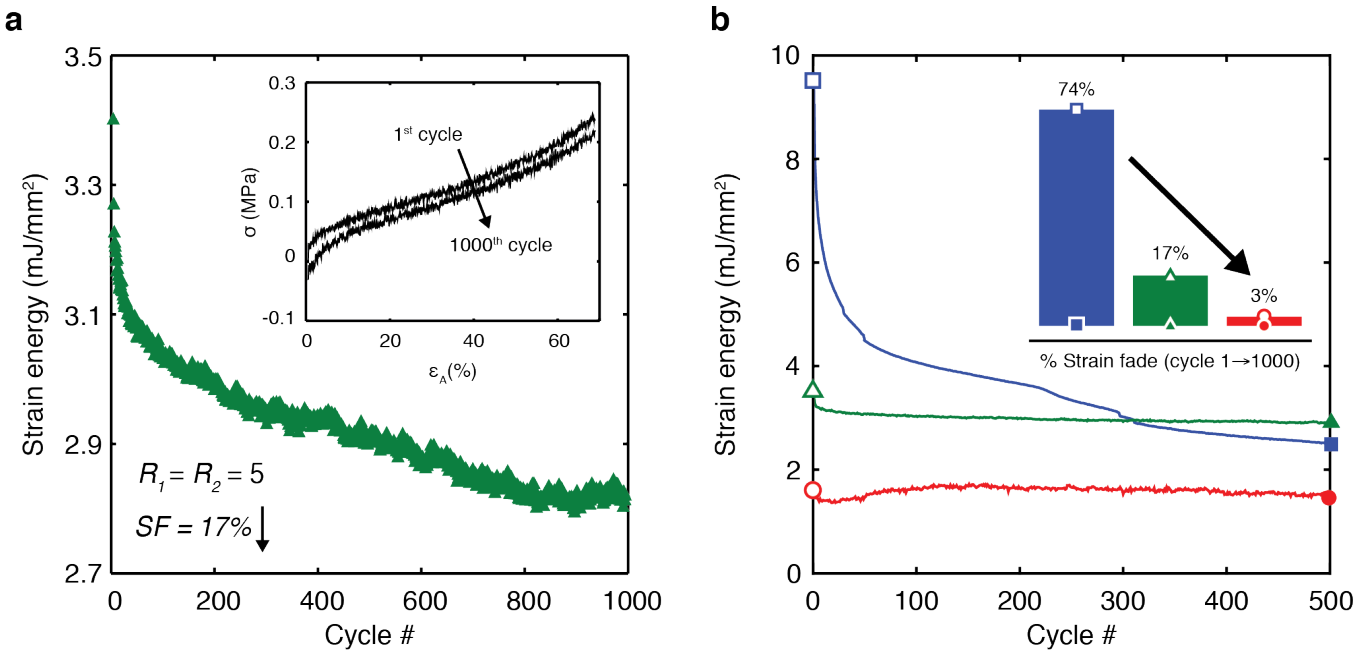

Figure 2.25 (a) Strain energy (E_ε) versus cycle number for a Kapton® kirigami tracker where $R_1 = R_2 = 5$ (L_C = 10 mm, x = 2 mm, and y = 2 mm). *Inset*: Change in stress (σ) – strain (ε_A) response from the first to last cycle, as was used to calculate E_ε. (b) Effect of system geometry on strain fade. For a kirigami tracker with $R_1 = R_2 = 10$ (L_C = 20 mm, x = 2 mm, and y = 2 mm), strain fade was measured to be only ~3% (a significant improvement over other tracker geometries).

In samples with low R_1 and R_2 (i.e. < 5), we must also consider the propagation of a crack along the direction of the cut due to high stress concentrations at high strains. To this point, consider **Figure 2.26a**, which shows microscope images of a kirigami sample with $R_1 = R_2 = 3$ (L_C = 6 mm, x = 2 mm, and y = 2 mm) at cycles 1, 5, 10, 20, 50, and 100. Notice the presence and growth of a crack, which starts at the edge of the cut (area of high stress concentration) and extends further in the direction of the cut as cycling continues. As the crack grows, keep in mind that the effective cut length (L_C) increases and the spacing between cuts in the transverse direction (x) decreases (R_1 increases). As this happens, we would expect the overall stress on each cut to decrease, and thus crack propagation to be hindered. We see this exact phenomenon is **Figure 2.26b**, where normalized crack length is plotted versus cycle number. Notice that most of the crack propagation occurs in the first 10 cycles, after which stress concentrations are

decreased and crack propagation is slowed. Microscope images of the same kirigami samples with $R_1 = R_2 = 3$ are shown in **Figure 2.26c** at various strains during cycle 1000 to better show the geometric effects of crack propagation. Of course, crack propagation is not an issue in samples with large values of R_1 and R_2 thanks to the significant reductions in stress concentrations as outlined previously. To this point, the Kapton® kirigami tracker with $R_1 = R_2 = 10$ ($L_C = 20$ mm, $x = 2$ mm, and $y = 2$ mm) shown in **Figure 2.26d** shows no crack propagation even after 1000 cycles.

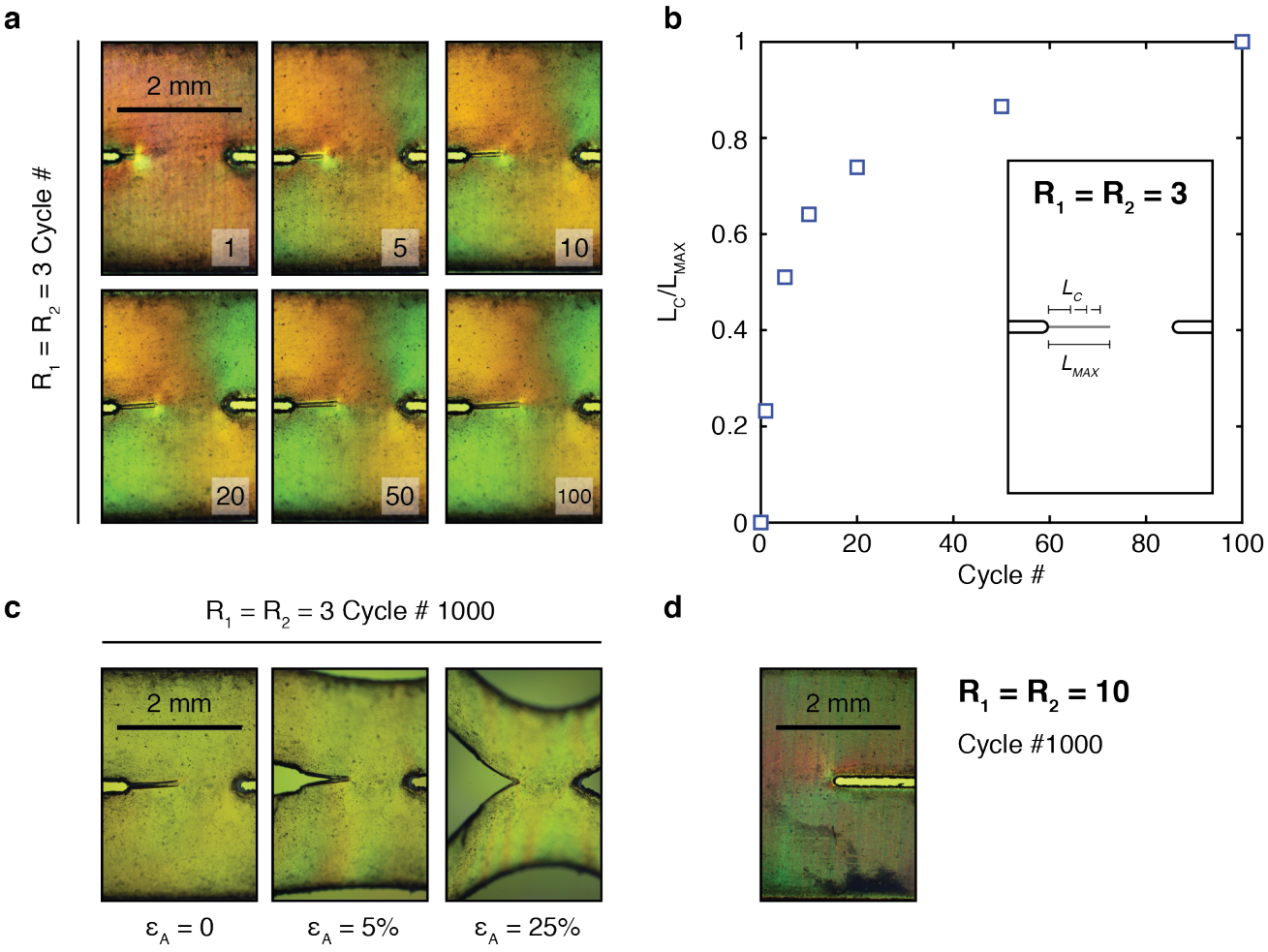

Figure 2.26 (a) Images of Kapton® sample after 1, 5, 10, 20, 50, and 100 cycles, where $R_1 = R_2 = 3$. Notice the formation and extension of the crack at the edge of the cut. (b) Normalized crack length (see inset) versus cycle number. (c) Images of Kapton® sample at various strains during cycle #1000. (d) Image of Kapton® sample after 1000 cycles, where $R_1 = R_2 = 10$.

2.6.2 Solar cell performance

Due to the unique geometric response and mechanical properties of the kirigami tracker, it is important to study their effect on solar cell performance both as a function of tracking angle (θ) and cyclic strain. It is helpful to review some basic concepts used to understand and quantify solar cell performance. The power conversion efficiency (*PCE*) of the solar cell is defined as the electrical power out divided by the optical power in:

$$PCE = \frac{J_{SC} V_{OC} FF}{P_{inc}} \tag{61}$$

where the short-circuit current density (J_{SC}) is the current density measured at zero bias (i.e. 0 V), the open-circuit voltage (V_{OC}) is the voltage measured at zero current density, and P_{inc} is the power density of incident light. The fill factor (*FF*) is a measure of the "squareness" of the current-voltage curve and compares the operating maximum power point (*MPP*) to the ideal maximum power point that would theoretically occur while operating at both J_{SC} and V_{OC} simultaneously.

$$FF = \frac{J_{MPP} V_{MPP}}{J_{SC} V_{OC}} \tag{62}$$

To determine the effects of strain on solar cell performance, we needed to eliminate any geometric effects – in particular, any changes in performance due to ε_T needed to be suppressed. To this point, consider the kirigami tracker shown in **Figure 2.27a**. Each facet of the bending elements contains a separate solar cell, all of which could be tested in-situ and independent from each other. For this specific test, and to mitigate any losses due to geometric necking, performance of the central solar cell (outlined in red) was considered. **Section 2.7.2** provides more information on the geometric layout of these test-only solar trackers, and also outlines the electrode breakout pattern (blue line in **Figure 2.27a**) used for testing.

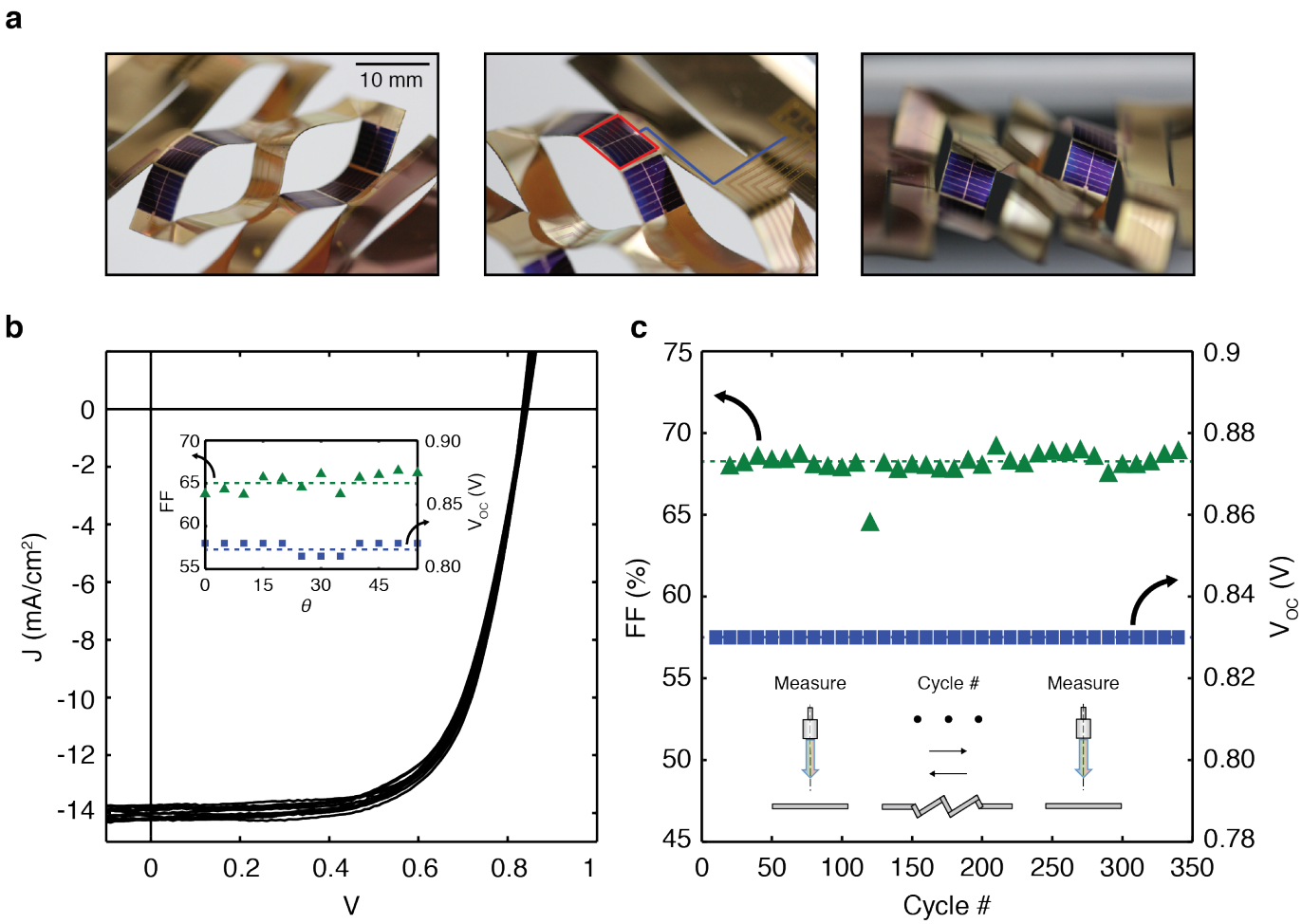

Figure 2.27 (a) Images of the modified kirigami solar tracker used to measure solar cell performance. Specifically, the solar cell highlight in red and the electrical contacts highlighted in blue were used. (b) Current density – voltage curves (*J-V*) curves as measured from $\theta = 0°$ to $\theta = \theta^*$. *Inset*: There is no change in fill factor (*FF*) or open circuit voltage (V_{OC}), signifying negligible effects of strain on cell performance. (c) Similarly, there was negligible effect of repeated cycling on *FF* or V_{OC} (measured over 350 cycles, from $\theta = 0°$ to $\theta = \theta^*$).

The modified solar tracker with $R_1 = R_2 = 3$ (L_C = 15 mm, x = 5 mm, and y = 5 mm) was strained to track a moving light source to the maximum tracking angle (θ_{MAX}), and the subsequent current-voltage (*J-V*) curves are shown in **Figure 2.27b**. Performance parameters (*FF* and V_{OC}) associated with each *J-V* curve are also shown as a function of tracking angle (θ) in the inset of **Figure 2.27b.** Notice that there is no significant change in the *J-V* curves, nor any large deviations in either *FF* or V_{OC}, signifying that stress concentrations due to tracking have negligible effect on system performance. A similar analysis was also conducted to see the effect

of repeated strain on system performance. Specifically, the solar tracker was repeatedly strained to the optimal extent of tracking (θ*) as defined in **Figure 2.19** while the source was kept constant at $\phi = 0°$. Cell performance (i.e. *FF* and V_{OC}) was measured every 10 cycles, when $\theta = 0°$ (and consequently $\phi = 0°$), for 350 cycles (to simulate approximately one year of operation). As is shown in **Figure 2.27c**, there was no apparent change in cell performance over 350 cycles, signifying that kirigami solar trackers may be applicable for long-term deployment.

2.7 Methods

2.7.1 Laser cutting

A 25W (10.6 μm wavelength) carbon dioxide (CO_2) laser cutter (Universal Laser Systems) was used for the majority of fabrication throughout my research. The laser was also used to produce shadow masks for vacuum thermal evaporation, 3D machining of simple fixture components, and also bonding as described in **Chapter 3**. Laser cut width and quality are controlled by changing the power (%), speed (%), pulses per inch (*PPI)* and optics. **Table 2** provides a starting point for laser settings and optics choice for several materials and material thicknesses. Note that the ratio between power and speed is extremely important, and should be used as a starting point. If the user desires a faster or slower speed (for example, to accommodate higher throughput or better quality, respectively) both power and speed should be adjusted accordingly so that the ratio between them remains consistent. In addition, the 1.5" optic should only be used for materials with a thickness less than 0.25" – due to the short focal length and shallow depth of field, thicker materials will experience a sloping of the sidewalls of the cut. Accordingly, for materials thicker than 0.25", the 2" optic should be used. Air assist (*AA*) and exhaust should also be used at all times, however for samples that require optical clarity (see **Chapter 3**) *AA* may be turned off as needed.

Table 2.2 Laser parameters for chosen materials and thicknesses

Material	Thickness	Rating (W)	Power (%)	Speed (%)	PPI	Optic
PET-G	0.5 mm	25	100	30	1000	1.5”
PET	50 μm		5	10		
	100 μm		5	10		
Acrylic	3 mm		100	5		2”
Paper	0.1 mm		30	100		1.5”
Tyvek	0.1mm		30	30		
Kapton	25 μm		30	30		
	50 μm	50	2	2.5	500	2”
		25	2	4	1000	1.5”
	75 μm		80	50		
	125 μm		4	2		

2.7.2 Fabrication of kirigami solar trackers

The fabrication of kirigami solar trackers can be broken down into the following areas: (1) Fabrication of gallium arsenide (GaAs) solar cells, (2) design and fabrication of electrical contacts, and (3) final alignment and laser cutting. Here, we will discuss each process in detail.

2.7.2.1 Fabrication of gallium arsenide (GaAs) solar cells

Kyusang Lee was responsible for the fabrication of the GaAs solar cells. Solar cell design was in accordance with a specific kirigami pattern, such that laser cutting would not affect solar cell performance (see **Figure 2.28** – blue squares). Fabrication steps were as follows. Epitaxial layers of *p-n* junction GaAs active material on an AlAs sacrificial layer were grown by gas-source molecular beam epitaxy (GSMBE) on a 2 inch-diameter (100) GaAs substrate. For the ND-ELO process, 0.2 μm thick GaAs buffer layer followed by a 20 nm thick AlAs sacrificial layer were grown, first. Then, following inverted photovoltaic device layers were grown: 0.1 μm thick, 5×10^{18} cm^{-3} Be-doped GaAs *p*-contact layer, 0.025 μm thick, 2×10^{18} cm^{-3} Be-doped

$Al_{0.20}In_{0.49}Ga_{0.31}P$ window layer, 0.15 μm thick, 1×10^{18} cm^{-3} Be-doped *p*-GaAs emitter layer, 3.0 μm thick, 2×10^{17} cm^{-3} Si-doped *n*-GaAs base layer, 0.05 μm thick, 6×10^{17} cm^{-3} Si-doped $In_{0.49}Ga_{0.51}P$ back surface field (BSF) layer, and 0.05 μm thick, 5×10^{18} cm^{-3} Si-doped *n*-GaAs contact layer. The sample was then coated with a 300 nm thick Au layer by e-beam evaporation, and bonded to a 50 μm-thick E-type Kapton® sheet (also coated in 300 nm Au layer) using cold weld bonding by applying a pressure of 4 MPa for 3 minutes at a temperature of 200 °C. After bonding, the photovoltaic epitaxial active region and Kapton® carrier were isolated from the bulk wafer using epitaxial lift-off (ELO) by selectively removing the AlAs sacrificial layer in dilute (15%) hydrofluoric acid (HF) solution at room temperature. After ND-ELO, a Pd(5 nm)/ Zn(20 nm)/ Au(700 nm) front metal contact was patterned using photolithography. Then, the device mesas were similarly defined using photolithography and subsequent chemical etching using H_3PO_4:H_2O_2:deionized H_2O (3:1:25). The exposed, highly Be-doped 150 nm thick *p*+ GaAs contact layer was selectively removed using plasma etching. After annealing the sample for 1 hr at 200 °C to facilitate ohmic contact formation, the sidewalls were passivated with 1 μm-thick polyimide applied by spin coating. After curing the sample at 300 °C for 30 min, the polyimide was selectively removed by photolithography and plasma etching. The external contact pad was patterned with Ti (10 nm)/Au (500 nm). Finally, a bilayer anti-reflection coating consisting of TiO_2 (49 nm) and MgF_2 (81 nm) was deposited by e-beam evaporation[26-28].

2.7.2.2 Design and fabrication of electrical contacts

For conventional, planar solar cells, static hard or soft probing is typically used during cell characterization. Specifically, each cell is electrically connected directly at the site of the cell. Kirigami trackers, on the other hand, are both flexible and dynamic systems, where the point of electrical connection is constantly changing as a function of ε_A and θ. Accordingly, we needed to design and fabricate an "electrode breakout pattern" that would allow us to maintain electrical connection irrespective of the position of the solar tracker. Two electrode breakout patterns are shown in **Figure 2.28**. The breakout pattern in **Figure 2.28a** was used to measure cell performance as a function of ε_A, θ, and cycle number (**Section 2.6.2**), where cell *B* was measured to ensure constant J_{SC}. The breakout pattern in **Figure 2.28b** was used for all other testing, and in particular, for coupling efficiency measurements as outlined in **Section 2.3.3**. Each breakout pattern was fabricated using a Kapton® shadow mask, and subsequent deposition of 10nm of Ti and 500 nm of Au.

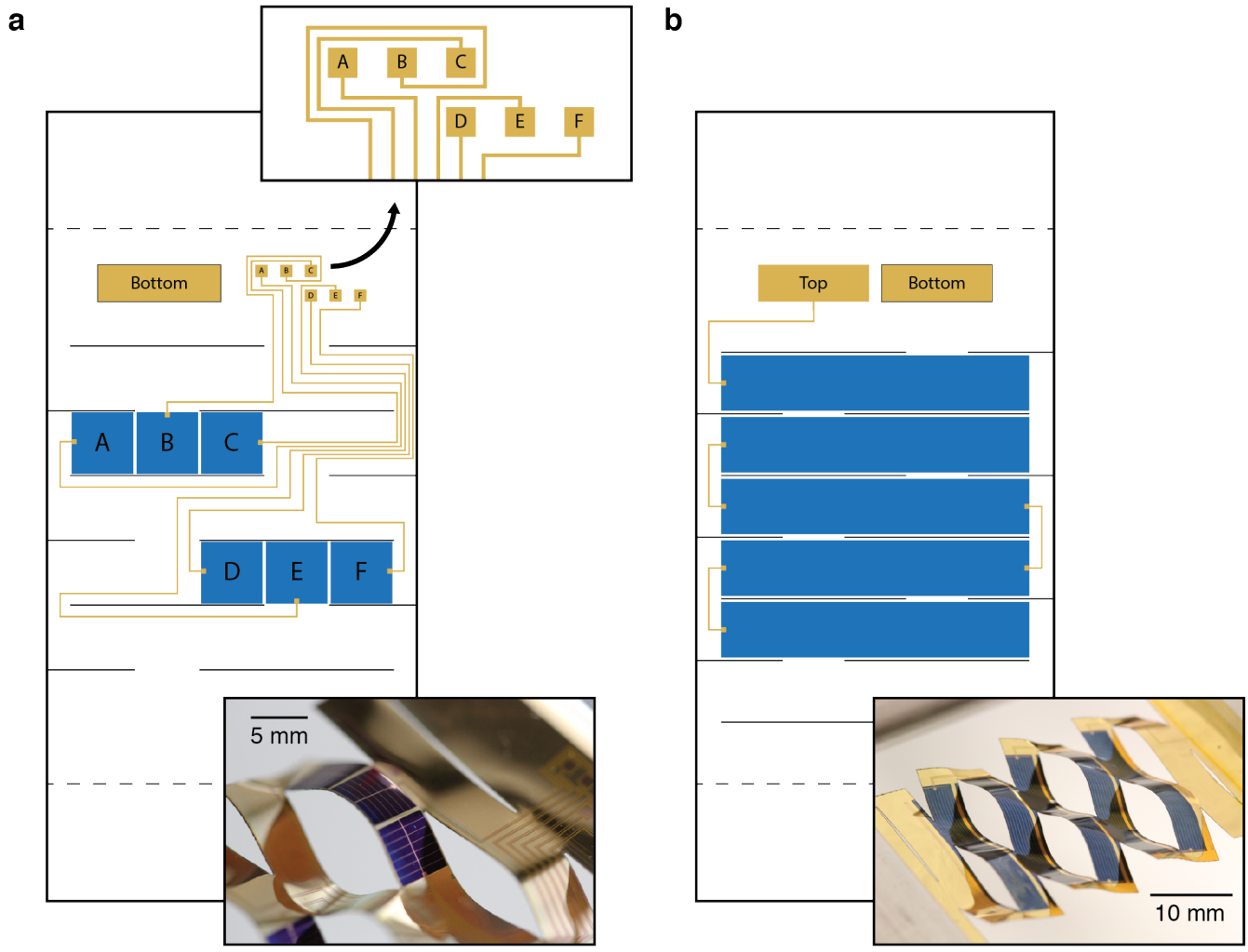

Figure 2.28 (a) Schematic of electrode breakout pattern and image of kirigami solar tracker used to measure cell performance as a function of ε_A, θ, and cycle number (Section 2.6.2). (b) Schematic of electrode breakout pattern and image of kirigami solar tracker used to measure coupling efficiency as a function of θ. In each schematic, electrode pattern (gold), solar cells (blue), and kirigami cut patterns (black, solid lines) are shown.

2.7.2.3 Alignment and laser cutting

Following solar cell fabrication on Kapton® and deposition of electrical contacts, the laser cutter was used to define the kirigami tracking geometries outlined previously. Importantly, special care was taken when aligning the solar cells with the laser cutter to minimize damage during dicing.

2.7.3 Measurement of axial and transverse strain

The kirigami structures detailed in **Section 2.2** were systematically strained using the homemade micro-strain apparatus shown in **Figure 2.29**. The straining process was imaged *in situ* using two cameras: one facing directly downwards to capture transverse strain (ε_T) and a second facing the edge of the sample to capture the change in feature angle (θ). Both cameras captured the axial strain (ε_A). The resulting images were analyzed using *ImageJ* (Rasband, W.S., Bethesda, Maryland, USA), where a global calibration scale was used to define measurement lengths. It should be noted that, in some cases, limitations imposed by the range of motion of the apparatus prohibited data collection at high strain values (i.e. we could not reach θ_{MAX}).

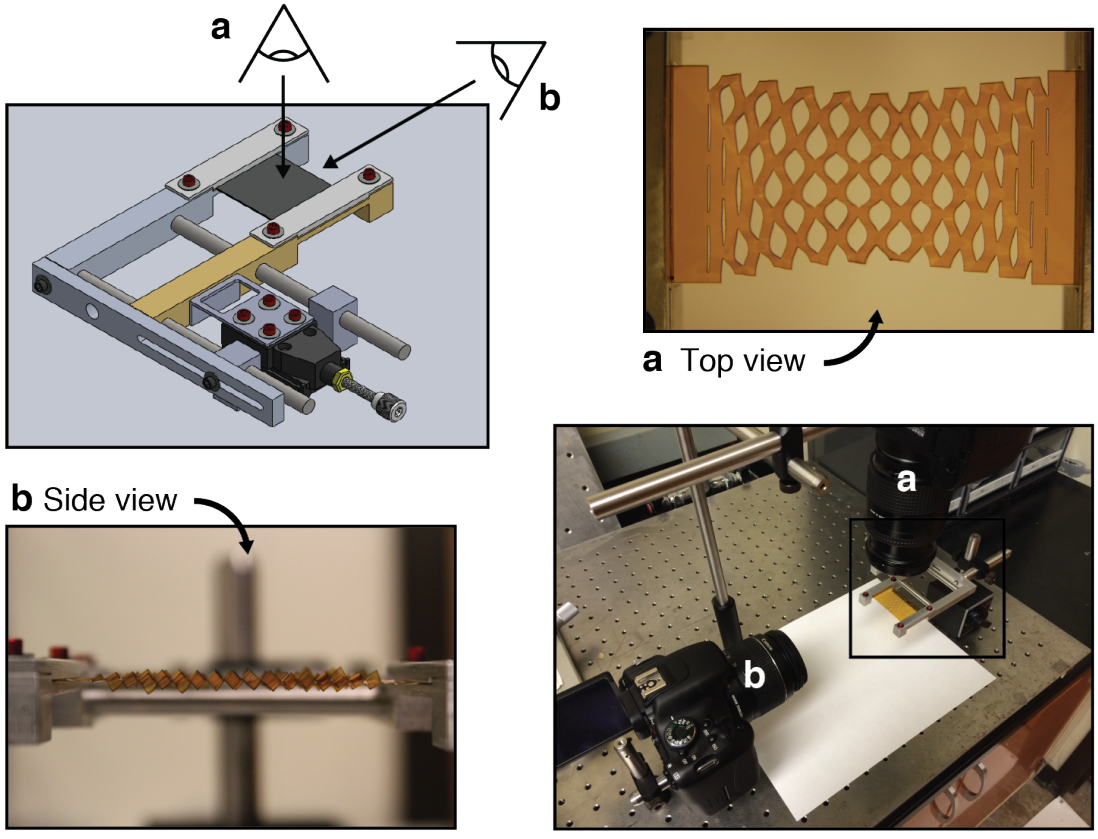

Figure 2.29 Experimental test setup used to measure ε_T (top view, a) and θ (side view, b). Two cameras were used to capture ε_T and θ, and the images were subsequently analyzed using *ImageJ*.

2.7.4 Electrical characterization of kirigami trackers

An image (a) and schematic (b) of the test setup used for solar cell and kirigami tracker characterization are shown in **Figure 2.30**. The kirigami solar trackers were strained using the micro-strain apparatus in **Figure 2.29** to tracking a moving AM1.5G light source (Oriel solar simulator, model 91191 with Xenon arc lamp and AM 1.5 global filter, simulated 1 sun, 100 mW/cm^2 intensity) from $\theta = 0°$ to $\theta = \theta^*$. The *J-V* characteristics (i.e. J_{SC}, V_{OC}, and *FF*) were measured at each angle using a semiconductor parameter analyzer (SPA, Agilent 4155B), in increments of five degrees, from normal incidence ($\phi = 0°$) to $\phi = 90°$. To determine the effect of cycling on cell performance, the solar tracker was repeatedly strained to $\theta = \theta^*$, while the source was kept constant at $\phi = 0°$. Cell performance (i.e. J_{SC}, V_{OC}, and *FF*) was measured every 10 cycles, when $\theta = 0$ (and consequently $\phi = 0°$), for 350 cycles (to simulate approximately one year of operation).

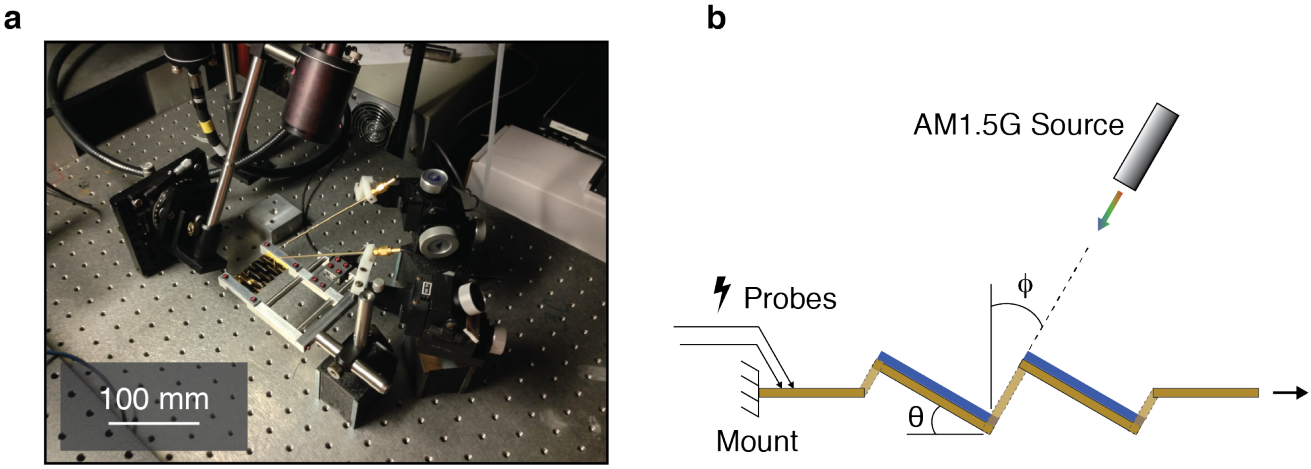

Figure 2.30 (a) Image and schematic (b) of test setup used for solar cell characterization.

2.7.5 Mechanical characterization of kirigami structures

The stress-strain characteristics (**Section 2.6.1**) of the Kapton® kirigami structures were measured using a TA.XT*Plus* Texture Analyzer (Texture Technologies, Hamilton, Massachusetts, USA) and the *Exponent* (Texture Technologies, Hamilton, Massachusetts, USA) software package. For the Kapton® trackers, the sample length as measured from the first cut to the last cut in the axial direction was 36 mm. Each sample was strained from $\theta = 0°$ to $\theta = \theta^*$, and the resulting stress-strain behavior was recorded. This process was repeated 1000 times, and the resulting curves were integrated to find the strain energy, per equation (59). The strain fade was calculated as the percentage difference in strain energy between cycle 1 and cycle 1000, per equation (60).

2.8 Conclusions

In this chapter we introduced a novel method of integrated, low-profile solar tracking whereby a simple kirigami pattern in thin-film gallium-arsenide solar cells enables tracking at the substrate level simply by stretching the sheet. The new tracker was inherently lightweight and less susceptible to wind loading, which greatly reduces tracking system complexity, size, and cost, while also enabling new applications. System performance was considered as a function of cut geometry, materials selection, and geographic location, and optimized performance was shown to generate ~40% more energy per solar cell area over the course of a day relative to a stationary, flat panel module. Electrical and mechanical robustness were also considered with implications towards long-term solar tracking applications (i.e. >10,000 actuation cycles). The methodologies and design principles are universal, and will be applied to develop new mechanical and optoelectronic systems going forward. The results from this work were published in *Nature Materials*[14] and *Nature Communcations*[32] in 2015.

Chapter 3 Integrated Concentrators and Solar Tracking

3.1 Introduction

Concentrator photovoltaics (CPVs) use concentration optics to focus incident light onto a small solar cell and are often integrated with mechanical tracking to maintain high concentration factors (CFs) as the sun moves through the ecliptic[33]. These systems reduce the required area of expensive solar cell needed to generate a desired power output, and also increase solar cell efficiency at higher light intensities[34]. Conventional CPV systems typically use either Fresnel lenses[35,36] and reflectors[37] or parabolic troughs[38,39] and dishes[40-42] as the optical components. Other systems use waveguides[43,44], free-form optics[45], or microcell tracking[46] to accomplished similar tasks. Unfortunately, many of these systems require costly optical components and complex fabrication techniques or bulky tracking components to support system weight and resist wind loading.

Despite these disadvantages, CPV systems have the potential to reduce module costs significantly. Consider the conventional parabolic reflector system shown in **Figure 3.1**, which consists of a parabolic dish reflector, structural components to support weight and facilitate tracking, and a planar solar cell that is fixed at a given focal length from the surface of the reflector. In this type of system, the power concentration factor (CF_P) is defined as the maximum

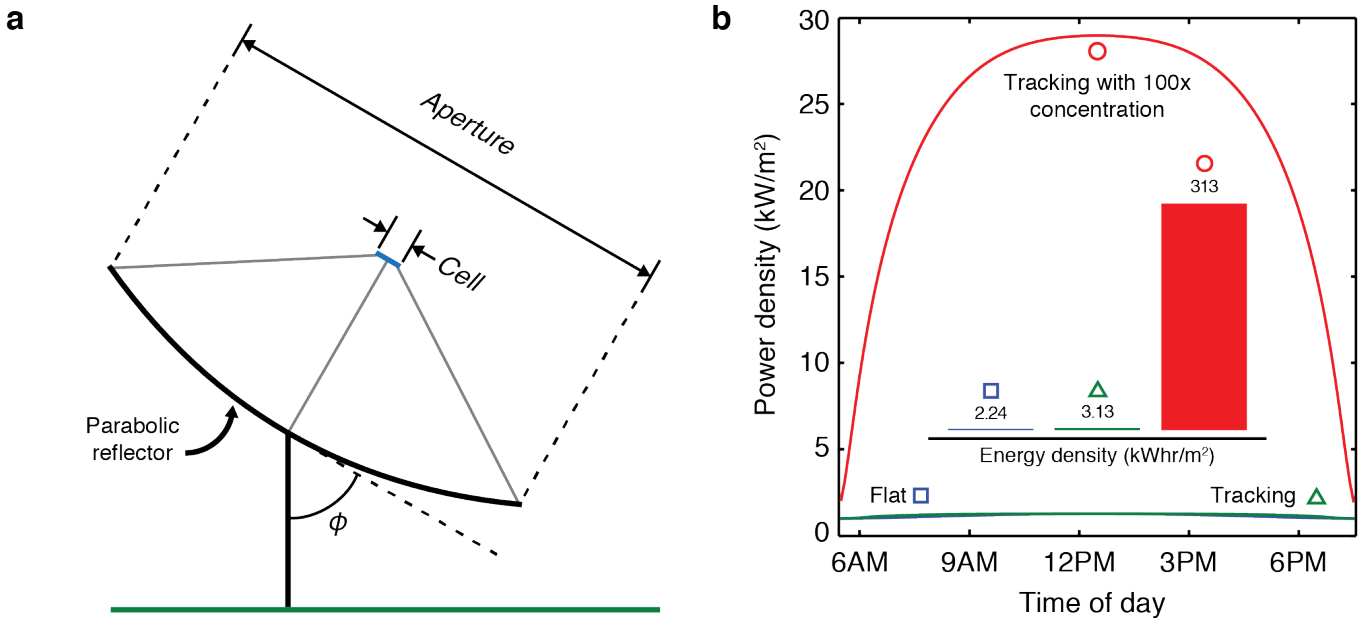

Figure 3.1 (a) Schematic of conventional CPV systems, showing reflector, cell area, and aperture area. (b) Power density per active material area versus time of day for a flat panel module, single-axis solar tracker, and single-axis solar tracker with 100x concentration. *Inset*: Energy density per active material for the systems described in (b).

power generated from the solar cell under concentration divided by the maximum power generated from the solar cell of equivalent area under one sun.

$$CF_P = \frac{P_{MPP}\big|_{Concentration}}{P_{MPP}\big|_{1\ Sun}} \tag{63}$$

Assuming there is no change in cell performance under concentration, CF_P is equivalent to the optical concentration factor (CF_O). CF_O is a geometric factor, and can be approximated as the area of the aperture of the concentrator divided by the area of the solar cell – a concentration efficiency term (η_{CF}) is also included to account for reflection losses or misalignment:

$$CF_O = \frac{A_{Aperture}}{A_{Cell}}\eta_{CF} \tag{64}$$

The performance of a solar tracker with 100x concentration is compared to flat panel and tracking-only systems in **Figure 3.1b**. Notice the significant increase in power density per active

material area, as well as the substantial increase in electrical energy density generated over the course of the day (~140x that of a flat panel and ~100x that of a tracking system without concentration). For a module in which the cost of semiconductor is ~80% of the total BOS costs (for example, the 29% PCE GaAs module discussed in **Chapter 2**), this decrease in the cost of semiconductor would result in a ~83% decrease in module cost!

In the sections that follow we will present a novel method of combing concentration optics and low-profile solar tracking. We will discuss the design of the kirigami tracker and concentration optics to maximize performance and also consider several new fabrication techniques to potentially lower manufacturing costs. We will also present the effects of cell temperature and electrical contact design on solar cell performance, and detail the systematic approach used to maximize performance.

3.2 System and concentrator design

3.2.1 Overview of system design

Thermoformed plastic optics have been used previously in the design of non-tracking, mini-compound concentrators[38]. These systems are inherently low cost and well suited for high throughput fabrication. Similar systems may be combined with kirigami design principles to develop a low-profile solar tracker with integrated concentrator optics. An overview of the original design concept is shown in **Figure 3.2a**. Specifically, the system consisted of two kirigami trackers that were offset from each other a distance equal to the focal length of the parabolic reflector. One tracker would control motion of the parabolic reflector, and the other would control the motion of the solar cells. On the other hand, a more integrated approach is shown in **Figure 3.2b**. Specifically, two kirigami trackers are bonded together, and focal length is achieved *via* an offset in the position of the cell along the axis of the focal length of the

parabolic reflectors. The design shown in **Figure 3.2b** not only significantly simplifies system design, but also enables the use of several new fabrications techniques as outlined in the following sections.

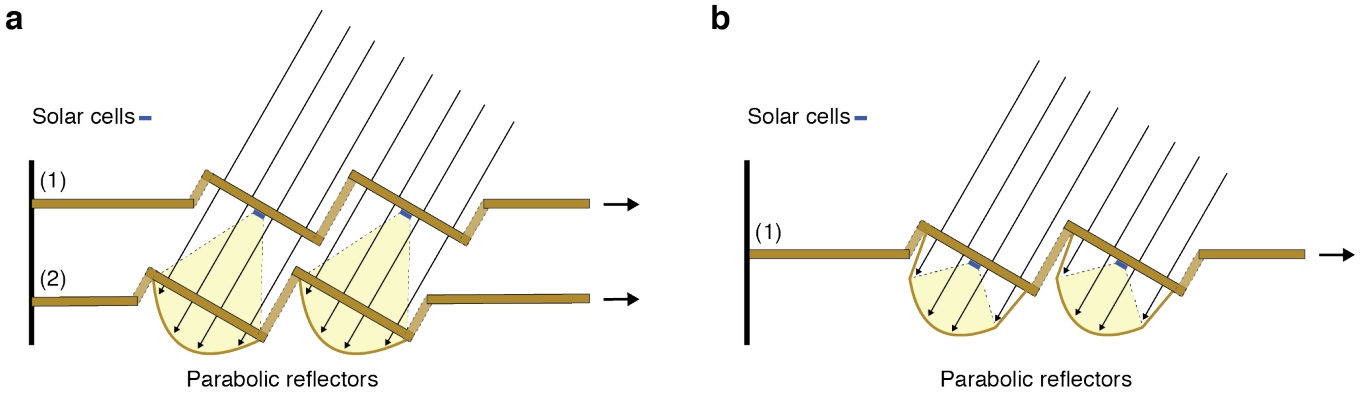

Figure 3.2 (a) Schematic of two separate kirigami trackers used to control function of (1) solar cells and (2) parabolic reflectors. (b) Integrated systems where solar cells and concentrator components are bonded together and focal length is achieved via offset in concentrator design.

3.2.2 Tracker geometry

To enable system integration and allow for thermoforming of the concentration optics into the actual kirigami tracker, modification of the simple linear pattern kirigami design previously discussed by Lamoureux *at al*. was required[32]. In addition to designing for manufacturing, other effects of kirigami design on mechanical response, semiconductor utilization, and subsequent concentration efficiencies needed to be considered. Consider now the kirigami structures shown in **Figure 3.3**. While different shapes to the individual elements or "unit cells" are possible and potentially useful (e.g. octagons, etc.), these will suffice for the present discussion. Each is a modification of the linear kirigami pattern discussed in Chapter 2, comprised of large static elements suited for thermoforming and thin, bending structures to facilitate tracking. Interestingly enough, because the linear kirigami pattern is the topological basis for each shown

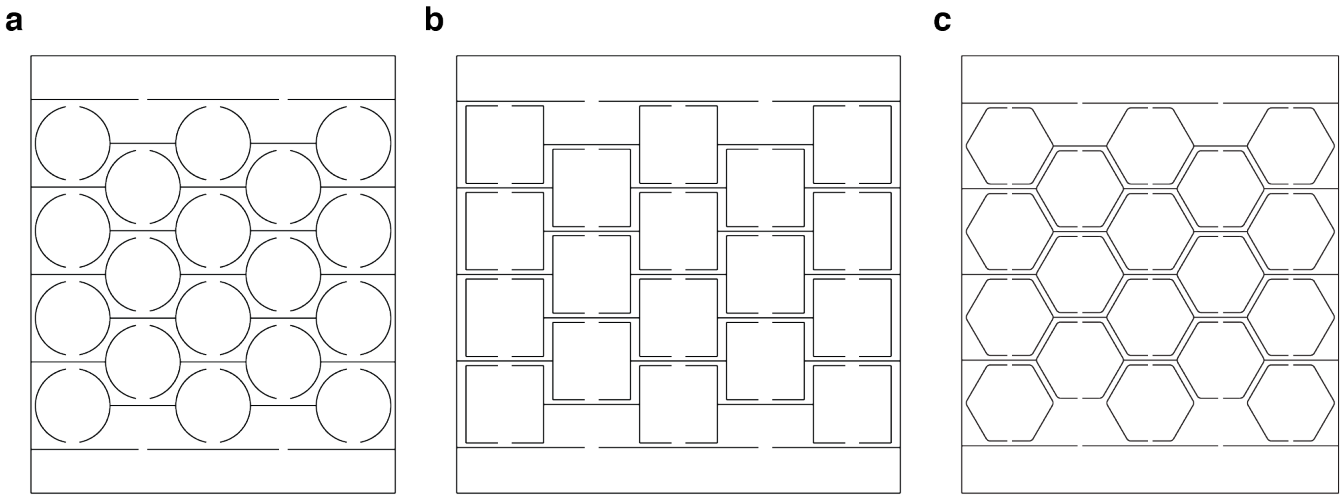

Figure 3.3 Several kirigami designs, where the shape of the rigid elements (and thus concentrator apertures) are either (a) circular, (b) square, and (c) hexagonal.

geometry, the relationship between tracking angle (θ) and axial strain (ε_A) remains the same, provided the rigidity of the "struts" involved in deflecting is unchanged – an assumption that can and will be relaxed:

$$\theta = \cos^{-1}\left(\frac{1}{\varepsilon_A + 1}\right) \tag{11}$$

To help in selecting an appropriate tracker and concentration geometry, it was important to quantitatively consider each tracker shown in **Figure 3.3**. Specifically, we considered the effect of the design on mechanical response, concentrator design, materials utilization, and packing density. Accordingly, a theoretical geometric efficiency (η_G) was calculated for each structure:

$$\eta_G = \eta_{CD}\eta_{PD}\eta_{SCU} \tag{65}$$

where η_{CD} is the optical efficiency assuming a concentrator aperture corresponding to the shape of the rigid sections, η_{PD} is the packing density of the concentration optics in the plane of the original sheet, and η_{SCU} is the semiconductor utilization efficiency assuming a solar cell corresponding to the shape of the concentrator aperture. Here, η_{CD} was calculated using ray-tracing simulations (courtesy of Byungjun Lee), η_{PD} was calculated by dividing the total

concentrator aperture area by the total area of the kirigami structure, and η_{SCU} was calculated by dividing the usable solar cell area after dicing by the total solar area before dicing. A breakdown of individual and total efficiencies for each of the kirigami geometries is shown in **Table 3**. As a result of this analysis, the hexagonal kirigami pattern was chosen for further analysis and development.

Table 3.1 Individual and total efficiencies for circle, square, and hexagonal kirigami designs

	Circle (a)	**Square (b)**	**Hexagonal (c)**
η_{CD} (%)	100	78	88
η_{PD} (%)	91	100	100
η_{SCU} (%)	91	100	100
η_G (%)	**82.8**	**78**	**88**

3.2.3 Concentration optics

The parabolic shape is often used as the reflecting surface in CPV systems because of its unique geometric properties. Consider the parabola (red) shown in **Figure 3.4a**, where the height (h) is a function of aperture diameter (d) and focal length (f):

$$h = \frac{d^2}{16f} \tag{66}$$

In addition, notice that the angle (ρ) between a line parallel to the axis of the parabola (y) and the normal to the surface of the parabola is equivalent to the angle (ρ) between the normal to the surface of the parabola and the focal point (F). This geometric relationship, in combination with Snell's Law that states (for a single index of refraction) the angle of reflection equals the angle of incidence, means that all rays parallel to the parabola will be reflected to the focal point (F).

A parabola is a geometric curve that is infinite in extent, however, when designing a parabolic concentrator, one uses a truncated version of that parabola. The amount of truncation is referred to as the rim angle (ψ_R), as shown in **Figure 3.4b**, where:

$$\psi_R = \frac{1}{\left(d/8h\right) - \left(2h/d\right)} \tag{67}$$

Due to surface reflections at high incident angles, a ψ_R of 60° was used in this study. Going forward, other angles should also be considered for their effects on optical performance and fabrication.

A conventional design for a parabolic concentrator is shown in **Figure 3.4b**, where the solar cell is held physically away from the parabolic dish, typically using rigid bars. Unfortunately, this type of configuration is often heavy and requires addition components and complex fabrication techniques. Our adaptation of this design is shown in **Figure 3.4c**, where ψ_R and the focal length (f) are incorporated through an offset parabolic dish (solid red line) and a transparent top sheet (dashed red line) onto which the solar cells are mounted.

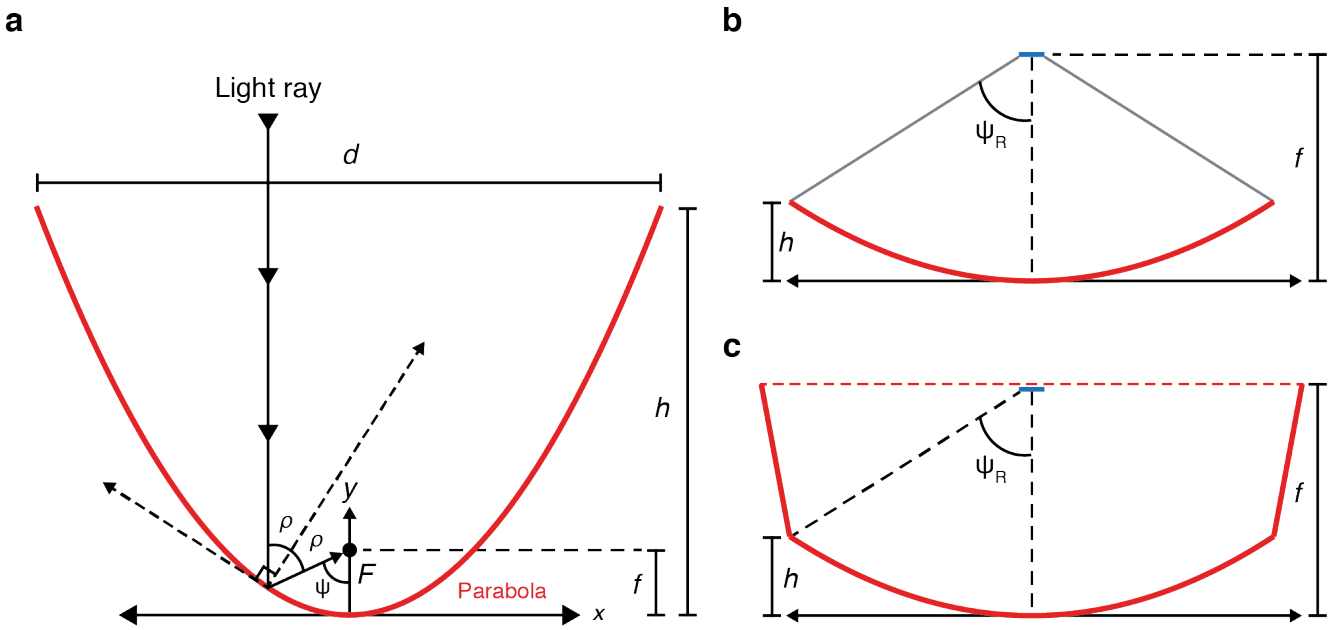

Figure 3.4 (a) Schematic of parabolic dish concentration, where light rays parallel to the axis of the parabola (y) are reflected to a focal point (F). (b) Schematic of a typical truncated parabolic dish, notating the extent of truncation in the form of rim angle (ψ_R). Notice that the solar cell (blue) is offset from the dish using rigid struts. (c) Schematic of modified parabolic dish, where molded parabola (solid red line) and transparent top sheet (dashed red line) are bonded together to form a single package.

3.2.4 Final design parameters

Final design selections are shown in **Figure 3.5**. Specifically, an overview of the hexagonal cut pattern, parabolic dishes (silver), electrical contact pattern (gold), and positioning of solar cells (blue) is shown in **Figure 3.5a**. An up close view of the final concentrator design is shown in **Figure 3.5b**, where the molded sheet is 0.5 mm PETG, the top transparent sheet is 50 μm PET, and patterned GaAs is used as the solar cell material. The evolution of the tracker side-profile as a function of axial strain is shown in **Figure 3.5c**.

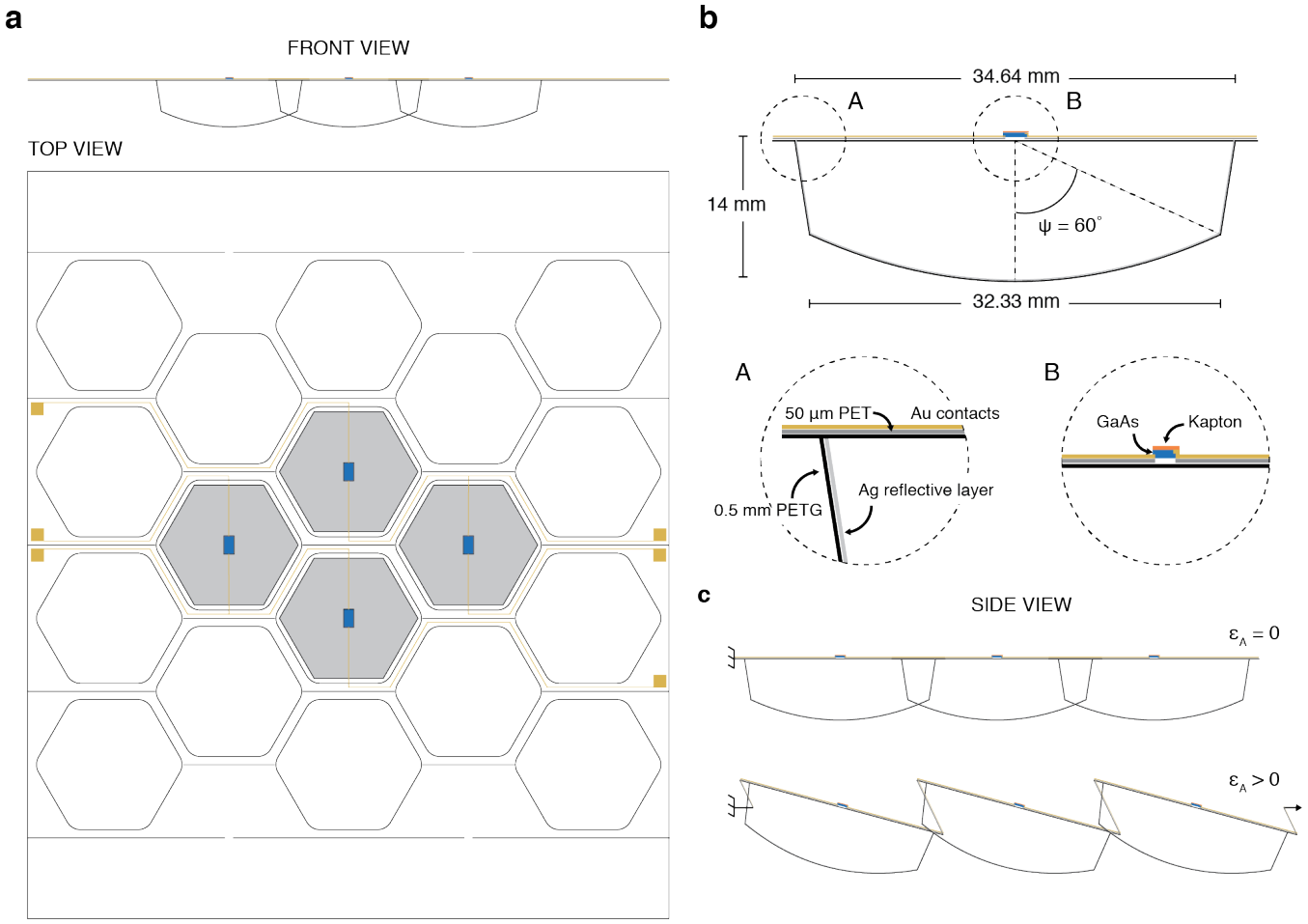

Figure 3.5 (a) Schematic of final system design, showing hexagonal cut pattern, thermoformed parabolic dishes (silver), electrical contact pattern (gold), and placement of GaAs solar cells (blue). (b) Detailed schematic of parabolic concentrator, where ψ_R was chosen to be 60°. (c) Evolution of tracker side-profile as a function of axial strain.

3.3 Fabrication

Due to the unique geometric design of the integrated system, several new fabrication techniques were required. Vacuum molding, rapid prototyping of shadow masks, vacuum thermal evaporation, cold-weld bonding, and laser cutting, among other techniques, will be discussed in this section.

3.3.1 Parabolic concentrators

The mold used in vacuum-assisted thermoforming of the parabolic concentrators in a 0.5 mm polyethylene terephthalate glycol modified (PETG) sheet is shown in **Figure 3.6a**. This negative mold technique was chosen over positive mold techniques to minimize transfer of non-uniformities from the surface of the mold (potentially occurring during the machining process) to the inside surface of parabolic reflectors. A schematic of results from negative molding is shown in **Figure 3.6b**. An overview of parabolic concentrator fabrication is shown in **Figure 3.6c**. (1) First, a 0.5 mm thick PETG sheet is laser cut and placed into the center of the vacuum mold shown in **Figure 3.6a**. (2) The mold/sheet combination is then placed into a convection oven and heated until the mold itself is ~100 °C. The glass transition temperature (T_g) of PETG is ~88 °C, which means that a mold temperature of 100 °C is sufficient to soften the PETG. Once 100 °C is reached, vacuum is then pulled on the mold and held for one minute. After one minute the vacuum is turned off, the sample is removed from the oven, and cooled. (3) After removing the deformed PETG sheet from the mold, vacuum thermal evaporation (VTE) and a shadow mask are used to selectively deposit 0.5 μm of silver (Ag) into the wells of the parabolas. An image of the final deformed PETG sheet with Ag is shown in **Figure 3.6c**.

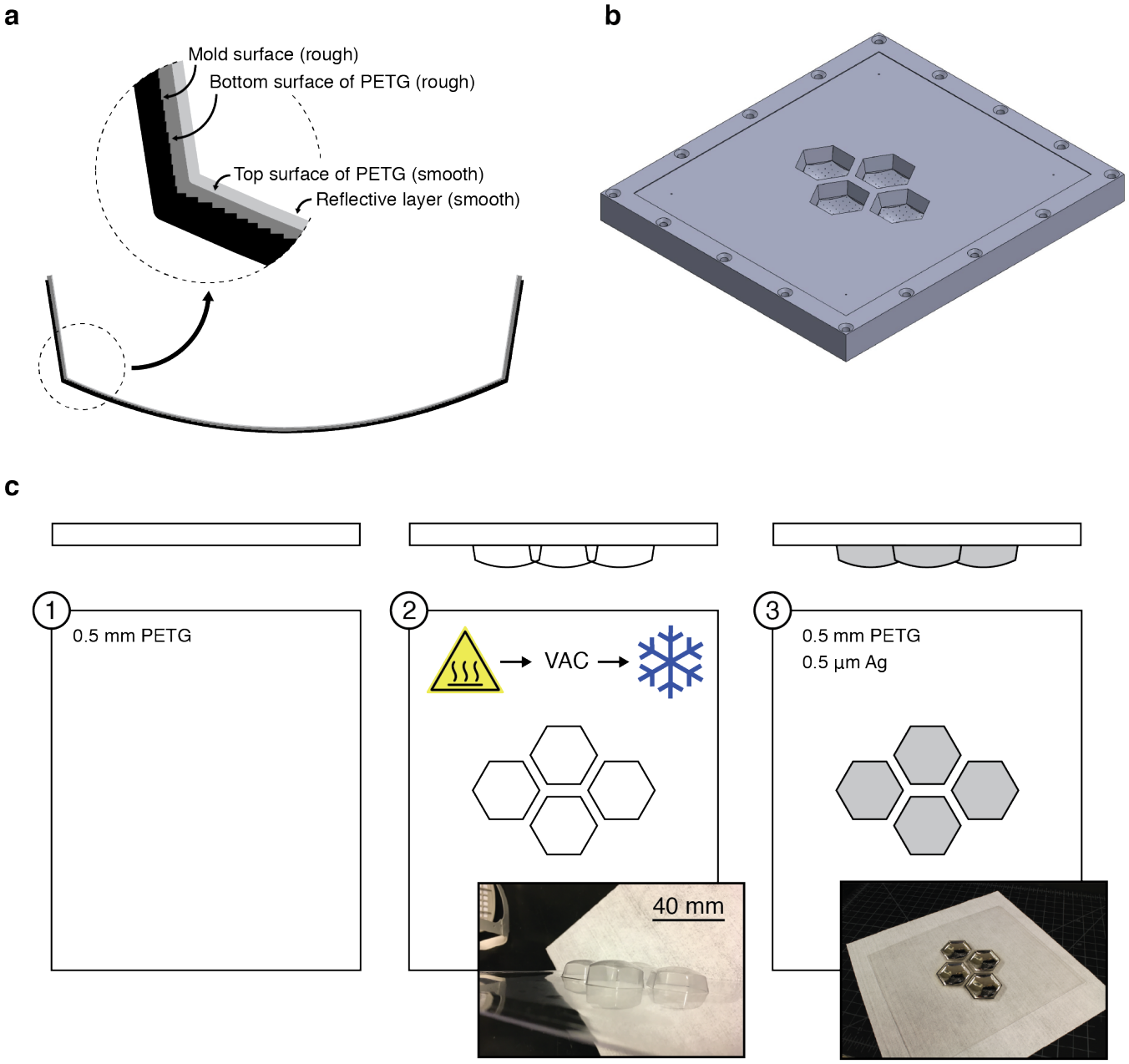

Figure 3.6 (a) Schematic of negative molding, where non-uniformities in mold are not transferred to reflective surface of concentrators. (b) Solidworks model and image of mold used for vacuum-assisted thermoforming of parabolic concentrators. (c) Fabrication steps for molded concentration optics in bottom sheet – (1) cutting of 0.5 mm PETG sheet, (2) vacuum-assisted thermoforming of parabolic concentrators, and (3) selective deposition of 0.5 µm of silver using vacuum thermal evaporation.

3.3.2 Electrical connections and top sheet

The top sheet system consists of a thin transparent film (here a polyethylene terephthalate (PET) sheet), metal (here gold) electrical contacts, through-thickness windows to minimize surface reflection, and finally bonded (here, gallium-arsenide) solar cells. An overview of fabrication is shown in **Figure 3.7**. (1) A transparent 50 μm PET sheet is cut equal in area to the 0.5 mm PETG bottom sheet. (2) A shadow mask is then used to selectively deposit an electrical contact pattern consisting of a 7 nm thick layer of iridium (Ir) and then a 700 nm layer of gold (Au). In this case, the Ir layer is used to increase adhesion between the contact pattern and the Au layer.

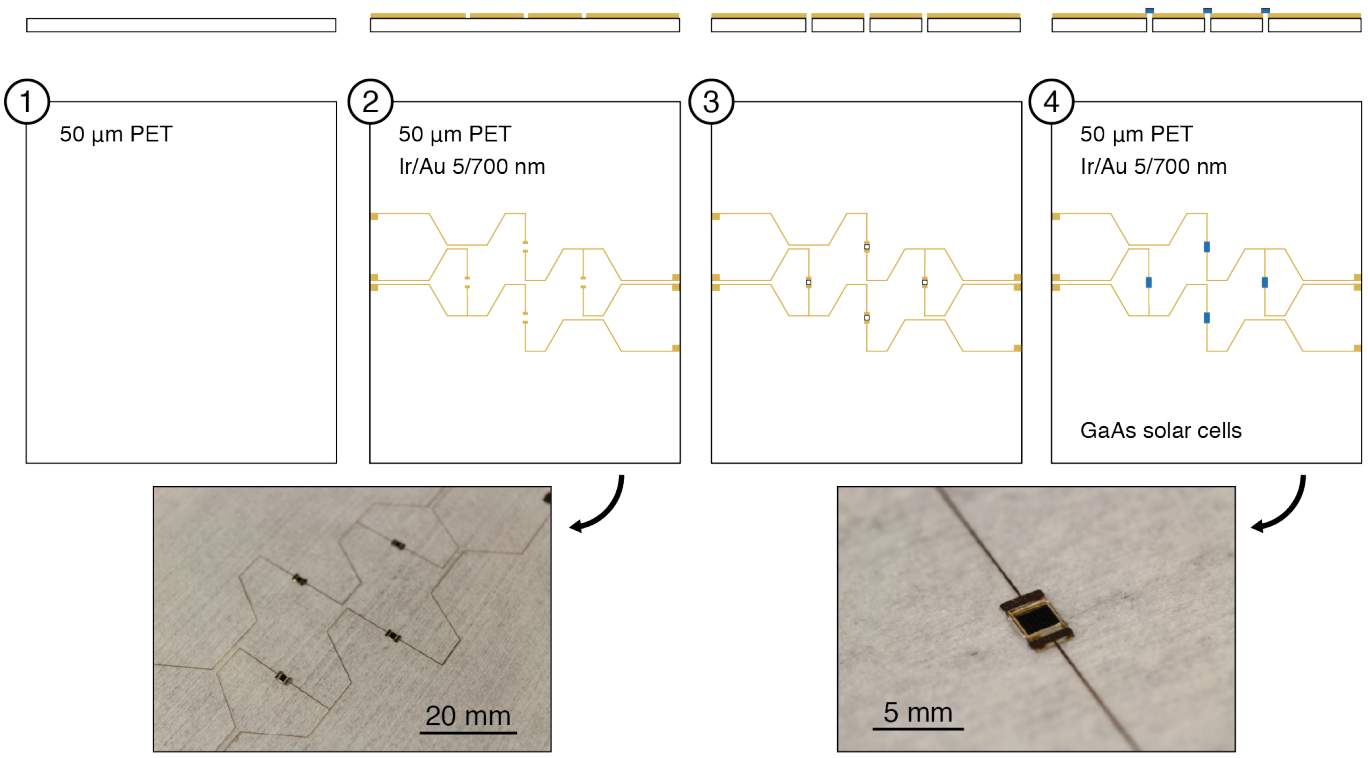

Figure 3.7 Fabrication steps for contact and solar cells integration onto transparent top sheet – (1) cutting of 50 μm PET sheet, (2) selective deposition of contacts using vacuum thermal evaporation, (3) laser cutting of windows to reduce surface reflections, and (4) bonding of gallium arsenide (GaAs) cells to electrical contacts.

(3) To minimize surface reflections at the surface of the solar cell, a through-thickness window is cut into the PET sheet. (4) Finally, the GaAs solar cells are aligned with the window cuts from step (3) and bonded to the Au contacts. This can be accomplished using a variety methods, including but not limited to using either high-conductivity silver (Ag) paste or cold welding techniques as described previously[26-28]. Images of the final top sheet are shown in **Figure 3.7**.

3.3.3 Integration of top and bottom sheets

To significantly simplify the integration of the top and bottom sheets, we used a laser welding process[47] to simultaneously bond the top and bottom sheets and cut the kirigami pattern used for tracking. **Figure 3.8a** provides an overview of this process. (1) First, the top and bottom sheets are aligned and brought into contact with one another – note that the solar cells on the top sheet should be facing down into the parabolic concentrators of the bottom sheet. (2) The combined top and bottom sheets are then aligned to the bed of a CO_2 laser and cut at 100% power, 30% speed, and 1000 pulses per inch (*PPI*) (see **Chapter 2** for more about laser cut parameters). Images of the resulting integrated and bonded trackers are shown in **Figure 3.8b**.

Alignment of laser cutting with the preformed optics is also extremely important to minimize damage to the reflective surface. Specifically, care must be taken to ensure that the laser does not contact the sidewalls of the parabolas, which would in turn provide a pathway for debris generated during the cutting process to enter the optics. This process is detailed further in **Figure 3.9**, where the results on optical clarity for aligned and misaligned cutting are shown.

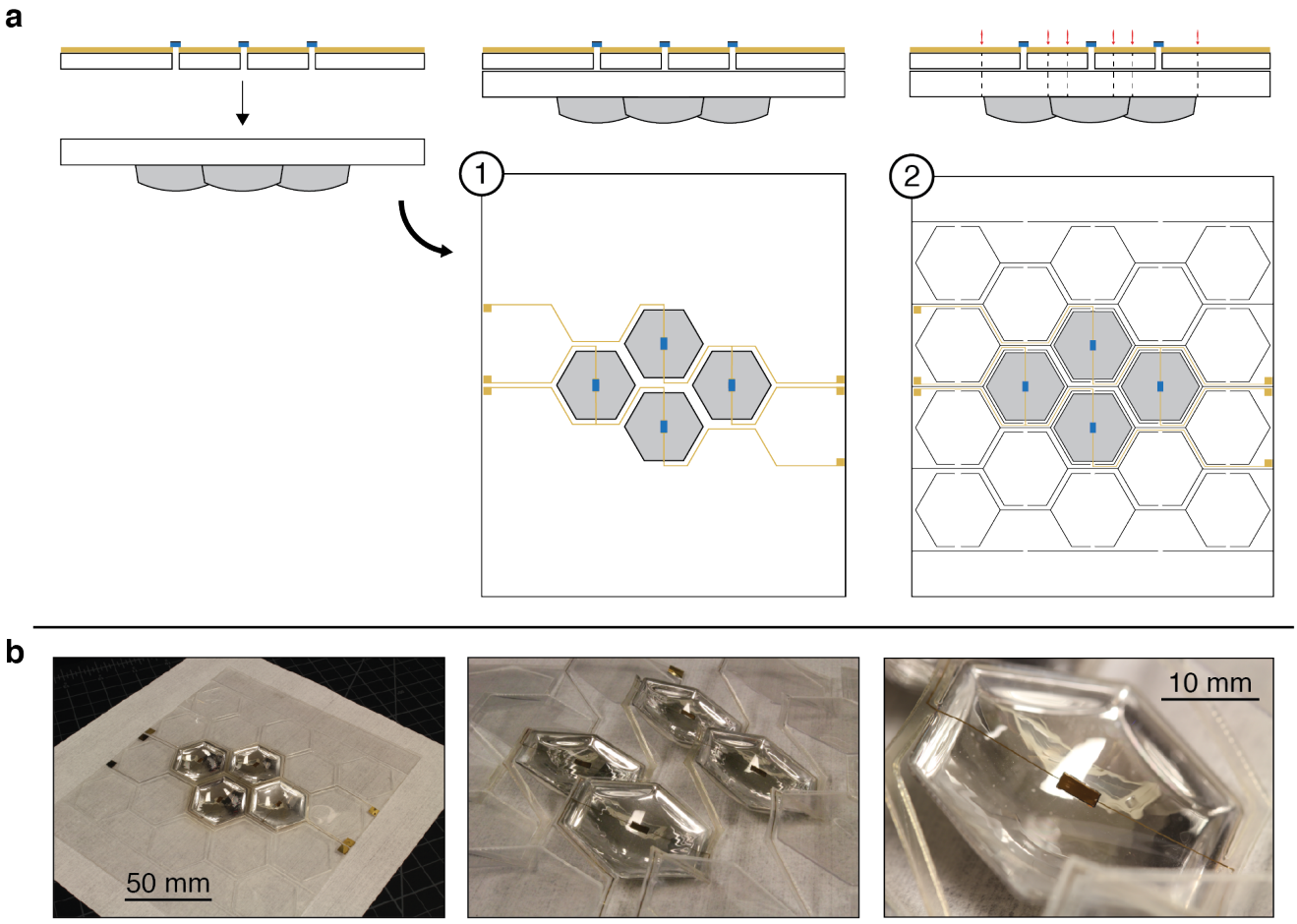

Figure 3.8 (a) Integration of final system requires (1) alignment of top and bottom sheets and (2) simultaneous laser welding and cutting of the kirigami pattern used for tracking. (b) Images of the final assembly following fabrication.

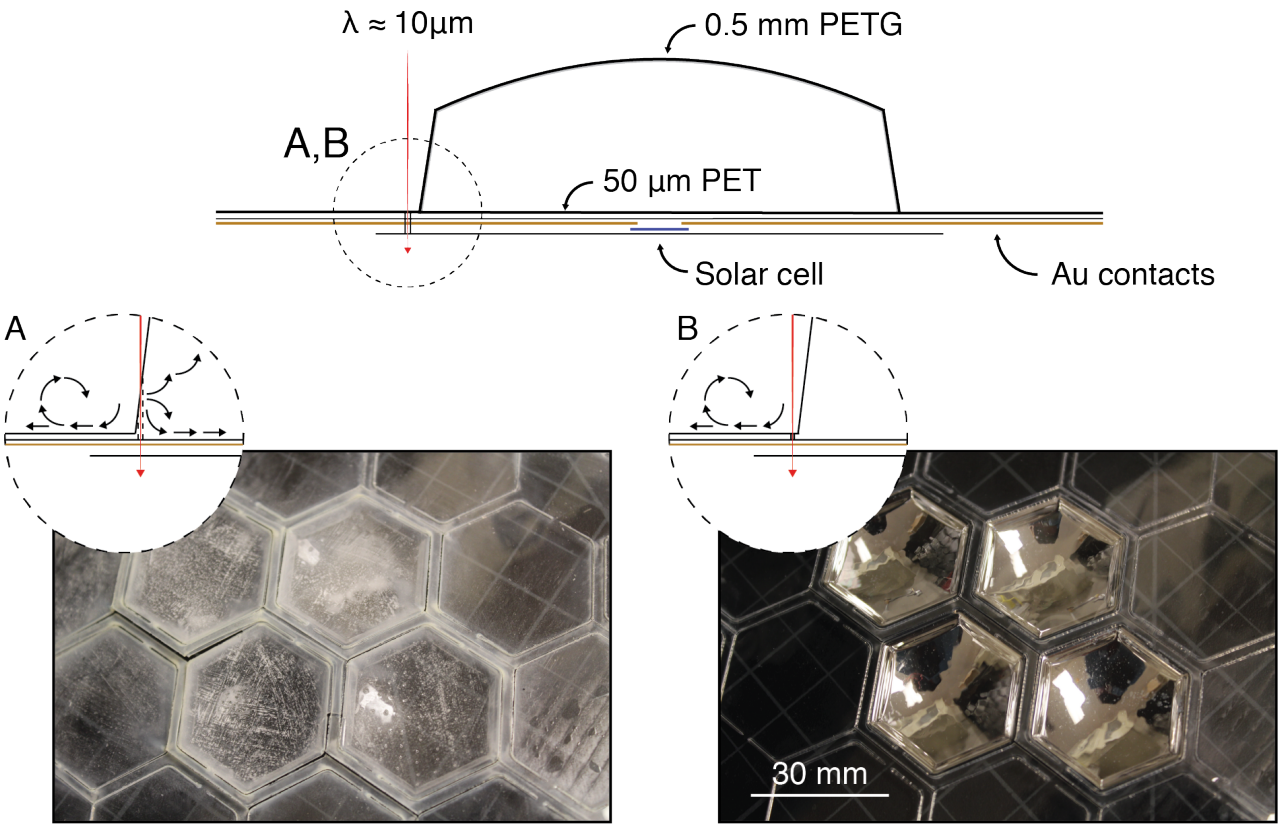

Figure 3.9 Importance of alignment during laser welding and cutting. Notice that (A) poor alignment results in debris that has a negative effect on optical clarity. (B) With proper alignment, the optic cavities remain sealed and are not affected by debris generated during the cutting process.

3.4 Geometric response

The geometric response of the integrated tracker was quantified by straining the sample and measuring the resulting feature angle (θ), similar to the process used in **Section 2.2**. These experimental results are shown in **Figure 3.10a** (red points), along with the theoretical relationship predicted by equation (11) (solid blue line). The deviation in response is due to thin film bending properties, and in particular the interface between the bending elements and the concentrator sections. This effect is shown pictorially in the inset of **Figure 3.10a** and schematically in **Figure 3.10b**, where there is some angle δ between the bending elements and optic due to high stress concentrations and insufficient structural rigidity in that location. Going

forward, these deviations from the predicted relationship may be address by adding reinforcing elements to the interface between bending elements and optics as shown in **Figure 3.10c**.

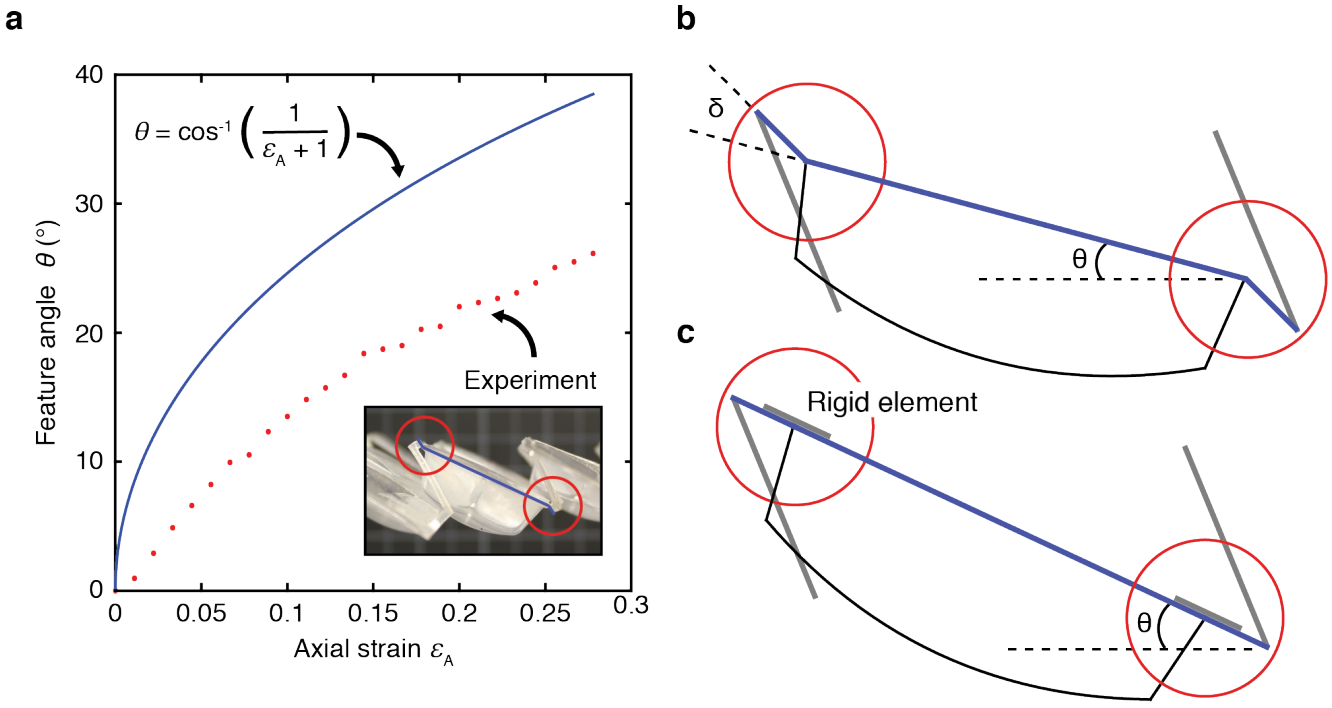

Figure 3.10 (a) Feature angle (θ) versus axial strain (ε_A) for the integrated tracker. Shown are experimental results (red points) and expected results from equation (11) (solid blue line). (b) The deviation from theory (a) results from unwanted bending at the interface between the bending elements and concentrator optics. (c) Going forward, rigid elements may be added to reinforce this interface, reduce bending, and recapture response predicted by equation (11).

3.5 System performance

3.5.1 Optical and power concentrator factors

Using equation (64), it is possible to calculate an optical concentration factor (CF_O):

$$CF_O = \frac{A_{Ap}}{A_{Cell}} \eta_{CF} \tag{64}$$

where, in this case, the area of the aperture (A_{Ap}) also accounts for the area occupied by the electrical contacts and substrate onto which the solar cells are mounted. Ray-tracing simulations were also conducting to confirm the expected concentration factor (courtesy of Byungjun Lee). A breakdown of the areas, optical concentrator factor, and ray-tracking result for the final concentrator design from **Figure 3.5b** is shown in **Table 4**.

Table 3.2 Breakdown of design parameters, concentration factor, and ray-tracing results

A_{Hex} (mm^2)	$A_{Contacts}$ (mm^2)	A_{Ap} (mm^2)	A_{Cell} (mm^2)	CF_O	Ray-Tracing
679	23.4	655.6	3.6	182x	177x

Notice that the expected concentration factor due to ray tracing is slightly below that predicted by the geometric relationship in equation (64). This is most likely due to using an insufficient number of rays during the simulation, and can be addressed by refining the simulation in the future.

When experimentally determining the concentration factor of the system, it is important to consider both the optical concentration factor (CF_O) as well as the power concentration factor (CF_P). Experimentally, we can calculate CF_O by dividing the current density measured at concentration to the current density measured at one sun:

$$CF_O = \frac{J_{SC}\big|_{Concentration}}{J_{SC}\big|_{1\,Sun}} \tag{68}$$

and CF_P by dividing the maximum power point (P_{MPP}) measured at concentration to the maximum power point measured at one sun:

$$CF_P = \frac{P_{MPP}\big|_{Concentration}}{P_{MPP}\big|_{1\ Sun}} \tag{63}$$

where P_{MPP} is the power density at maximum power point:

$$P_{MPP} = V_{MPP} J_{MPP} \tag{69}$$

and V_{MPP} and J_{MPP} are the voltage and current densities at the maximum power point, respectively.

The current density and voltage (*J-V*) characteristics for a GaAs solar cell under one sun and also for the integrated system are shown in **Figure 3.11**. Specifically, **Figure 3.11a** shows the *J-V* curve for a GaAs solar cell under one sun before mounting onto the top sheet. Both the GaAs solar cell under one sun (solid blue line) and integrated system (red dashed line) are shown in **Figure 3.11b** for comparative purposes. Notice the significant increase in J_{SC} and P_{MPP} for the integrated system. Using these measured values, the optical concentrator factor (CF_O) and power concentration factor (CF_P) were ~80x and 58.5x (~60x), respectively.

It should be noticed that CF_O (~80x) is less than the theoretical predictions from equation (63) and ray tracing (182x and 177x, respectively). This decrease is due to a variety of factors, including misalignment during testing, less than unity absorption at the surface of the solar cell (particular at high incident angles from rays near the rim angle), and also less than unity reflection at the surface of the parabola. These areas may be addressed in future design iterations, although care must be taken when balancing the tradeoffs between CF_O and the effects of temperature on cell performance. These effects will be discussed further in the following sections.

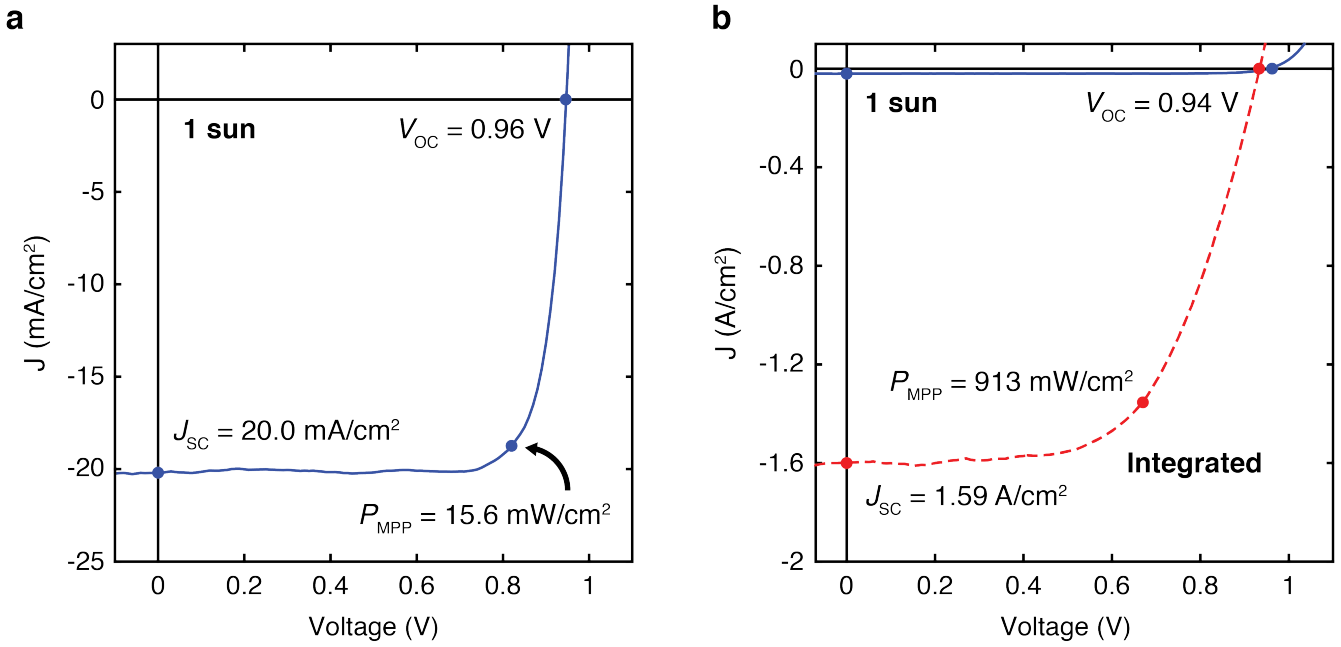

Figure 3.11 (a) Current voltage (*J*) versus voltage (*V*) (*J-V*) curve for GaAs solar cell measured under one sun AM1.5G illumination. Also shown are short circuit current (J_{SC}), open circuit voltage (V_{OC}), and power at maximum power point (P_{MPP}). (b) Comparison *J-V* curves for GaAs cell under one sun (solid blue line) and for integrated tracker with concentration (dashed red line). Using measured, the optical concentration factor (CF_O) and power concentration factor (CF_P) are ~80x and 58.5 (~60x), respectively.

3.5.2 Effect of resistance on concentration factor

Series resistance (R_S) in a conventional solar cell has three causes: (1) movement of current through the active material, (2) contact resistance between the metal contact (collection grid) and the active material, and (3) contact resistance of the top and bottom contacts in connection with electrical probes. For the integrated system, we must also consider contact resistance between the solar cell and the electrical contact pattern (as a function of bonding technique) and also the movement of current through the electrical contacts. R_S can be deduced from a typical *J-V* curve by looking at the slope near V_{OC}.

A low shunt resistance (R_{SH}) will typically cause a decrease in cell performance due to the presence of an additional current pathway. For conventional solar cells, a low R_{SH} is typically due to manufacturing defects. For the integrated system, we must also consider effects of contact

design on R_{SH} – in particular, the interface between top and bottom contacts, and the thickness and quality of the passivation layer used. R_{SH} can be deduced from a typical *J-V* curve by looking at the slope near J_{SC}.

Figure 3.12a provides a schematic view of two prototype designs, each of which has different R_S and R_{SH} (as labeled). In these systems, a high R_S results from insufficient electrical contact width and thickness (here we used 125 μm and 5/500 nm Ti/Au, respectively). On the other hand, a low R_{SH} is due to a low-quality passivation layer and shunting between the top and bottom contacts. For the sample with low R_S and high $R_{SH,}$ the electrical contacts were widened and thickened (here, 325 μm and 5/100/3000/400 nm Ti/Au/Al/Au, respectively), and the polyimide passivation layer quality was improved by using a more controlled annealing procedure to reduce shunting. *J-V* characteristics for the samples with high R_S and low R_{SH} (blue dashed line) and low R_S and high R_{SH} (solid green line) are shown in **Figure 3.12b**, where you can clearly see the effect of R_S and R_{SH} on cell performance. Specifically, J_{SC} increases from 0.89 A/cm^2 to 1.69 A/cm^2 and the resulting P_{MPP} increases from 162 W/cm^2 to 588 W/cm^2 (3.6x greater). Furthermore, in comparison to the baseline cell shown in **Figure 3.11a** (P_{MPP} is 15.6 W/cm^2), the resulting power concentration factor ($CF_{P)}$ increased from ~10x to ~38x.

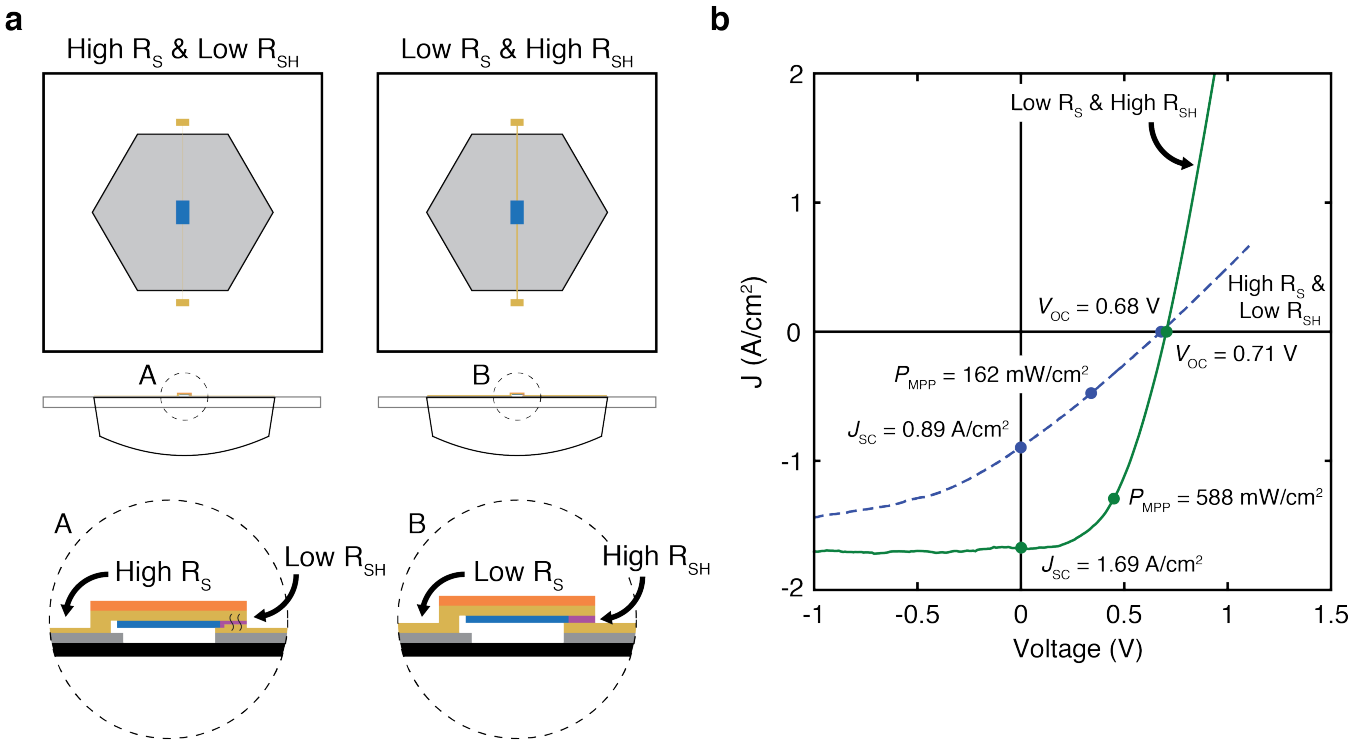

Figure 3.12 (a) Schematics of two prototype systems used to identify the effect of cell design and packaging on system performance. (A) For the non-optimized system, a high series resistance (R_S) results from insufficient electrical contact width and thickness (125 µm and 5/500 nm Ti/Au, respectively), and a low shunt resistance (R_{SH}) is due to a low quality passivation layer and shunting between the top and bottom contacts. (b) R_S is decreased and R_{SH} is increased by widening and thickening the electrical contacts (325 µm and 5/100/3000/400 nm Ti/Au/Al/Au, respectively), and by optimizing passivation layer quality between the top and bottom contacts, respectively.

3.5.3 Effect of temperature on concentration factor

Temperature is important to consider when discussing solar cells, and in particular, when dealing with concentration photovoltaics. As the temperature is increased, the open circuit voltage (V_{OC}) is reduced according to an increase in dark saturation current (I_0) due to an increase in the intrinsic carrier concentration (n_i).

$$V_{OC} = \frac{kT}{q} \ln\left(\frac{I_{SC}}{I_0}\right) \tag{69}$$

$$I_0 = qA\frac{Dn_i^2}{LN_D} \tag{70}$$

$$n_i = BT^3 \exp\left(-\frac{E_{G0}}{kT}\right) \tag{71}$$

where k is the Boltzmann constant ($1.38\text{x}10^{-23}$ J/K), q is the electronic charge ($1.602\text{x}10^{-19}$ C), I_{SC} is the short circuit current, A is the area of the junction, D if the diffusivity, L is the diffusion length, N_D is the doping, B is a constant, and E_{G0} is the bandgap at 0 K[48].

The effect of system cooling on solar cell performance is shown in **Figure 3.13**. Specifically, *J-V* characteristics for the integrated system were measured without (solid green line) and with (red dashed line) cooling in the form of a fan placed in close proximity to the system. Using an infrared thermal imaging camera, the operating temperatures without and with cooling were measured to be ~80 °C and ~40 °C, respectively. With cooling, notice the large increase in V_{OC} from 0.71 V to 0.94 V, and subsequent increase in P_{MPP} from 588 W/cm^2 to 913 W/cm^2. In comparison to the baseline cell shown in **Figure 3.11a** (P_{MPP} is 15.6 W/cm^2), the resulting power concentration factor ($CF_{P)}$ increased from ~38x to ~60x.

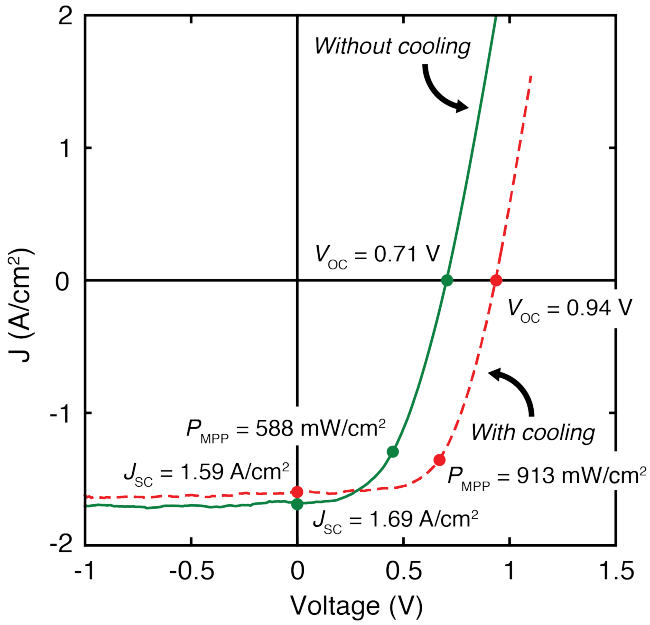

Figure 3.13 Effect of system cooling on open circuit voltage (V_{OC}) and power at maximum power point (P_{MPP}). With the aid of a small fan to provide convective cooling during the measurement, V_{OC} was increased from 0.71 V to 0.94 V and P_{MPP} was increased from 588 mW/cm^2 to 913 mW/cm^2. As compared to the base cell under one sun concentration, this represents an increase in power concentration factor (CF_P) from ~38x to ~60x.

3.6 Conclusions

In summary, we have introduced a new integrated system that combines ~60x solar concentrators and low-profile solar tracking. The new design leverages simple fabrication techniques including vacuum-assisted thermoforming, vacuum thermal evaporation, and laser welding, and is potentially well suited for high-throughput manufacturing. We considered the effects of system design on tracking and optical performance, as well as the effects of series resistance, shunt resistance, and temperature on cell performance.

Going forward, additional work is required to close the gap between the simulated power concentration factor (~180x) and the measured power concentration factor (~60x). For example, alignment methods may be revisited to ensure proper placement of the solar cell at the focal point of the concentration optics and maximize optical concentration factor. Other optical considerations, such as oxidation of the reflective surfaces and surface contamination may also be considered for their impact on optical concentration factor. System thermodynamics should also be studied, and in particular the effects of material selection and cooling on open circuit voltage and power concentration factor. Additional cooling methods may include more active procedures such as using heat transfer or cryogenic fluids, or system redesigns that incorporate thermal fins for increased convective cooling. Other design factors, including the tradeoffs between line dimensions, system size, and material selection, must also be considered for their effect on power concentration factor. The stress-strain response of the system should be studied, as well as the effect of cut geometry and material selection on plastic deformation. An understanding of this response would help to identify new design and materials to increase durability and increase cycle life. Finally, to make tracking more predictable, new mechanical designs should be considered which reduce bending between flexible and rigid elements.

Chapter 4 Additional Applications and Future Work

4.1 Additional kirigami patterns and frameworks

The three-dimension design principles discussed in **Chapter 2** and **Chapter 3** for the linear and modified linear kirigami patterns may also be extended to addition designs. As an example, consider the square kirigami pattern shown in **Figure 4.1a**. The pattern consists of repeating "U-shaped" cuts, where an overlap between the cuts in the axial direction creates a lever arm for mechanical response. Accordingly, pulling on the sheet in the axial direction (**Figure 4.1b**) causes this lever arm to rotate out of the plane of the structure to an angle θ. For the simplest version of this system (i.e. for repeating unit cells), the relevant cut parameters required to calculate θ as a function of ε_A are shown in **Figure 4.1a**. The critical parameter R is the ratio of y_1 over y_2, and is indicative of the overlap between cuts in the axial direction. Note that cut dimensions in the transverse direction (i.e. perpendicular to the direction of ε_A) are not provided, as they do not affect the relationship between ε_A and θ. Using a purely geometric method similar to the one described in **Section 2.2.1.1**:

$$\varepsilon_A = \frac{\sqrt{\left(2y_1 + y_3\right)^2 - \sin^2\left(y_1 - y_2\right)^2} - \left(y_1 - y_2\right)\cos\theta - \left(y_1 + y_2 + y_3\right)}{\left(y_1 + y_2 + y_3\right)} \tag{72}$$

where $y_1 + y_2 + y_3$ is the initial length of the unit cell.

The square kirigami pattern is unique from the linear pattern in that the relationship between θ and ε_A can be controlled as a function of cut geometry (although not the relationship between ε_T and ε_A). To this point, consider the three square patterns shown in **Figure 4.1c**, where R = 3, 4, and 6. The geometric response for these geometries predicted by equation (72) is shown in **Figure 4.1d**. Also shown are the geometric responses for the linear cut pattern (black dashed line) and the original equation for θ as a function of ε_A. Notice that the square pattern is capable of much larger θ than the linear pattern, and also that θ (for a given ε_A) decreases as the measure of overlap (R) increases. This unique geometric response may be extended to designs with changing row dimensions, and potentially used to develop complex focusing optics such as tunable length Fresnel lenses.

4.2 Origami solar tracking

The following work was part of a collaboration in which we demonstrated a lightweight and low profile, and potentially low-cost planar solar-tracking concentrator based on origami bending principles[49]. The system consisted of a folded hexagonal concentrator mounted on top of a sinusoidal bent plastic film (**Figure 4.2a**, adapted from publication), where the orientation of the concentrator and solar cell was controlled as a function of displacement on the edges of the bent film (**Figure 4.2b**). The tracker exhibited excellent mechanical response, with only ~2.8% decrease in strain energy over 10,000 actuation cycles (**Figure 4.2c**), and negligible change in orientation response over the same number of cycles (**Figure 4.2d**). An image of the tracker used for testing is also shown in **Figure 4.2d**. Please see **Chapter 2** for an overview of methods used to measure orientation angle and mechanical response.

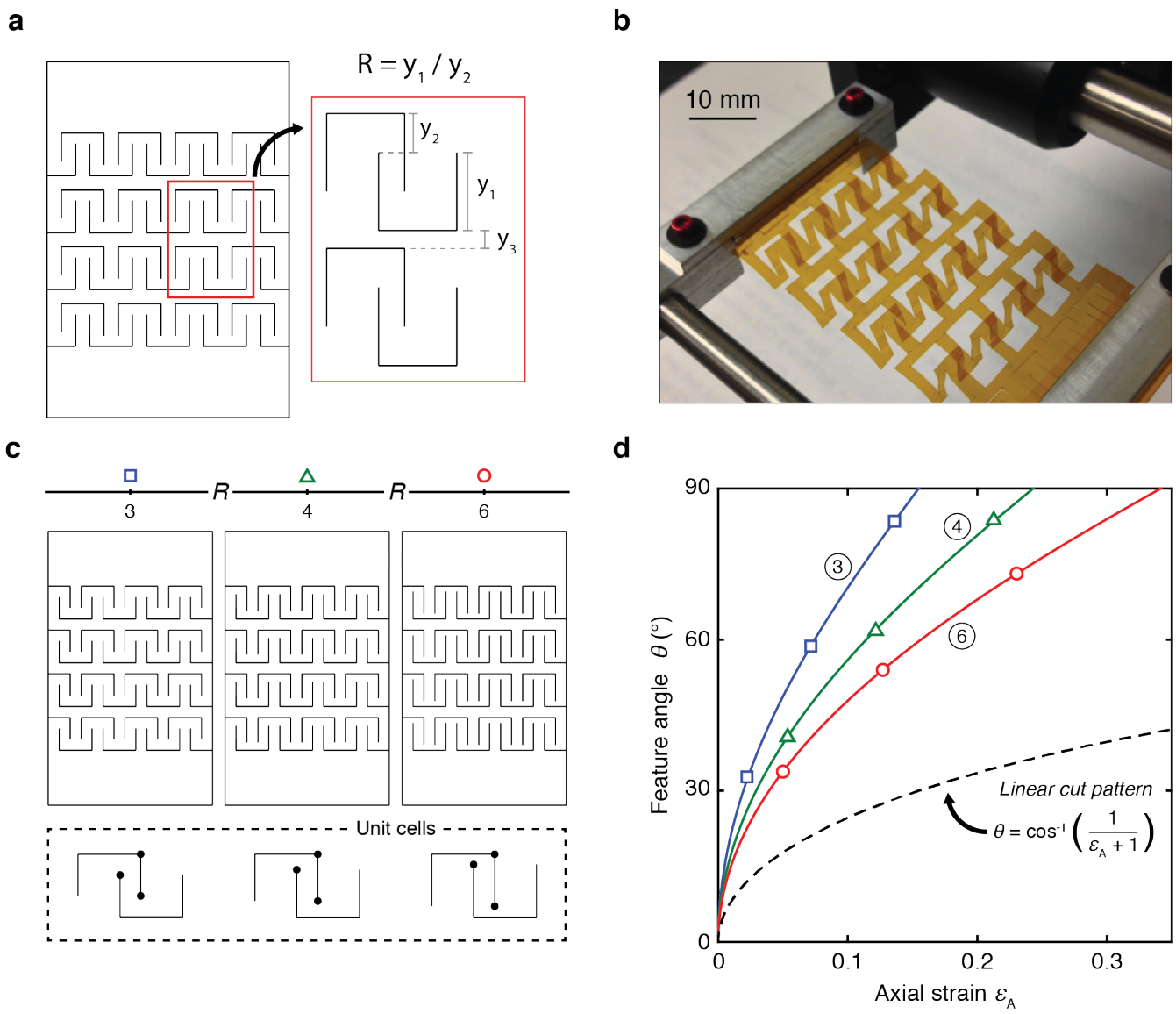

Figure 4.1 (a) Square kirigami pattern and important cut parameters needed to determine geometric response. (b) As the sample is stretched in the axial direction (ε_A), lever arms formed as a result of overlapping cuts rotate out of the plane of the original sheet to an angle θ. (c) Schematics of three kirigami structures, where R = 3, 4, and 6 and is a measure of the amount of overlap between cuts in the axial direction. Also shown are the corresponding unit cells. (d) Feature angle (θ) versus axial strain (ε_A) for the three square kirigami structures shown in (c). For comparison, the linear pattern geometric response is also shown (black dashed line).

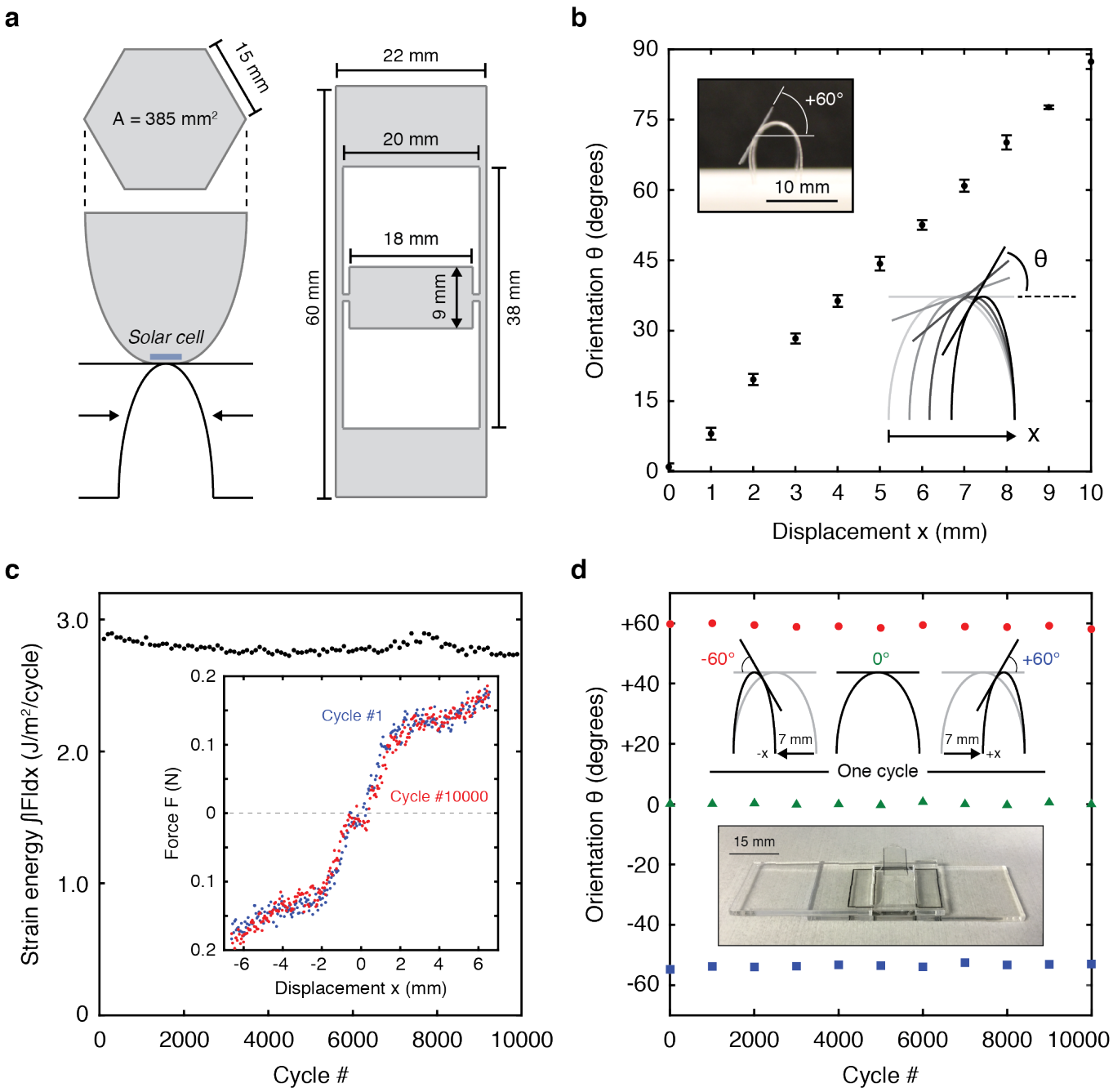

Figure 4.2 (a) Square kirigami pattern and important cut parameters needed to determine geometric response. (b) As the sample is stretched in the axial direction (ε_A), lever arms formed as a result of overlapping cuts rotate out of the plane of the original sheet to an angle θ. (c) Schematics of three kirigami structures, where R = 3, 4, and 6 and is a measure of the amount of overlap between cuts in the axial direction. Also shown are the corresponding unit cells. (d) Feature angle (θ) versus axial strain (ε_A) for the three square kirigami structures shown in (c). For comparison, the linear pattern geometric response is also shown (black dashed line).

4.3 Dynamic control surfaces for drag steering

The following work is being conducted in collaboration with the Inman Group (University of Michigan). Lift and drag vectors (*L* and *D*, respectively), as well as the angle of attack (α) are shown in **Figure 4.3a** Although drag is primarily an adverse aerodynamic effect that causes resistance to moving objects through a fluid, it may also be used asymmetrically in aircraft as the foundation for yaw steering about the nadir (*z*) axis as shown in **Figure 4.3b**. Conventional approaches to drag steering involve actuation of a rudder, which protrudes into the flow and increases drag by changing the direction of the aerodynamic force vector such that a component lies in the direction of free stream flow. Unfortunately, this method requires complex actuation methods and may have a negative impact on radar footprint. Another method of drag steering is via surface texturing, something that has already been achieved using a poro-vascular laminate[50]. Our goal is to use kirigami design principles to develop new systems for drag steering with reduced component costs and a simplified installation process to enable retrofitting.

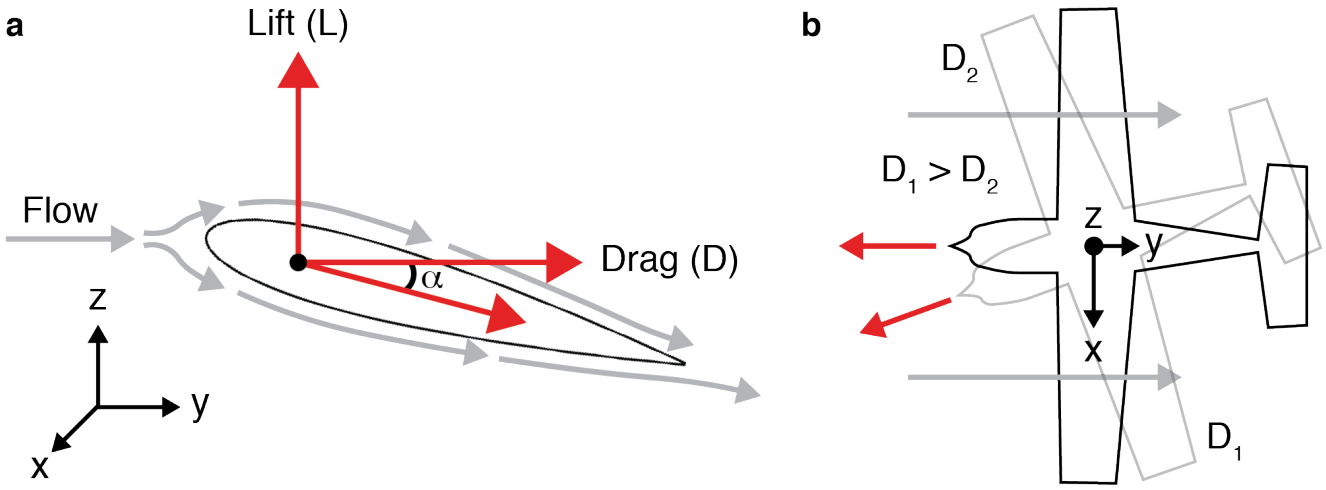

Figure 4.3 (a) Schematic of airfoil in flow at an angle of attack (α), showing force vectors of lift (*L*) and drag (*D*). (b) Drag steering occurs about the *z-axis* (nadir) due to a difference in drag across the width of the aircraft.

Here we discuss the use of the linear kirigami pattern mounted onto the surface of an airfoil to control drag as a function of strain on the system. This is shown schematically in **Figure 4.4a**, whereby straining the sheet along the *y*-axis produces a deformation of the material between cuts out of the plan of the airfoil surface (in the *z*-direction). An image of this deformation is also shown. The linear kirigami pattern was mounted onto a symmetric airfoil (NACA 0012) and placed into a wind tunnel with flow at 10 m/s. Subsequently, lift and drag measurements were taken at varying angles of attack (α) for each ε_A. Lift and drag values were then normalized to lift coefficients (C_L and C_D, respectively), dimensionless values that relate lift and drag to the fluid density around the body, the fluid velocity, and an associated reference area for the airfoil. As shown in **Figure 4.4b** (and in the inset for C_L at $\alpha = 0°$), there was negligible effect of kirigami ε_A on lift. On the other hand, C_D appears to increase with ε_A as shown in **Figure 4.4c** (and in the inset for C_D at $\alpha = 0°$). These results are extremely promising, as they provide preliminary proof that kirigami skins may be used to control drag properties and potentially enable drag steering. Going forward, additional work is required to verify results, test new kirigami geometries, and also determine the effect of system scale and flow speed on performance.

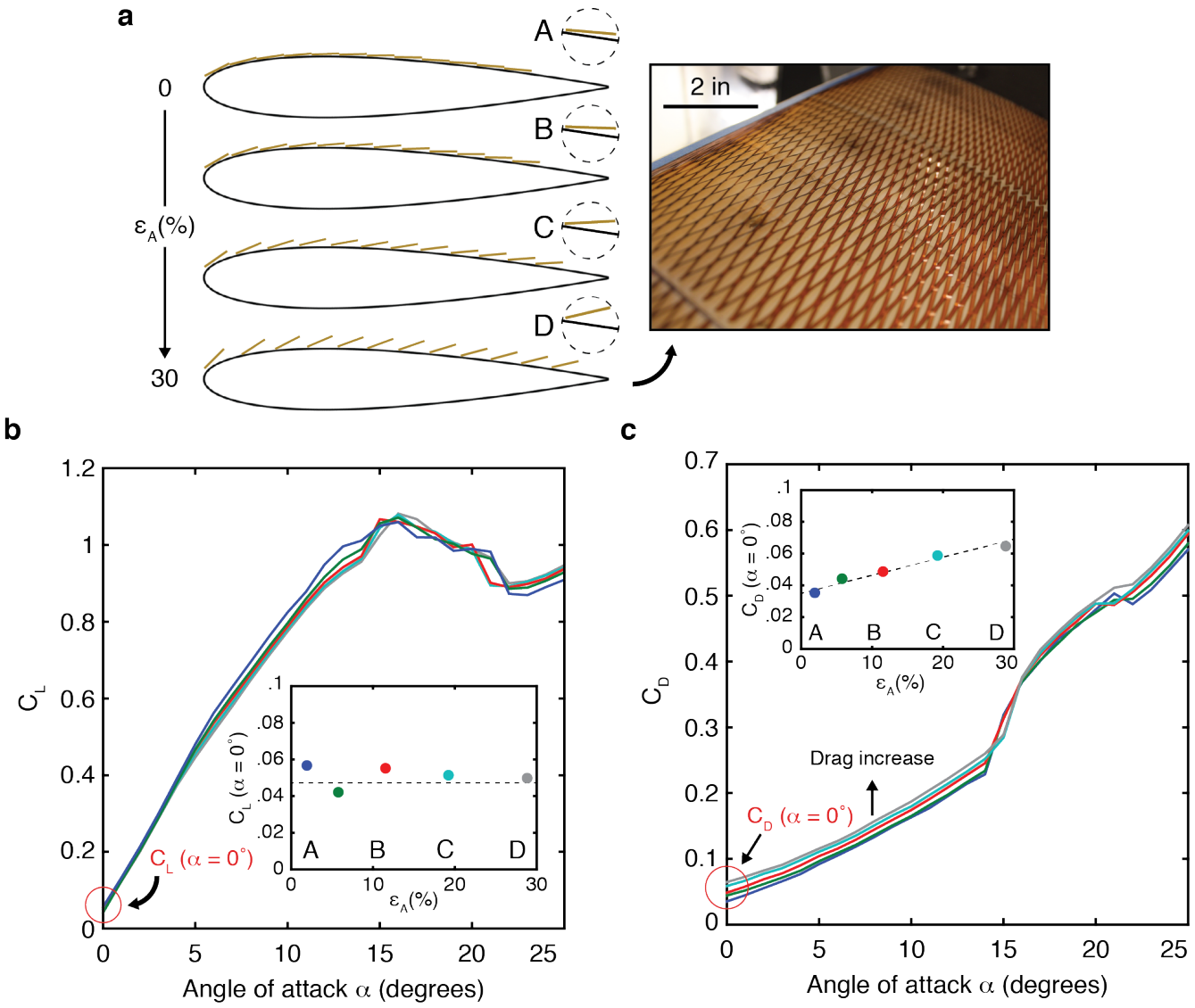

Figure 4.4 (a) Schematics of the linear kirigami pattern mounted on a symmetric airfoil (NACA 0012) at varying strains (ε_A). Also shown is an image of a Kapton® kirigami pattern on a symmetric airfoil at ε_A = 30%. (b) Coefficients of lift (C_L) versus angle of attack (α) for kirigami structures at increasing ε_A. *Inset*: C_L at α = 0° versus ε_A. (c) Coefficients of drag (C_D) versus angle of attack (α) for kirigami structures at increasing ε_A. *Inset*: C_D at α = 0° versus ε_A. Importantly, C_D is shown to increase as ε_A showing promise for drag steering.

4.4 Origami tessellations for electrochemical energy storage

The following work is being conducted in collaboration with the Mayer group (Adolphe Institute, University of Fribourg) to develop an electric eel-inspired origami-enabled battery. In the electric eel, complex neural network controls the open of sodium ion (Na^+) channels on the innervated side of each electrocyte, leading to transcellular potentials that add in series across the width of the organ[51]. In the proposed system, anion and cation-selective hydrogels (*ASH* and *CSH*, respectively) along with salt water and water hydrogels (*SWH* and *WH*, respectively) are patterned on a semipermeable, hydrophobic membrane **(Figure 4.5a**). This membrane is then folded using a *Miura-ori* pattern, which ensures registration between hydrogels and provides the conductive pathway for ion flow (**Figure 4.5b**). An example of the patterned hydrophobic substrate is shown in **Figure 4.5c**. This system has the potential to generated over 100V, and has added benefits of a small form factor and potentially on-off functionality for greater shelf life.

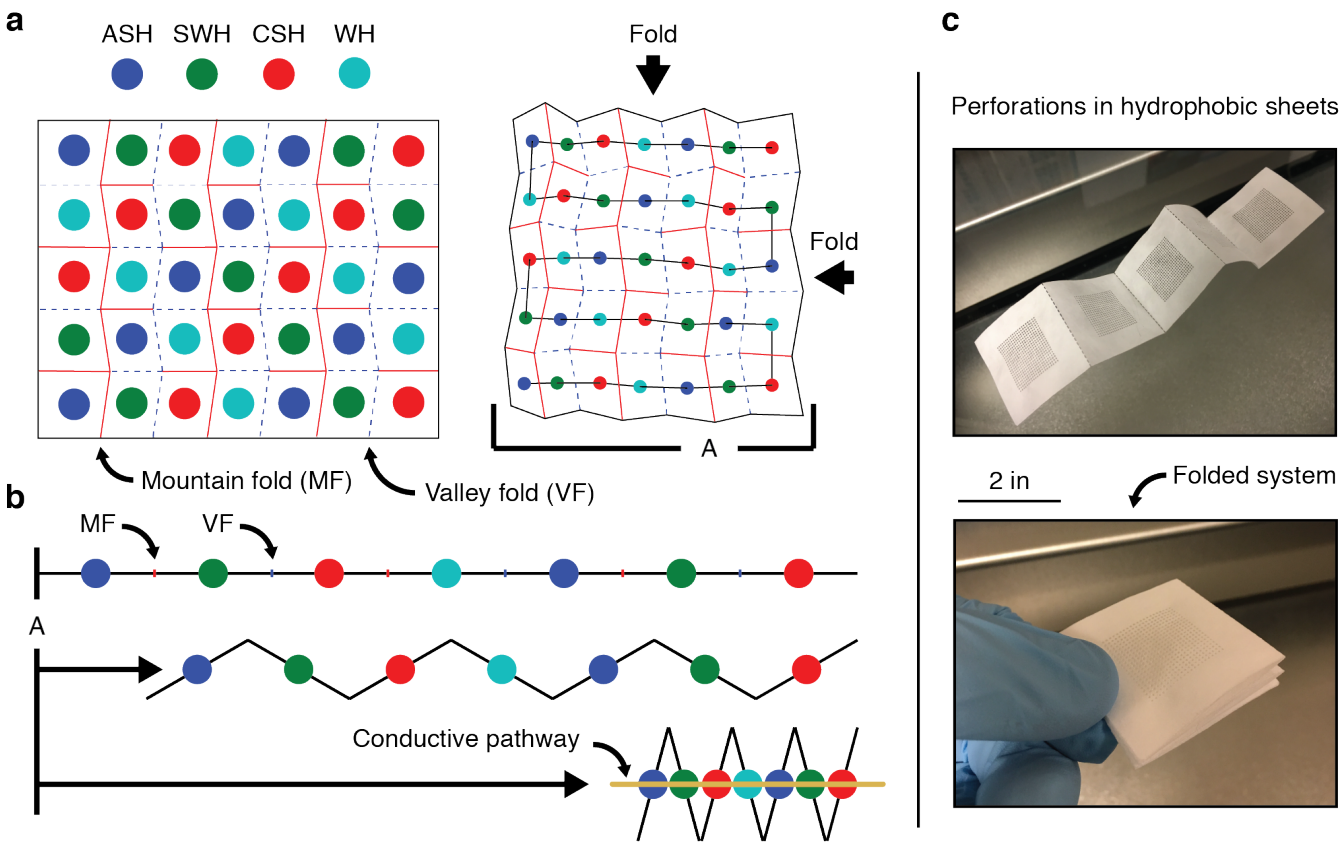

Figure 4.5 (a) Anion and cation-selective hydrogels (*ASH* nd *CSH*, respectively) and salt water and water hydrogels (*WH* and *SWH*, respectively), patterned on a semipermeable, hydrophobic membrane. (b) A *Miura-ori* fold is used to bring each hydrogel into contact and ensure registration across the sheet. (c) Images of perforated hydrophobic sheets before hydrogen patterning.

4.5 Kirigami designs for tunable antennas

The following work is being conducted in collaboration with the Grbic Group (University of Michigan). The rapid expansion of and miniaturization of mobile electronics has created the need for more advanced antennas[52]. Here we will outline initial work towards a tunable antenna where gain and input impedance may potentially be controlled as a function of out-of-plane deformation achieved via kirigami engineering. A schematic of the kirigami design is shown in **Figure 4.6a**, where the linear cut pattern is symmetric about a center axis (*z*-direction). The

electrical pathway for the antenna is formed using a patterned conductive film – gold (Au) is shown in this example. This structure may be mounted to a coaxial cable to provide signal and ground as shown in **Figure 4.6b**. This deformation of this kirigami structure may be controlled as a function of out of plane deformation as shown in finite element models in **Figure 4.6c**. Interestingly enough, we believe this deformation, and in particular the resulting shape of the conductive pathway, will allow tunability of the antenna output. Additional work is currently underway using the experimental setup shown in **Figure 4.6b**.

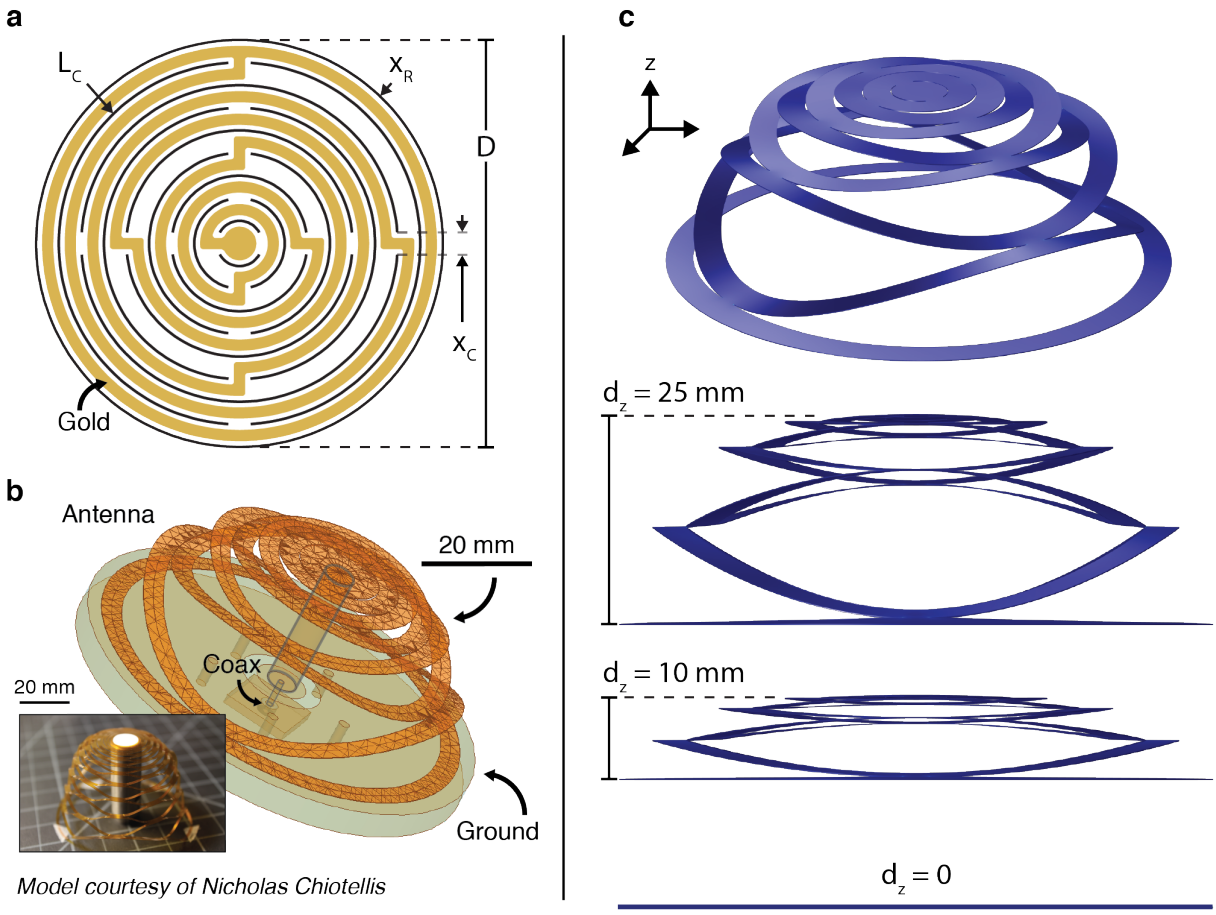

Figure 4.6 (a) Schematic of antenna design, consisting of axially-symmetric linear pattern and electrical contacts. (b) Experimental setup to measure antenna response. Also shown is a prototype antenna made from Kapton® film. (c) COMSOL modeling of kirigami response, shown as a function of *z-axis* deflection (0 to 25 mm).

4.6 Conclusions and future work

In this thesis, we have demonstrated a novel approach to three-dimensional design using origami and kirigami principles with a focus on developing optoelectronic systems to decrease the cost of solar electricity. In **Chapter 2**, we demonstrated a novel method of integrated, low-profile solar tracking whereby a simple kirigami pattern in thin-film gallium-arsenide solar cells enables tracking at the substrate level simply by stretching the sheet. The new tracker is inherently lightweight and less susceptible to wind loading, which greatly reduces tracking system complexity, size, and cost, while also enabling new applications. System performance is considered as a function of cut geometry, materials selection, and geographic location, and optimized performance is shown to generate up to ~40% more energy per solar cell area over the course of a day relative to a stationary, flat panel module. Electrical and mechanical robustness are also considered with implications towards long-term solar tracking applications (i.e. >10,000 actuation cycles).

In **Chapter 3**, similar design principles were extended to develop a new integrated system that combines ~60x solar concentrators and low-profile solar tracking. The new design leverages simple fabrication techniques including vacuum-assisted thermoforming, vacuum thermal evaporation, and laser welding, and is potentially well suited for high-throughput manufacturing. We considered the effects of system design on tracking and optical performance, as well as the effects of series resistance, shunt resistance, and temperature on cell performance. Although initial results look promising, additional work is required to fully maximize optical and power concentration factors and also to increase system robustness.

Finally, we discussed several new frameworks and applications, all of which were built on the fundamental principles discovered in **Chapters 2 and 3**. Examples included textured surfaces for

flow manipulation and drag steering, kirigami patterns for tunable antennas, and origami tessellations for novel forms of electrochemical energy storage. Although not discussed in this thesis, we also believe novel forms of actuation (e.g. piezoelectric materials, shape-memory alloys, etc.) should be considered in combination with these constructs. We hope the work presented in this thesis will serve as a foundation for future design iterations, and enable new systems for existing and future applications going forward.

BIBLIOGRAPHY

1 Lang, R.J "Origami Design Secrets." Dover Publications (2003).

2 Miura, K. Proposition of Pseudo-Cylindrical Concave Polyhedral Shells. *Institute of Space and Aeronautical Science*, University of Tokyo, Report No. 442 (1969).

3 Miura, K.. "PCCP Shell." *New Approaches to Structural Mechanics, Shells, and Biological Structures*. Springer Science (2002).

4 Wu, W. *et al*. A solution for folding rigid tall shopping bags. *Proceedings of the Royal Society A: Mathematical, Physical and Engineering Sciences*. 467:2561-2574 (2011).

5 Zirbel, S. *et al*. Accommodating thickness in origami-based deployable arrays. *Journal of Mechanical Design.* 135, 111005 (2013).

6 Mroz, K. & Pipkorn, B. *6th European LS-DYNA User's Conference* (Gothenburg, Sweden, 2007).

7 Cho, J.H. *et al*. Nanoscale origami for 3D optics. *Small* 7, 1943-1948 (2011).

8 Kuribayashi, K. *et al*. Self-folding devices and materials for biomedical applications. *Trends in Biotechnology*. 30, 138-146 (2012).

9 Tang, R. *et al*. Origami-enabled deformable silicon solar cells. *Applied Physics Letters*. 104, 083501 (2014).

10 Song, Z. *et al*. Origami lithium-ion batteries. *Nature Communications*. 5:3140 (2014).

11 Oru Kayak: Folding Kayaks That Go Anywhere. www.orukayaks.com (2016).

12 Cruz, P. *et al*. *ICSA2010 1st International Conference on Structures & Architecture* (CRC Press/Balkema Taylor & Francis Group, 2010).

13 Xu, L. *et al*. Kirigami nanocomposites as wide-angle diffraction gratings. *ACS Nano* 10, 6156-6162 (2016).

14 Shyu, T.C. *et al*. A kirigami approach to engineering elasticity in nanocomposites through patterned defects. *Nature Materials* 14, 785-789 (2015).

15 Key World Energy Statistics. *International Energy Agency (*2016).

16 United States Energy Statistics. *International Energy Agency* (2014).

17 Gangon, P. *et al*. Rooftop Solar Photovoltaic Technical Potential in the United States: A Detailed Assessment. *National Renewable Energy Laboratory* (2016).

18 Table 1.1. Net Generation by Energy Source: Total (All Sectors), 2006-September 2016. *U.S. Energy Information Administration*. (2016).

19 Levelized Cost and Levelized Avoided Cost of New Generation Resources in the Annual Energy Outlook 2016. *U.S. Energy Information Administration* (2016).

20 Barbose, G. Tracking the Sun VI: An Historical Summary of the Installed Price of Photovoltaics in the United States from 1998 to 2012. *Lawrence Berkeley National Laboratory* (2014).

21 Best Research-Cell Efficiencies. *National Renewable Energy Laboratory* (2015).

22 Shockley, W. & Quisser, H.J. Detailed Balance Limit of Efficiency of p-n Junction Solar Cells. *Journal of Applied Physics* 32, 510-519 (1961).

23 Beard, M.C. *et al*. The promise and challenge of nanostructured solar cells. *Nature Nanotechnology* 9, 951-951 (2014).

24 Photovoltaics Report. *Fraunhofer Institute for Solar Energy Systems, ISE* (2016).

25 Goodrich, A. *et al*. Residential, Commercial, and Utility-Scale Photovoltaic (PV) System Prices in the United States: Current Drivers and Cost-Reduction Opportunities. *National Renewable Energy Laboratory* (2013).

26 Konagai, M. *et al*. High efficiency GaAs thin film solar cells by peeled film technology. *Journal of Crystal Growth* 45, 277-280 (1978).

27 Lee, K. *et al*. Multiple growths of epitaxial lift-off solar cells from a single InP substrate. *Applied Physics Letters* 97, 101107 (2010).

28 Lee, K. *et al*. Non-destructive wafer recycling for low-cost thin-film flexile optoelectronics. *Advanced Functional Materials* 24, 4284 (2014).

29 Mousazadeh, H. *et al*. A review of principle and sun-tracking methods for maximizing solar systems output. *Renewable and Sustainable Energy Reviews* 13, 1800-1818 (2009).

30 Lee, C. *et al*. Sun tracking system: a review. *Sensors* 9, 3875-3890 (2009).

31 Goussev, O.A. Void-containing materials with tailored Poisson's ratio. *Journal of Applied Physics* 88, 4013 (2000).

32 Lamoureux, A. *et al*. Dynamic kirigami structures for integrated solar tracking. *Nature Communications* 6:8092 (2016).

33 Philipps, S.P., *et al*. Current Status of Concentrator Photovoltaic (CPV) Technology. *Fraunhofer Institute for Solar Energy Systems, ISE* (2016).

34 Algora, C. *et al*. A GaAs Solar Cell with an Efficiency of 26.2% at 1000 Suns and 25.0% at 2000 Suns. *IEEE Trans. Electron Devices* 48, 840-844 (2001).

35 Ryu, K. *et al*. Concept and Design of Modular Fresnel Lenses for Concentration Solar PV System. *Sol. Energy* 80, 1580-1587 (2006).

36 Yamaguchi, M. *et al*. Multi-Junction II-V Solar Cells: Current Status and Future Potential. *Sol Energy* 79, 78-85 (2005).

37 Rosell, J.I. *et al*. Design and Simulation of a Low Concentration Photovoltaic/thermal System. *Energy Convers. Manage* 46, 3034-3036 (2005).

38 Coventry, J.S. Performance of a Concentrating Photovoltaic/thermal Solar Collector. *Sol. Energy* 78, 211-222 (2005).

39 Lee, K. *et al*. Transforming the Cost of Solar-to-Electrical Energy Conversation: Integrating Thin-Film GaAs Solar Cells with Non-Tracking Mini-Concentrators. *Light: Sci. Appl.* 4 (2015).

40 Feuermann, D. & Gordon, J.M. High-Concentration Photovoltaic Designs Based on Miniature Parabolic Dishes. *Sol. Energy* 70, 423-430 (2001).

41 Lovegrove, K. *et al*. A new 500m2 Paraboloidal Dish Solar Concentrator. *Sol. Energy* 85, 620-626 (2011).

42 Tan, M.H. *et al*. Optical Characterization of Nonimaging Dish Concentrator for the Application of Dense-Array Concentrator Photovoltaic System. *Appl. Opt.* 53, 475-486 (2014).

43 Yoon, J. *et al*. Flexible concentrator photovoltaics based on microscale silicon solar cells embedded in luminescent waveguides. *Nature Communications* 2, 1-8 (2011).

44 Sheng, X. *et al*. Doubling the power output of bifacial thin-film GaAs solar cells by embedding them in luminescent waveguides. *Adv. Energy Mater*. 3, 991-996 (2013).

45 Duerr, F. *et al*. Tailored free-form optics with movement to integrate tacking in concentration photovoltaics. *Opt. Express* 21, A401-A411 (2013).

46 Price, J.S. *et al*. Wide-angle planar microtracking for quasi-static microcell concentrating photovoltaics. *Nature Communications* 6, 1-8 (2015).

47 Coelho, J.P. *et al*. High-speed laser welding of plastic films. *Optics and Laser in Engineering* 34, 385-395 (2000).

48 Sinton, R.A. & Cuevas, A. Contactless determination of current-voltage characteristics and minority-carrier lifetimes in semiconductors from quasi-steady-state photoconductance data. *Applied Physics Letters* 69, 2510-2512 (1996).

49 Lee, K. *et al*. Origami Solar-Tracking Concentrator Array for Planar Photovoltaics. *ACS Photonics* 3, 2134-2140 (2016).

50 Thomas, J. *et al*. Two-phase poro-vascular laminates with structure-plus-surface roughness control. The 19th International Conference on Composite Materials (Montreal, Canada 2013).

51 M. Piccolino. The bicentennial of the voltaic battery (1800-2000): the artificial electric organ. *Trends in Neurosciences* 23, 147-151 (2000).

52 Pfeiffer, C. *et al*. Direct transfer patterning of electrically small antennas onto three-dimensionally contoured substrates. *Advanced Materials* 24, 1166-1170 (2012).